



Michigan Technological University
Create the Future Digital Commons @ Michigan Tech

Dissertations, Master's Theses and Master's
Reports - Open

Dissertations, Master's Theses and Master's
Reports

2012

Implementation of porous silicon technology for a fluidic flow-through optical sensor for pH measurements

Kumar L. Vanga
Michigan Technological University

Follow this and additional works at: <https://digitalcommons.mtu.edu/etds>



Part of the [Electrical and Computer Engineering Commons](#)

Copyright 2012 Kumar L. Vanga

Recommended Citation

Vanga, Kumar L., "Implementation of porous silicon technology for a fluidic flow-through optical sensor for pH measurements", Dissertation, Michigan Technological University, 2012.
<https://doi.org/10.37099/mtu.dc.etds/71>

Follow this and additional works at: <https://digitalcommons.mtu.edu/etds>



Part of the [Electrical and Computer Engineering Commons](#)

Implementation of Porous Silicon Technology for a Fluidic Flow-Through Optical Sensor
for pH Measurements

By

Kumar L. Vanga

A DISSERTATION

Submitted in partial fulfillment of the requirements for the degree of

DOCTOR OF PHILOSOPHY

(Electrical Engineering)

MICHIGAN TECHNOLOGICAL UNIVERSITY

2012

© 2012 Kumar L. Vanga

This dissertation, "Implementation of Porous Silicon Technology for a Fluidic Flow-Through Optical Sensor for pH Measurements," is hereby approved in partial fulfillment of the requirements for the Degree of DOCTOR OF PHILOSOPHY IN ELECTRICAL ENGINEERING.

Department of Electrical and Computer Engineering

Signatures:

Dissertation Advisor _____
Dr. Paul L. Bergstrom

Department Chair _____
Dr. Daniel R. Fuhrmann

Date _____

Contents

List of Figures	vii
List of Tables	xii
Acknowledgments	xiii
Abstract	xvi
1 Motivation And Goals	1
1.1 Introduction	1
1.2 Flow-Through Sensing Technologies	4
1.2.1 Background	4
1.2.2 Detection of Lead: Flow Injection System	6
1.2.3 Fluorescent Dye Detection Technique With VCSEL	7
1.3 Fluorescence Spectroscopy	9
1.4 Dye Immobilization- Porous Silicon Template	11
1.4.1 Immobilization of Dye on Capillary Based Sensors	11
1.5 pH Sensor Based on pH Sensitive Fluorescent Dye	13
1.6 Flow-Through Sensing System Requirements	15

1.7	Motivation	17
1.8	Research Statement	23
1.9	Proposed Flow-Through Sensing Device (FTSD)	25
1.10	Goals	26
1.11	Organization of the Dissertation	28
2	Implementation of Porous Silicon Membranes For Electro-Osmotic Pumps .	31
2.1	Introduction	31
2.1.1	Electro-Osmotic Pump Theory	32
2.2	Experimental Methods	38
2.3	Results	40
2.3.1	Mesoporous Silicon Pore Characterization	40
2.3.2	Mesoporous Silica Formation	42
2.4	EOP Test	42
2.4.1	Flow Rate And Pressure Measurements	46
2.4.2	Pressure vs. Pore Size	55
2.4.3	Power Considerations For the EOP	56
2.5	Fluid Permeability Test	57
2.5.1	Stress in the Mesoporous Silica Membrane	59
2.6	Summary	60
3	Optical Properties of Mesoporous Silicon/Silica	62
3.1	Introduction	62

3.2	Experimental Methods	65
3.3	Optical Measurements of Mesoporous Silica	67
3.3.1	Transmission Spectra	68
3.3.2	Angle Resolved Transmission Spectra	70
3.3.3	Angle Resolved Reflection Spectra	72
3.3.4	Optical Constants	74
3.4	Summary	80
4	Flow-Through Sensing Using Fluorescence Measurements	81
4.1	Introduction	81
4.2	pH Measuring Mechanism	82
4.3	Flow-Through Sensing Device	85
4.3.1	Monolayer Preparation- Immobilization of Dye	88
4.3.2	Optical Constants of the Fluorescent Dye- Fluorescein	90
4.3.3	Fluorescence Studies	92
4.3.4	Sensitivity of the pH Sensor	96
4.4	Real Time Implementation of FTSD in Lakes	98
4.5	Summary	99
5	Conclusions And Future Work	100
5.1	Future Work	103
5.1.1	300 nm pore size for EOP	103
5.1.2	Flow-Through Measurement - FTSD	106

5.1.3	Silicon Nanorod Fabrication And Applications	110
References		113
A Porous Silicon Fabrication		126
A.1	Introduction	126
A.1.1	Electrochemical Anodization Setup	127
A.1.2	Macroporous Silicon - <i>p</i> (100) Substrates	129
A.1.3	Photoresist Spinning	132
A.1.4	RF-Sputtering: Mask Deposition	133
A.1.5	Photolithography	135
A.1.6	Reactive Ion Etching	139
A.1.7	Inverted Pyramidal Pits: Nucleation Sites	141
A.2	Introduction to Porous Silicon	143
A.2.1	Porous silicon: Applied Current Density	144
A.2.2	Thermal Oxidation	146
A.2.3	Rapid Thermal Annealing	147
A.2.4	Through-Wafer Pores- Micro-polishing	148
A.2.5	Lift-Off: Cr-Au Mask	150
A.3	Pore Size Control: Spherical Polystyrene Beads	156
A.4	Summary	158
B Permission For Figures		160

List of Figures

1.1	Various micropumps with flow rates and pressure capacities.	3
1.2	Flow injection analytical system utilized for the detection lead.	7
1.3	Fluorescent dye detection technique with VCSEL configuration.	8
1.4	Fluorescence intensity spectra with excitation and emission peak.	10
1.5	Optical micrograph of protein patterns formed on the porous silicon surface by electron beam irradiation.	12
1.6	Cross-section of a typical capillary sensor.	12
1.7	An optical pH sensor based on pH sensitive fluorescent dye.	14
1.8	FE-SEM image profiles of macroporous silicon.	18
1.9	Configuration of various porous media utilized for electro-osmotic pumps including, porous polymer frit, porous glass frit, and macroporous silicon. .	19
1.10	EOP based on DRIE fabricated porous media.	20
1.11	Optical photograph of mesoporous silicon membrane (un-oxidized sample) and of a mesoporous silica membrane (oxidized sample).	22
1.12	Schematic of the flow-through sensing device used in the current study. . . .	27

2.1	Electric Double Layer configuration of macroporous silicon in comparison to the electric double layer of mesoporous silica.	34
2.2	Schematic of EOP frustrated flow profile.	37
2.3	Schematic of EOP flow profile.	37
2.4	Illustration of zeta potential formed due to the charge distribution.	38
2.5	Cross-sectional and top view SEM profiles of mesoporous silicon with different electrolyte and applied current densities.	41
2.6	Optical photograph of the top view of a 550 μm thick un-oxidized mesoporous silicon membrane and mesoporous silica membrane (oxidized sample).	43
2.7	EOP setup utilized earlier by Zheng et al., for the flow measurements. . . .	45
2.8	Schematic of the EOP based on porous silicon.	45
2.9	Experimental setup utilized for EOP flow rate measurements.	47
2.10	Experimental flow rate vs. applied voltage for the EOP based on mesoporous silica membrane.	48
2.11	Experimental flow rate vs. applied voltage for the EOP based on macroporous silicon membrane.	50
2.12	Experimental setup utilized for EOP pressure capacity measurements. . . .	51
2.13	Measurement setup utilized for pressure readings of EOP.	52
2.14	Experimental maximum pressure vs. applied voltage for the EOP based on mesoporous silica membrane.	52

2.15	Experimental maximum pressure vs. applied voltage for the EOP based on macroporous silicon membranes.	53
2.16	Theoretical maximum pressure generated vs. pore size of the porous silicon membrane.	55
2.17	Equivalent resistance of DI water and porous silicon sample in the EOP configuration.	57
2.18	Fluid permeability setup used to check the fluid flow across the porous membrane in the EOP.	58
2.19	FESEM image of EOP mask pattern formed by selective porousifying of silicon.	60
3.1	Silicon transmission from 200 nm to 1000 nm in a 100 μm thick silicon substrate.	63
3.2	X-ray diffraction spectra of amorphous quartz substrate superimposed over the spectra of mesoporous silica.	66
3.3	Transmission spectra for a typical mesoporous silica samples.	68
3.4	Ellipsometric configurations for angular transmission and reflection spectra for mesoporous silica samples.	71
3.5	Angle resolved transmission spectra measurements from - 45° to + 45° for Sample A.	72
3.6	Variation of transmitted intensity vs. angle of incidence for for Sample A at 900 nm, 1200 nm and 1500 nm.	73

3.7	Angle resolved reflection spectra from 20° to 70° for Sample A.	74
3.8	Variation of reflected intensity vs. angle of incidence for Sample A at 900 nm, 1200 nm and 1500 nm.	75
3.9	The measured refractive index (n) and extinction coefficient (k) of the mesoporous silicon Sample C (un-oxidized sample).	76
3.10	The measured refractive index (n) and extinction coefficient (k) of the mesoporous silica film (oxidized sample).	77
4.1	Absorbance spectra corresponding to intensity forms of cresol red (sodium salt).	84
4.2	Schematic of the flow-through sensing device used in the study.	86
4.3	Fixture of the flow-through sensing device used in the study.	87
4.4	SPEX FLUOROLOG 1681 fluorometer setup utilized for fluorescence measurements.	87
4.5	Hypothetical configurations for dye immobilization on porous silicon. . . .	89
4.6	Chemical structure of fluorescein-5-isothiocyanate and fluorescein.	91
4.7	Images of porous silica untreated (left), immersed in fluorescein solution (middle) and fluorescein covalently bonded (right).	91
4.8	Variation of refractive index of fluorescein in the 300 - 1000 nm wavelength range.	92
4.9	Normalized fluorescence excitation spectra of fluoroscein (1.00 mM) in buffer solution.	93

4.10	Normalized fluorescence excitation spectra of fluorescein immobilized on porous silica.	94
4.11	Relationship between pH and excitation ratio of fluorescein in buffer solution.	95
4.12	Relationship between pH and excitation ratio of fluorescein in porous silica.	96
4.13	Plot of HA% and A-% of fluorescein vs. pH in buffer solution and porous silica.	97
5.1	Atomic layer deposition of Al ₂ O ₃ films in porous silicon.	105
5.2	A preliminary test sequence for measuring different pH in a dynamic flow-through fluorescence experiment.	107
5.3	Setup utilized for dynamic flow-through fluorescence experiments.	108
5.4	Bowing of mesoporous silica sample during thermal oxidation.	110
5.5	Silicon nanorods fabricated using electrochemical anodization under high current density.	111

List of Tables

2.1	Experimental conditions and the etch parameters for mesoporous silicon fabricaton.	40
2.2	Physical characteristics of mesoporous silica in comparison to other porous membranes.	44
2.3	Flow rate of the EOP pump against the applied voltage for mesoporous silica membrane.	48
2.4	Flow rate and pressure comparison from this work with literature.	49
2.5	Pressure of the EOP pump against the applied voltage for mesoporous silica membrane.	50
2.6	Parameters for current (I) and power calculations for EOP	56
A.1	Boron dopant implantation conditions for improving backside silicon conductivity- Porous silicon formation.	130
A.2	Experimental conditions for the 2 μ m pattern transfer.	138

Acknowledgments

I take this opportunity to express my gratitude to my advisor Prof. Paul Bergstrom for his guidance and mentorship, I have learnt a great deal both in the lab and life. I have enjoyed working with him and benefitted a lot from sharing his valuable insights in my research and numerous discussions over the years. In particular, I have gained a lot from the liberty he has given me for performing my research at the same time being available when I am facing a challenge. In addition, I am able to develop professionally with the numerous opportunities provided by him through international conference presentations and publications in reputed journals at national and international venues. Various graduate classes that I have taken from him helped me gain in-depth knowledge of semiconductor and MEMS technologies.

I am thankful to my dissertation advisory committee members, Prof. Sarah Green, Prof. Christopher Middlebrook and Prof. Warren Perger for reviewing this work and for their valuable inputs.

The collaboration with Ms. Qili Hu and Dr. Green from the Department of Chemistry at Michigan Technological University has been excellent and has resulted in the successful testing of the flow-through sensing device. Their primary contribution is presented in Chapter 4 which includes developing the chemistry and techniques involved in

the immobilization of optical dyes on mesoporous silica templates and further conducting fluorescence measurements. Ms. Hu has conducted several fluorescence experiments to identify the best possible mechanism for fluorescence testing and some of the important results are presented in this document. In addition, the collaboration has resulted in a conference paper that was presented at the IEEE-NANO meeting, Portland-OR, August 2011. Karumbaiah Chappanda Nanniah has contributed to some theoretical analysis and experimental testing of electro-osmotic pump with mesoporous silica membranes as outlined in Chapter 2. This collaboration has also resulted in a conference presentation at the PSST 2010 meeting in Valencia-Spain, March 2010.

Faculty members at MTU including, Prof. Hackney, Prof. Jaszczak, Prof. Borysow, and Prof. Kulkarni were kind to share their views on aspects related to my research. Special thanks to Mr. Bill Knudsen for his valuable inputs and sharing his expertise in various micro-fabrication tools. I am thankful to Mr. Owen Mills and Mr. Ed Laitila for their advise on various optical characterization tools available in ACMAL, MTU. Many thanks to Mr. Michael Chase, Mr. Mark Sloat, and Mr. Mark Kilpela for their support with the instrumentation. I would also like to acknowledge the support of the secretaries (administrative staff) in the ECE department, MTU.

I would like to acknowledge Dr. Debra Charlesworth's effort in helping me with suggestions in the preparation as well as for her feedback in improving this document. Many thanks to Ms. Nancy Byers for keeping me posted with her inputs on grad school

documentation. I am thankful for the support from Ms. Thy Yang, Ms. Tara Evans, Ms. Jenny Pindral, and Ms. Greta Gustafson from the IPS at MTU. Many thanks to Mrs. Aparna Pandey, Prof. Ravi Pandey and Prof. Bergstrom's family for their support. I would also like to acknowledge Dr. Sue Hill's help with some graphics that I have used in my doctoral presentation. Many thanks to Gowtham for providing the LaTeX template.

I have enjoyed working with fellow graduate students in Bergstrom's group over the years, some of them include; Jin Zheng Wallner, Santosh Karre, Manoranjan Acharya, Radheshyam Tewari, Shwetha Bolagond, Dawdon Cheam, Rodney Snow, Michael Oisten, Jaspreet Nayyar, and Tom Daunais. I am thankful for the company and support of friends Lakshmi, Biju, Madhana, Edwar, Julio, Mary Kaminski and Randy over the years.

The authors would like to acknowledge the support for this work in part by Michigan Technological University and in part by the Engineering Research Centers Program of the National Science Foundation under Award Number EEC-9986866. It is a difficult task for me to list the names of several other individuals here that have contributed towards my success directly or indirectly, I would like to thank them all.

Finally, I acknowledge the love and support of my parents, Mrs. Sarojini Naidu, Mr. Naidu, brothers Srinivas, Anand, Raghav and sister Madhu.

Abstract

This work presents an innovative integration of sensing and nano-scaled fluidic actuation in the combination of pH sensitive optical dye immobilization with the electro-osmotic phenomena in polar solvents like water for flow-through pH measurements. These flow-through measurements are performed in a flow-through sensing device (FTSD) configuration that is designed and fabricated at MTU.

A relatively novel and interesting material, through-wafer mesoporous silica substrates with pore diameters of 20 -200 nm and pore depths of 500 μm are fabricated and implemented for electro-osmotic pumping and flow-through fluorescence sensing for the first time. Performance characteristics of macroporous silicon ($> 500 \mu\text{m}$) implemented for electro-osmotic pumping include, a very large flow efficiency of $19.8 \mu\text{L min}^{-1}\text{V}^{-1}\text{cm}^{-2}$ and maximum pressure efficiency of 86.6 Pa/V in comparison to mesoporous silica membranes with $2.8 \mu\text{Lmin}^{-1}\text{V}^{-1}\text{cm}^{-2}$ flow efficiency and a 92 Pa/V pressure efficiency. The electrical current (I) of the EOP system for 60 V applied voltage utilizing macroporous silicon membranes is $1.02 \times 10^{-6}\text{A}$ with a power consumption of 61.74×10^{-6} watts.

Optical measurements on mesoporous silica are performed spectroscopically from 300 nm to 1000 nm using ellipsometry, which includes, angularly resolved transmission and angularly resolved reflection measurements that extend into the infrared regime.

Refractive index (n) values for oxidized and un-oxidized mesoporous silicon sample at 1000 nm are found to be 1.36 and 1.66.

Fluorescence results and characterization confirm the successful pH measurement from ratiometric techniques. The sensitivity measured for fluorescein in buffer solution is 0.51 a.u./pH compared to sensitivity of ~ 0.2 a.u./pH in the case of fluorescein in porous silica template. Porous silica membranes are efficient templates for immobilization of optical dyes and represent a promising method to increase sensitivity for small variations in chemical properties. The FTSD represents a device topology suitable for application to long term monitoring of lakes and reservoirs.

Unique and important contributions from this work include fabrication of a through-wafer mesoporous silica membrane that has been thoroughly characterized optically using ellipsometry. Mesoporous silica membranes are tested as a porous media in an electro-osmotic pump for generating high pressure capacities due to the nanometer pore sizes of the porous media. Further, dye immobilized mesoporous silica membranes along with macroporous silicon substrates are implemented for continuous pH measurements using fluorescence changes in a flow-through sensing device configuration. This novel integration and demonstration is completely based on silicon and implemented for the first time and can lead to miniaturized flow-through sensing systems based on MEMS technologies.

Chapter 1

Motivation And Goals

1.1 Introduction

Micro-Total Analysis Systems (μ TAS) and micro-Fluidic Injection Analysis (μ FIA) are some of the prominent analytical techniques that use micro-fluidic technologies to identify and quantify various pollutants. Important challenges in the implementation include the concentration of the sample (to increase the signal strength) and isolating the signal from interference from other species present in the analyte. This requirement necessitates the need for accurate, sensitive and efficient detection technologies. Aspects related to filtration, separation and identification have lead to the development of various technologies that include magnetic, electro-kinetic and optical sensing.

Typically sample characterization involves manually collecting samples or they are acquired through other means of transportation for testing and analysis in the laboratory. This process is time consuming and can be expensive. In addition, an important drawback with these systems includes degradation of the integrity of the sample during transportation. This limits the accuracy of detection and hence there is a need for continuous flow-through detection systems that provide direct and immediate information. Micro Electro Mechanical Systems (MEMS) technologies that are based on silicon are the current state of technologies that are increasingly implemented in areas such as accelerometers in automobiles, optical sensors for display technologies, and energy harvesting etc.

An important parameter, pH, is a measure of the acidity of a solution and is a measurand commonly used in aquatic studies. The pH influences the solubility of different materials that are carried by waters that reach lakes and reservoirs. Water that enters lakes and rivers from irrigation, farming, construction, laboratories, drains, hospitals and other industrial sources when untreated can carry harmful elements (iron, lead, ammonia, mercury etc.) and hazardous wastes that can affect the aquatic life and ecosystem [1]. Hence, it is important to have devices that can quantify the amount of contaminants in a short time. The growing need for miniaturized and portable devices to separate and detect different species has greatly increased and created significant interest in micro-fluidics [2]. An important component of these portable devices is a micro-pump which is used for transferring fluid across the various testing phases.

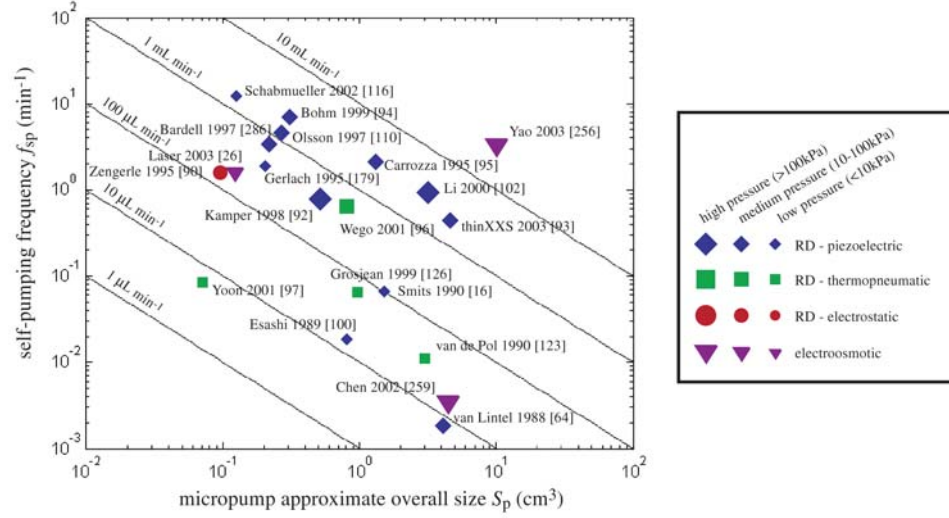


Figure 1.1: Comparison of various micropumps with maximum flow rate (Q_{max}), maximum pressure (P_{max}), and package size S_p [3]. [Permission in Appendix].

In general, micropumps are categorized into reciprocating (mechanical) and dynamic pumps (non-mechanical). The different micropumps that are fabricated using the various micro-fabrication technologies are shown in Fig. 1.1 [3].

For reciprocating pumps, pressure is generated by a periodic compression and expansion of a fluidic volume with the aid of moving surfaces that are interior to the pump. Some of the examples of reciprocating pumps include, electromagnetic, piezoelectric, thermo-pneumatic, and electrostatic pumps. For applications that require highest pressures, reciprocating are usually preferred in which the fluid profile is described as a pulse like motion. In contrary to reciprocating pumps, dynamic pumps produce pressures as a result of fluid that gains momentum as it moves through the pump. Dynamic pumps are categorized into electro-osmotic, magnetohydrodynamic and ultrasonic pumps.

Advantages of using these pumps include, they produce constant pulse-less flow, and utilize fewer components and can be fabricated in a much smaller scale compared to reciprocating pumps [4].

Electro-Osmotic pumps (EOP) have evolved to play a significant role in applications such as micro-flow injection analysis (μ -FIA), micro-channel cooling system, volumetric nano-titrations, and micro-fluidic liquid chromatography systems (μ -LC) for fluid transport at micro and nano-scale [5]. EOPs work on the principle of creating a flow in a fluid by application of electric field across a porous membrane and are highly desirable for miniature fluidic applications as they work without any mechanical parts.

1.2 Flow-Through Sensing Technologies

1.2.1 Background

Optical fiber pH sensors have been used quite extensively in the past many years for sensing applications. These sensors have merits associated with electromagnetic immunity, smaller size, and good mechanical flexibility. These sensors can also be implemented for non-invasive processes due to the fact that they do not have electrical contacts at the sensing element [6]. Some drawbacks including the fact that during the implementation, optical fibers come in contact with sample (analyte) under study and break thereby reducing their

lifetime. The interaction between the optical field of the fiber with the environment of the analyte gives out useful information used for analysis [7].

FIA systems were first introduced by Ruzicka in 1975. Flow based systems have merits compared to other instrumentation analysis as liquid samples under investigation are injected into moving columns of carrier stream of liquid as they pass to the detector [8]. Flow based electrochemical detection is categorized into the following types, a) amperometric detection, b) potentiometric detection, c) optical detection, d) atomic absorption spectroscopy, e) fluorescence, and f) chemiluminescence. Various methodologies and techniques that are commonly implemented to realize optical sensing are presented in following sections.

For FIA applications, a controlled pumping with a precise flow rate is very important for fixed volume sampling. Peristaltic pumps with few or no moving parts are commonly found in FIA systems for fluid transfer in various transport and testing stages. EOPs that utilize porous boric glass core and porous sintered glass frit were reported by Gan et al., and Yao et al. These pumps have demonstrated figures of merit of 0.9 - 30 $\mu\text{L}/\text{min}/\text{V}/\text{cm}^2$ flow rates per unit applied voltage and unit area with pressure per unit voltage performances of 304 - 1013 Pa/V [9], [10]. Porous silicon membranes are desirable for the EOP applications compared to others due to compatibility with current micro processing technologies that are based on silicon [11].

1.2.2 Detection of Lead: Flow Injection System

Various chemical sensors are explored by Zusman et al. by trapping different reagents in a porous glass network. A distinctive color change is observed as the sample under study (metal cation, inorganic anion, and protons etc.) interacts with the trapped or immobilized reagent. In their study, they detected Lead by using immobilized reagent Gallocynine (7-dimethylamino-4-hydroxy-3-oxo-phenoxazine-1-carboxylic acid) in a sol-gel glass matrix with a color change from blue to violet in a 30 min reaction period [12].

Similarly, Yusof et al. have detected trace levels of Lead using a flow injection system where Gallocynine was immobilized on a copolymer as a supporting base in an optical fiber which is then incorporated in a flow injection system. As can be seen in the Fig. 1.2 (a), the probe loaded with XAD 7 bead is inserted in the flow cell. Sample solution with Lead is introduced through the injection port that is connected to a peristaltic pump. During the detection phase, light from the halogen lamp interacts with the column of solution in the flow cell and is reflected back to the benchtop spectrometer through the optical fibre for detection.

The interaction between the Lead solution and Gallocynine results in the formation of a complex of Pb (II)-Gallocynine with a change in color from dark blue to violet. This

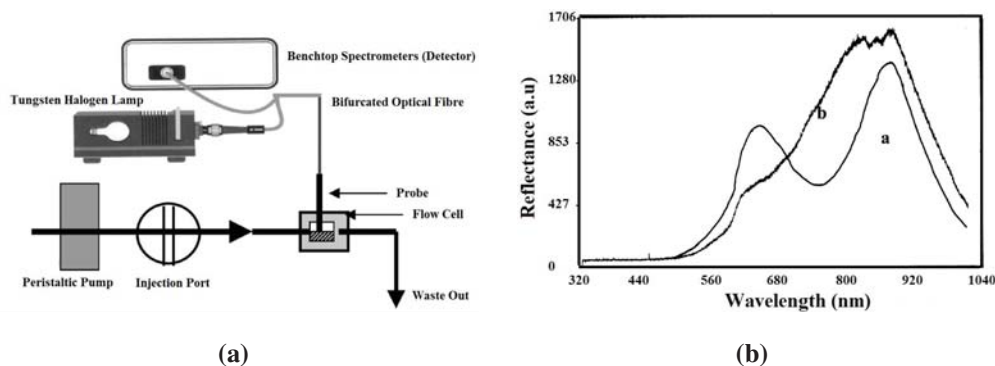


Figure 1.2: (a) flow injection analytical system utilized for the detection of Lead, and (b) plot of reflectance intensity of Gallocynine that is immobilized on XAD 7 polymer, where a) denotes before the reaction and b) after the interaction with 0.2M Pb (II) [13]. [Permission in Appendix].

color change causes an increase in the reflectance as shown in Fig. 1.2 (b) that is used for detection. The peak reflectance intensity was observed at 800 nm and hence is considered for more measurements [13].

1.2.3 Fluorescent Dye Detection Technique With VCSEL

Fluorescence detection technology offers high sensitivity and specificity compared to other methods. To realize portable and miniaturized analysis and sensing systems, various sensing and fluidic components need to be fabricated on the same substrate minimizing the different integration processes [14]. This can be achieved by using the well established semiconductor processing techniques. Thrush et al., have demonstrated the implementation of VCSELs (vertical-cavity surface-emitting lasers), optical filters, and PIN (P-type-Intrinsic-N-type) photo detectors utilizing a single substrate for fluorescent

dye detection technique. In the Fig. 1.3 (a), the intermediate optics is designed for directing the laser beam to the sample, collecting and directing the sensing fluorescence signal to the detector. Another possible configuration, the proximity mode allows the laser beam to interact with the sample directly. The fluorescence signal is collected directly by the photo detector that surrounds the laser source.

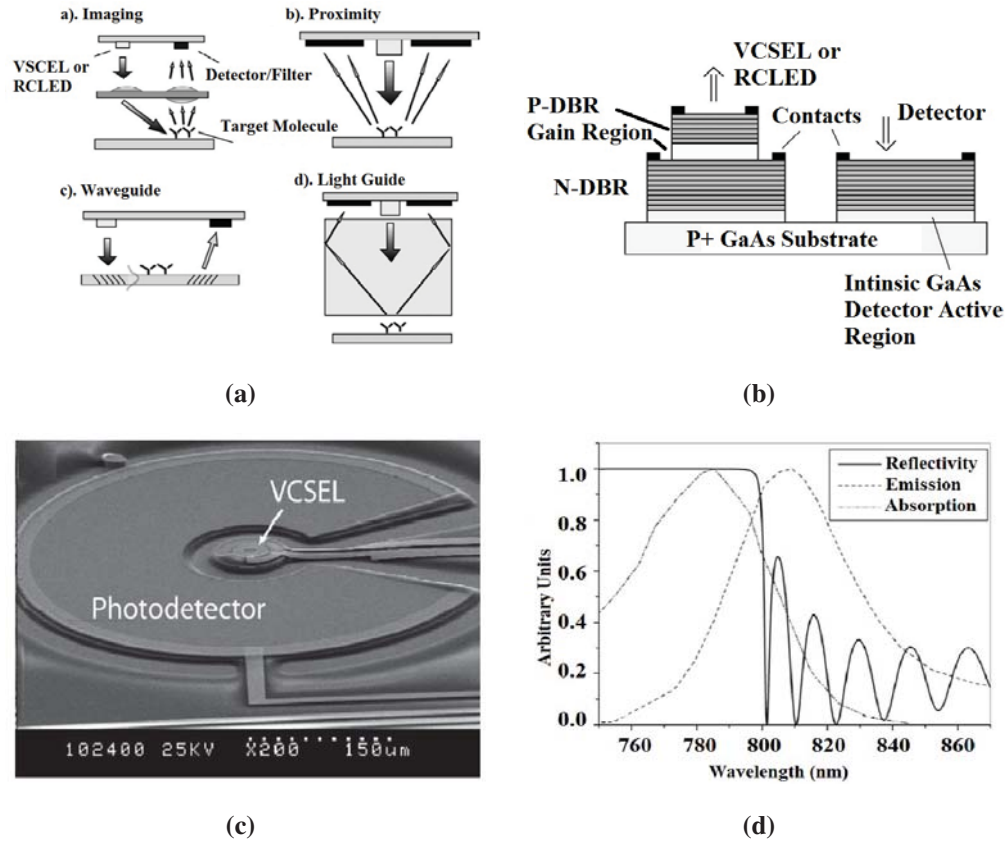


Figure 1.3: Fluorescent dye detection technique with VCSEL, (a) a- imaging, b- proximity, c- waveguide, and d- light guide, (b) integrated device with laser, detector and optical filter, (c) integrated configuration of photo detector (on GaAs substrate) surrounding the VCSEL, and (d) theoretical filtering behavior of the DBR (Distributed Bragg Reflector) which is reflective for lasing and transparent during emission. Also shown in the figure is the Li-Cor dye IR-800 spectra for excitation and emission [14]. [Permission in Appendix].

The waveguide configuration involves coupling the laser light into the waveguide using gratings, where part of electromagnetic field associated with the laser beam in the waveguide excites the sample. The emitted fluorescence signal is again captured by the waveguide and is directed towards the detector. The advantageous aspect of the above design is its compact integrated design. The laser that is employed as the excitation source could provide an energetic source to retrieve a strong signal from the sample. This process has drawback with sampling as new samples need to be manually loaded every time and this could be inefficient and time consuming. Light Guide is another configuration that utilizes a glass or a transparent block that couples light between the detector and sample under study. Figure 1.3 (b) shows the integrated device comprising a laser, detector and an optical filter on a single GaAs substrate. Figure 1.3 (c) shows the SEM image of the integrated configuration of photo detector (on GaAs substrate) surrounding the VCSEL. Also seen in the image are the interconnects to the VCSEL and the photo-detector. Figure 1.3 (d) shows the theoretical filtering behavior of the DBR (Distributed Bragg Reflector) which is reflective for lasing and transparent during emission.

1.3 Fluorescence Spectroscopy

Fluorescence assays comprise of chemical compounds called fluorophores which are made of aromatic groups, plane or cyclic molecules that can be introduced into or are intrinsic to the sample under study. Fluorophores absorb light in a specific wavelength and after

excitation re-emit light of higher wavelength known as the fluorescence. The absorption spectra of a fluorophore as shown in the above Fig. 1.4, has an excitation peak at λ_{ex} and an emission peak at λ_{em} [15].

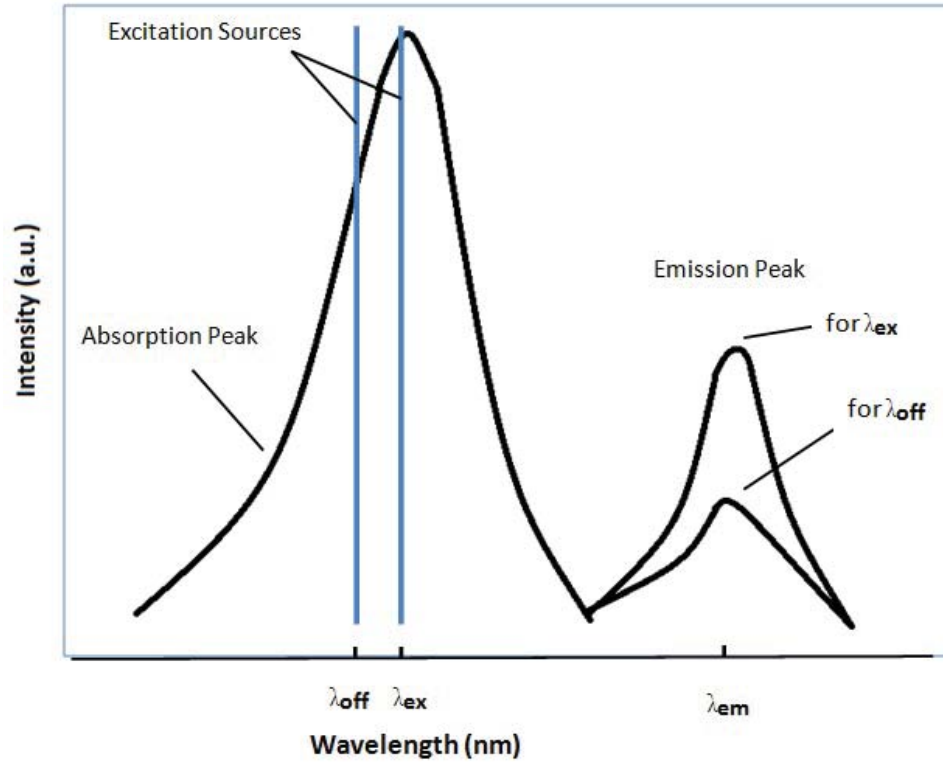


Figure 1.4: Fluorescence intensity spectra with excitation and emission peak [15]. [Permission in Appendix].

For the implementation of fluorescence phenomenon for detection, the immobilization of bio-molecules on a solid substrate and their localization in small regions are important requirements. Porous silicon is an ideal candidate for sensing applications because it has a large specific surface area ($\sim 200 - 500 \text{ m}^2 \text{ cm}^{-3}$), is bio-compatible, and has promising electrical, optical and mechanical properties. More information about porous silicon and its fabrication is presented in Appendix A.

1.4 Dye Immobilization- Porous Silicon Template

A detailed overview of using glucose sensing proteins that are immobilized onto porous silicon templates for blood glucose level measurements is reported by Staiano et al. [16]. Electron irradiation of porous silicon is done in the SEM after the addition of protein solution. After rinsing in de-ionized water, the specific binding of proteins to the porous silicon after irradiation was observed as shown in the Fig. 1.5 (a) and through the fluorescence spectra in Fig. 1.5 (b). The fluorescence spectra were obtained before and after irradiation with the addition of Rhodamine-labeled glutamine-binding protein solution [16]. The binding of the protein occurred as the surface of the porous silicon region was modified.

1.4.1 Immobilization of Dye on Capillary Based Sensors

In the case of capillary based sensors as reported by Weigl et al. [17], the sensing materials are immobilized inside capillary channels (made of glass or plastic) by pumping or drawing solution through the capillary tubes using a peristaltic pump. As the sample solution is drawn through the capillary tubes and is then dried, the dye gets deposited on the inner surface of the channel. Figure 1.6 (a) shows the cross-section of a typical capillary channel and Fig. 1.6 (b) shows the cross-section of a capillary channel with a sensor layer.

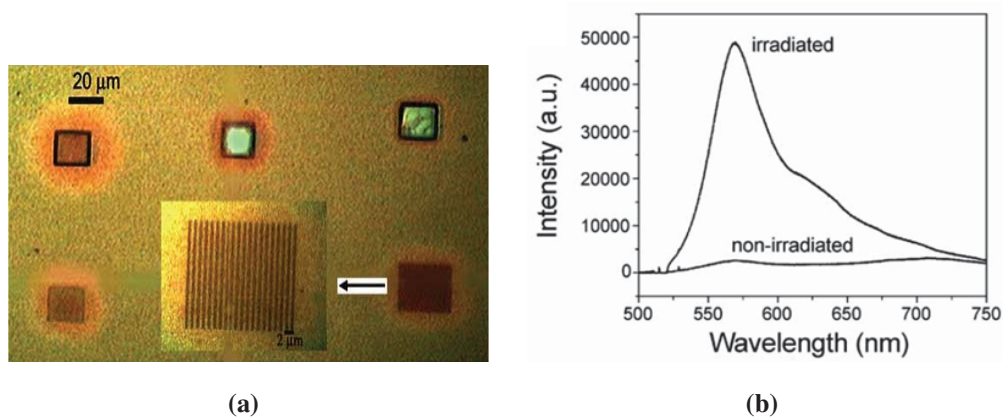


Figure 1.5: (a) optical micrograph of protein patterns formed on the porous silicon surface by electron beam irradiation at different conditions before and after exposure to Glutamine-binding proteins at various conditions, and (b) fluorescent spectra obtained from two regions of the same porous silicon before and after irradiation and exposure to the glutamine binding protein [16]. [Permission in Appendix].

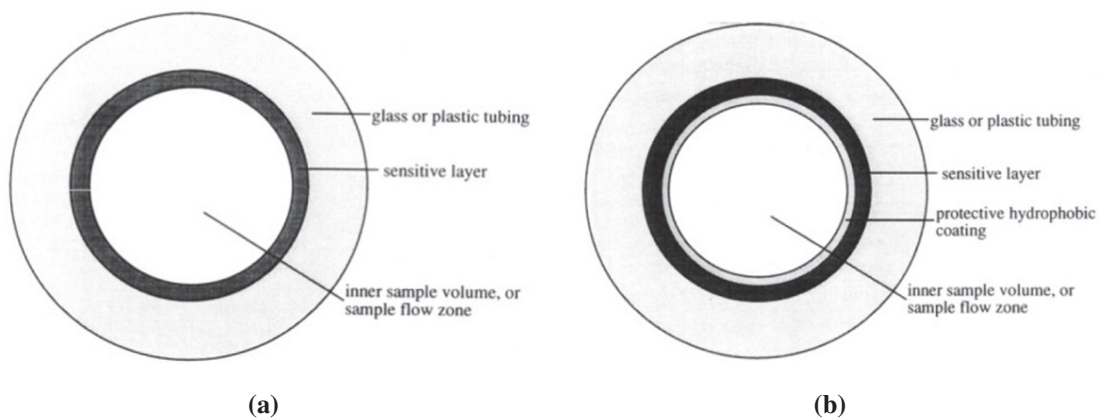


Figure 1.6: (a) cross-section through typical capillary sensor, and (b) one coating is deposited on the inner wall of the capillary and the resulting sensor is used mainly for analyzing gaseous samples [17]. [Permission in Appendix].

1.5 pH Sensor Based on pH Sensitive Fluorescent Dye

An optical pH sensor based on micro-structured polymer optical fiber (MPOF) is considered by Yang et al. In their work, the inner walls of the capillaries is coated with a pH sensing film (eosin as the pH indicator and cellulose acetate as the carrier). This sensor was obtained by drawing the eosin-cellulose acetate solution through the capillaries in the MPOF and then withdrawing the solution (acetic acid) [6]. Figure 1.7 (a) shows the cross-sectional SEM image of the MPOF. Figure 1.7 (b) shows the cellulose acetate modified (top half of the image) and the unmodified (below half of the image). Figure 1.7 (c) shows the cellulose acetate film in the MPOF at an angle. Figure 1.7 (d) shows a magnified SEM image of the sensing film on top of the polymer surface of MPOF.

In order to test the sensitivity of the sensor, buffer solutions consisting of KCl (potassium chloride), HCl (hydrochloric acid) and other phosphate buffers are considered. The sensor is positioned in these solutions for testing and a laser diode is used as the excitation source. The experimental setup of the system is shown in the Fig. 1.7 (e) with the MPOF orthogonal to the laser beam. The fluorescence signal from the MPOF is coupled through the detector fiber to the spectroscopy. The measurements are conducted in the 540 - 650 nm range as different pH solutions are introduced and is shown Fig. 1.7 (f). For the pH range 2.4 - 4.5 for these wavelengths, the fluorescence intensity increased with an increase in pH.

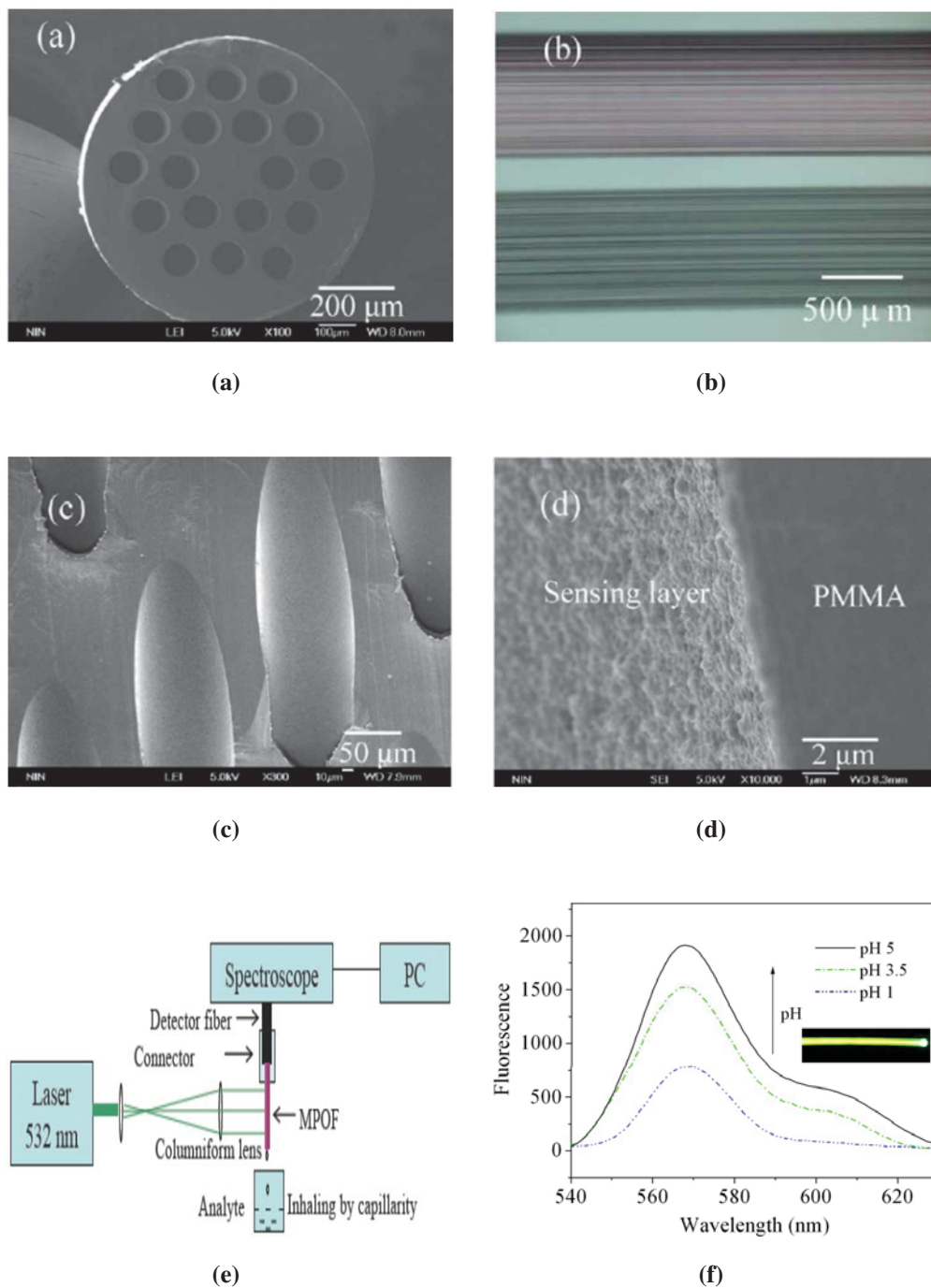


Figure 1.7: SEM images of MPOF, (a) cross-sectional image of MPOF, (b) cellulose acetate modified (above) and unmodified (below) film, (c) cellulose acetate layer at an angle, (d) sensing film on PMMA, (e) experimental setup with MPOF, and (f) fluorescence response of MPOF sensor to various pH solutions at different wavelengths [6]. [Permission in Appendix].

1.6 Flow-Through Sensing System Requirements

It is evident that there is a definite need for a technology that is simple, efficient, and portable and that can provide an output signal that is reliable for a thorough and continuous measurement of an analyte under study. In particular, monitoring the quality of waters in lakes and reservoirs has a immediate need and knowledge of pH is required. In addition, it is desirable that the new technology can be scalable and be integrated with current state of art of miniaturization that is based on MEMS technology which primarily uses silicon as a base material. This miniaturization of the sensing device will make it portable and reduce the time involved in implementation at a short notice and will help sample the area under study at multiple locations without incurring additional costs. Hence, there a need for a new pH sensing method that is completely based on silicon.

From the literature review, the fundamental requirements for realizing a complete flow-through system for a thorough measurement includes;

1. A simple pump that can provide reasonable flow rates and pressure capacities and do not have any moving parts. Micro pumps are a critical components of micro total analytical systems (μ TAS), micro-fluidic systems, lab-on-a-chip and other miniaturized detection systems. EOPs have been demonstrated for high pressures and flow rates without any moving parts.

2. A pump media that can be integrated into devices or systems that are based on MEMS technology. MEMS based technologies are highly desirable due to the wealth of information available for silicon which is the base material for microelectronics and micro-fabrication.
3. A pump media that could be produced in batch process and is reproducible with similar pore morphology.
4. A pump media that can be tailored to obtain a wide range of pressure capacities (10s - 100s of kPa) and flow rates (μ l to mL) with the application of 10 - 100 volts.
5. A template for effectively immobilizing the sensing materials.
6. A template that is inert to common solvents like water and is bio-compatible for applications related drug delivery in medical fields.
7. A good understanding of the fabrication and material properties of the template material. The optical and mechanical properties are one of the important properties of the template material needed for the device implementation.
8. A sensing mechanism that can provide high sensitivity with reasonable selectivity. Fluorescence sensing using immobilized fluorophores offer high sensitivity and will be studied further in this work.

1.7 Motivation

Since the early discovery of porous silicon by Arthur Uhlir Jr. and Ingeborg Uhlir [18] in 1956 at Bell labs and some other initial studies by Turner [19], there has not been any significant interest in porous silicon until Leigh Canham predicted and demonstrated the luminescent properties of porous silicon which is attributed to the quantum confinement of the charges [20]. Some of the noted applications of porous silicon that were demonstrated include, device isolation in microelectronics by Nippon Telegraph and Telephone Public Corporation [21] and Sony Corporation [22], electroluminescent devices [23], biosensors [24], humidity sensors [25], [26], gas sensors [25], [27], waveguides [28], bioactive implants [29], capacitors [30], micromachining [31], and photovoltaics [20].

Figure 1.8 shows the FE-SEM images of the top-view and cross-sectional profile of macroporous silicon fabricated at MTU. Porous silicon is fabricated using various micro-fabrication processes along with electrochemical anodization of silicon. The pore size and pore density is controllable by choosing appropriate silicon substrate resistivities and anodization conditions. The pores are highly vertical, uniform with high aspect ratio (ratio of pore length over pore diameter ~ 250), with a large surface to volume ratio and large flexible pumping area [11]. Macroporous silicon is a promising material as a pump media for EOP pump and was successfully demonstrated for a maximum pressure capacity (5.2 kPa) and a high flow rate ($11.9 \mu\text{l min}^{-1} \text{ mm}^{-2}$) at 60 volts by Zheng et al. in 2006

[11]. Implementation of this kind of EOP for a flow-through detection is highly desirable and hence will be pursued with different porous membranes and dye immobilized porous silica templates.

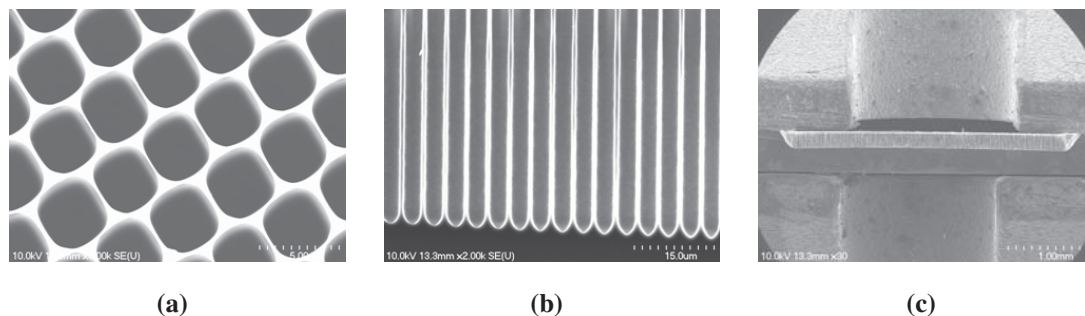


Figure 1.8: (a) top-view FE-SEM image of macroporous silicon, (b) cross-sectional FE-SEM image of macroporous silicon, and (c) cross-sectional FE-SEM image of macroporous silicon at very low magnification.

Earlier, Zeng et al. [32], have demonstrated an EOP fabricated utilizing polymer frits packed with non-porous polymer frits as shown in Fig. 1.9 (a). As outlined in their work, some challenges include fabrication of frits that can handle the EOF (electro-osmotic flow) cycles. Secondary issues include the packaging of dense smaller particles (forming a porous network) in the pumping chamber [32]. Also the size of the particles need to be within a particular distribution such that they do not block the pressure driven flow. In addition, porous media fabricated from these frits are not compatible with standard silicon processing and results in tortuous porous profile with limited surface to volume ratio and limited pumping area.

Yao et al., have fabricated EOP from sintered-glass as shown in Fig. 1.9 (b) with

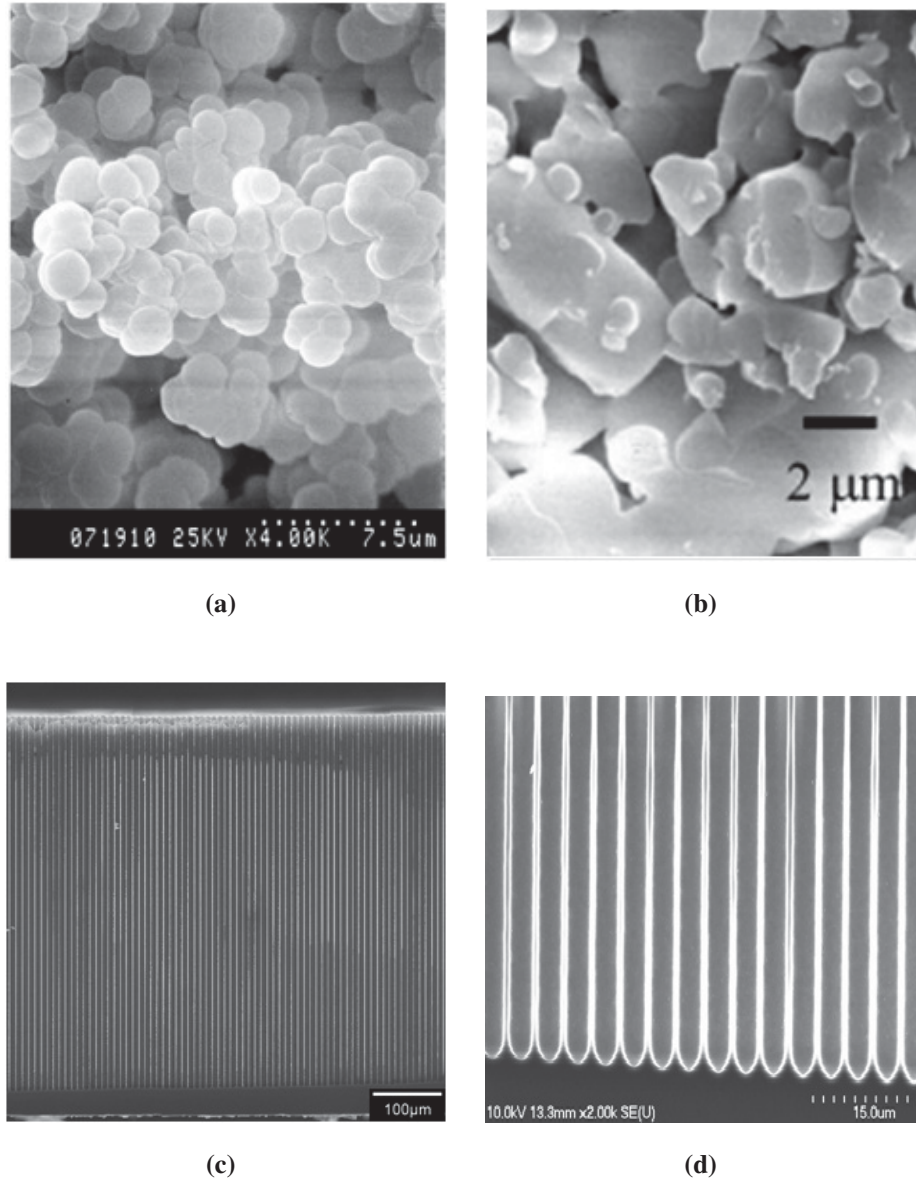


Figure 1.9: SEM images of, (a) porous polymer frit [32], (b) porous glass frit [33], (c) macroporous silicon fabricated at MTU using electrochemical anodization [11], and (d) macroporous silicon fabricated at MTU using a metal mask.[Permission in Appendix].

flow rates of 33 ml/min and pressure capacities of 1.3 atm at applied voltage of 100 volts.

The porous structure in their design includes chemically treated ultra-fine glass frit (filter).

Inconsistencies in the reported values for flow rates and pressure capacities is attributed to the random geometries of the pores in the glass frit structure, deviation from the ideal cylindrical porous structure [33].

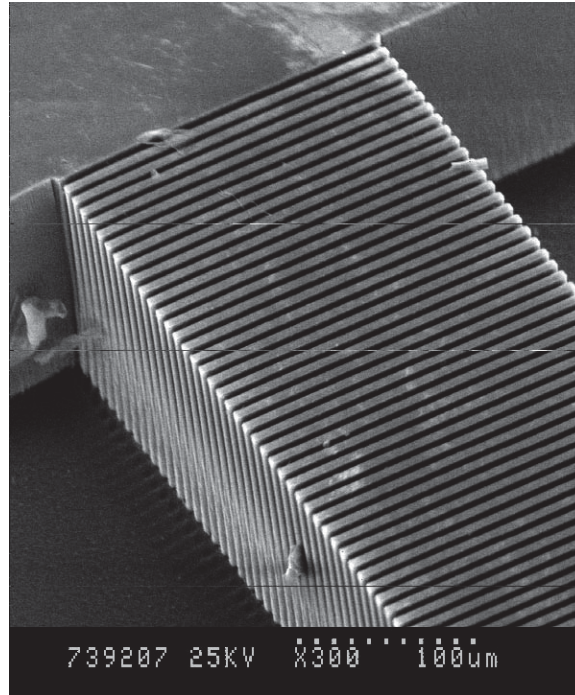
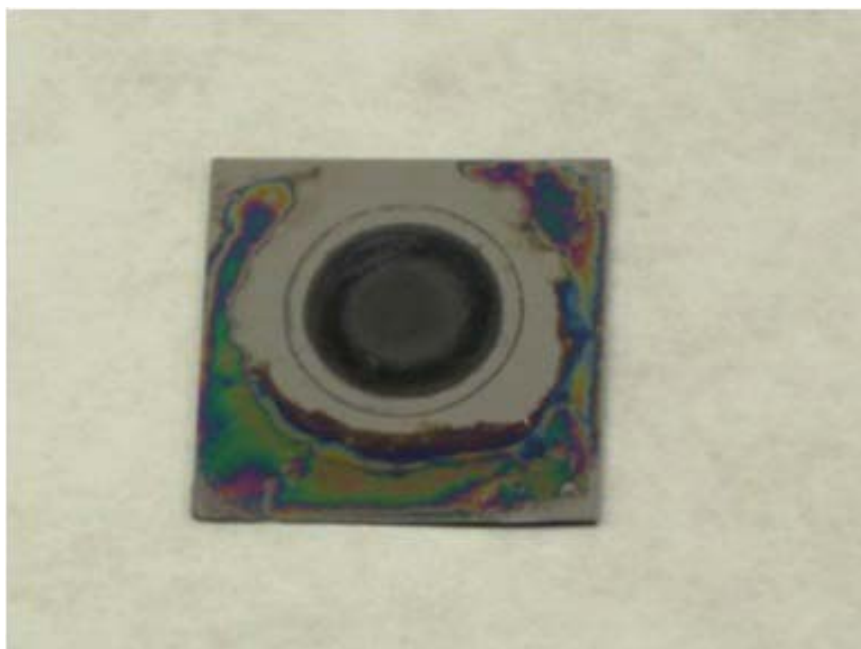


Figure 1.10: EOP based on DRIE fabricated porous media [34]. [Permission in Appendix].

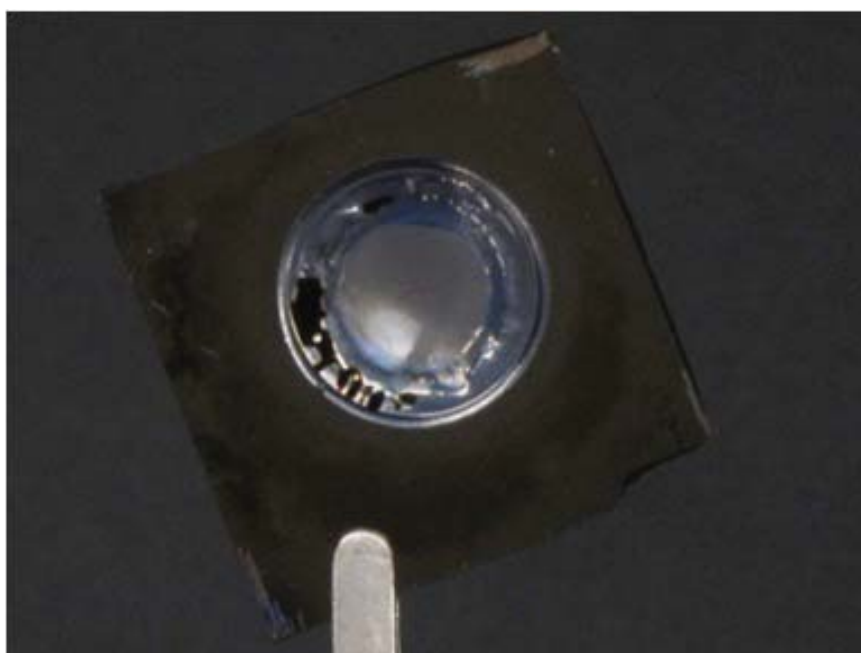
Laser et al., has made some progress on implementation on EOP from silicon substrates for cooling integrated circuits. Their approach has potential for integration of the EOP with CMOS (Complementary Metal Oxide Semiconductor) compatible processes for integrated circuits. The pumping area is defined by deep slots on silicon that is fabricated using DRIE (deep reactive ion etching) techniques as shown in Fig. 1.10 [34]. The process leads to pores with sidewall profiles that suffer from scalloping.

Another class of material known as mesoporous silicon is explored in this study. Unmasked boron doped *p*-type (100) silicon substrates with resistivity of 0.001 - 0.002 Ω -cm and substrate thickness of $525 \pm 25 \mu\text{m}$ are considered as they produce much smaller pores. After anodization, the through-wafer mesoporous silicon samples were thermally oxidized at 950 °C to grow a 10 - 15 nm oxide layer on the sidewalls. As the sidewalls of the pores are in the range of 5 - 10 nm, complete oxidation of the membrane occurs as silicon is fully consumed producing a full wafer thickness porous silica membrane that is optically transparent over a wide range of wavelengths (from UV to near IR). The interesting aspect of the mesoporous silica substrate as shown in Fig. 1.11 pertains to the fact that it is translucent to the human eye and is porous. Details of the fabrication and characterization of mesoporous silicon/silica membranes is outlined in Chapter 3.

Even though silicon with its indirect band-gap has not been traditionally considered a material of choice for luminescent applications, fabrication of a translucent porous silica membrane from silicon can lead to many interesting applications including optical and particle filters. In order to understand the material properties of mesoporous silica, optical properties of porous silica material are spectroscopically characterized from 300 nm - 1000 nm using ellipsometric techniques. Normal transmittance through the membrane was measured and found to be attenuated significantly up to wavelengths of ~ 900 nm but approached the transmittance of bulk silicon for the near infrared and beyond ~ 900 nm - 1500 nm. Angularly resolved transmission and reflection study is performed extending into the infrared regime [35].



(a)



(b)

Figure 1.11: (a) optical photograph of mesoporous silicon membrane (un-oxidized sample) with chip dimensions of $1.5\text{ cm} \times 1.5\text{ cm}$, (b) optical photograph of a mesoporous silica membrane (oxidized sample) $1.5\text{ cm} \times 1.5\text{ cm}$ [35]. [Permission in Appendix].

Mesoporous silica with unique optical properties and high surface area is a potential material for immobilization of host of materials including fluorescent dyes. It is important to have a knowledge of the optical properties of mesoporous silica due to fact that fluorescent and optical dyes will be immobilized on it. Hence, angular transmission, angular reflection and optical constants including, refractive index and extinction coefficients are studied and are presented in Chapter 3. Experiments related to dye immobilization of mesoporous silica template are outlined in Chapter 4.

In summary, from the above discussed technologies and also from the literature review presented earlier, it is possible to integrate a EOP pump that is based on macroporous silicon and mesoporous silica with dye immobilization for a complete flow-through sensing system with details outlined in the later chapters.

1.8 Research Statement

With the increase in demand for miniaturized flow-through sensing systems, there is a high motivation for using silicon technology due to its well established knowledge base. Continuous sampling of analytes without supervision is important in realizing efficient analysis and detection. From literature review, technologies ranging from optical fibers that have dye at the tip and to capillary sensors suffer either from feasibility of implementation or due to the lack of integrity of the detected signal. Porous silicon has been of significant

interest because of its unique optical, mechanical, and electrical properties and has been implemented successfully in optical sensing. Key optical parameters that are used for sensing include refractive index change, fluorescence spectra, and change in reflectivity. Colored dyes have been immobilized onto a porous silicon template to measure the change in pH of the analyte under test. Flow-through optical sensing is a promising technique for achieving reliable and reproducible results with continuous monitoring. The current flow-through sensors have a drawback in terms of pumping the fluid and its implementation. In general, the pumps used for flow-through sensing are peristaltic with moving parts. Also, they have less control on the flow rate and this limits the implementation of the sensor. Electro-Osmotic pumps which are based on the principle of fluid flow by the application of electric field do not have any moving parts and the flow rates can be controlled accurately by the application of electric field. The flow rates achieved using EOPs are highly precise in the nano and micro range, which is a requirement in many biological and chemical applications. Implementation of the EOP device with the optical properties of porous silicon can lead to devices that can have high sensitivity and are efficient. The integration of Electro-Osmotic phenomenon with the optical properties of porous silicon enables a complete flow-through detection system for biological, chemical, and environmental monitoring applications.

1.9 Proposed Flow-Through Sensing Device (FTSD)

Figure 1.12 shows the schematic of the proposed FTSD that is designed and fabricated at MTU. A meso-scale electro-osmotic pump has been fabricated using plexiglass for the FTSD configuration that is designed for pH sensing of fresh waters using indicator dyes that are immobilized on porous silica templates. The fabricated FTSD configuration is a modification of the earlier demonstrated porous silicon based EOP device. The pumping area for this configuration is 0.07 cm^2 which is accounted by measuring the porous area. As shown in Fig. 1.12, there is an additional port on the FTSD to load the sample and refill the reservoir. The exterior walls of the fixture are mirror polished to reduce scattering of the signal during detection. The dye coated mesoporous silica sample is held in a slot that is machined on a thin slab of plexiglass.

During the pump operation, an external voltage is applied to the two spiral Pt (platinum) electrodes, the liquid (buffer solution) is pushed from the larger reservoir to the smaller through the porous silicon membrane and then to the capillary exit. The buffer solution interacts with the porous silica chip with immobilized dyes and leads to different fluorescence signals as the pH of the solution is changed. During the sensing phase, the incident light (excitation source) from the lamp source (400 - 600 nm) of the fluorometer passes through the fixture walls and is directed towards the dye coated porous silica membrane. The emitted fluorescent signal captured by the detector and subsequent

measurements are taken. Details of the implementation will be discussed in Chapter 4. The proposed design is a simple but efficient configuration that utilizes macroporous silicon as a pump media to maximize the flow rate and mesoporous silica templates with really high surface area for increased dye immobilization leading to higher fluorescence intensities during fluorescence detection.

1.10 Goals

The entire project is divided into several tasks as listed below. Successful completion of the goals below will lead to a complete flow-through sensing device for pH measurements of waters.

Task 1: Fabricate macroporous silicon membranes with through-wafer pores of diameters $3\ \mu\text{m}$ and depths $> 500\ \mu\text{m}$ in a circle of $3.5\ \text{mm}$ diameter for the pump media using boron doped *p*-type (100) substrates with resistivity of $17 - 23\ \Omega\text{-cm}$. Details outlined in Appendix A.

Task 2: Fabricate through-wafer ($> 500\ \mu\text{m}$) mesoporous silica membranes with pore size in the $10 - 200\ \text{nm}$ range from *p*-type (100) silicon substrates with resistivity of $0.001 - 0.002\ \Omega\text{-cm}$. Details outlined in Chapter 2.

Task 3: Test both macroporous silicon and mesoporous silica membranes as a pump media for an electro-osmotic pump for high flow rates and pressure capacities. Details outlined in Chapter 2.

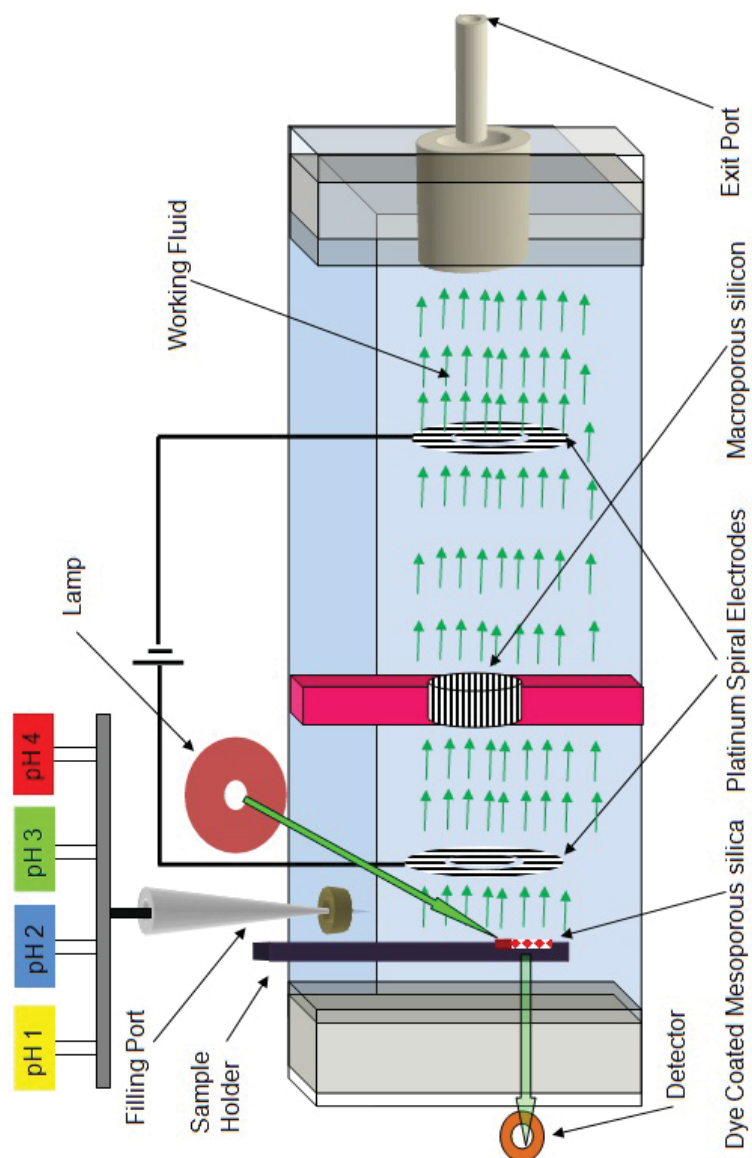


Figure 1.12: Schematic of the flow-through sensing device (FTSD) used in the current study.

Task 4: Perform a thorough optical characterization on mesoporous silica membranes using ellipsometric techniques. Details outlined in Chapter 3.

Task 5: Test the feasibility of immobilizing optical dyes (fluorescein) on mesoporous silica membranes for fluorescence measurements. Details outlined in Chapter 4.

Task 6: Test and characterize the flow-through sensing device by implementing the various

technologies and materials outlined in Task 1 - Task 5.

1.11 Organization of the Dissertation

Chapter 1: Motivation And Goals: This chapter presents a review of the latest techniques that are used for detection and analysis that is based on flow-through sensing systems. In particular, optical sensing that is based on flow-through detection is outlined. Based on the literature review and results from current and previous study, a research statement for the dissertation is proposed.

Chapter 2: Implementation of Porous Silicon Membranes For EOP: Through-wafer mesoporous silicon membranes are fabricated with near vertical and uniform pores with pore diameters of 20 - 200 nm and pore depths of 500 μm by anodizing silicon substrates with resistivity of 0.001 - 0.002 $\Omega\text{-cm}$. Results pertaining to the implementation of macroporous silicon and mesoporous silica membranes for an electro-osmotic pump are presented. Maximum pressure capacities and flow rates of EOP utilizing macroporous silicon and mesoporous silica are measured.

Chapter 3: Optical Properties of Mesoporous Silicon/Silica: Optical properties of porous silicon (mesoporous silicon/mesoporous silica) are measured using ellipsometric techniques which include transmission spectra, reflection spectra, angular resolved

transmission spectra, angular resolved reflection spectra and the refractive indices. A relatively novel and interesting material, translucent mesoporous silica substrates are formed by the complete oxidation of mesoporous silicon substrates.

Chapter 4: Flow-Through Sensing Using Fluorescence Sensing: Based on the research statement, a novel experiment and design for the integration of EOP with the optical properties of mesoporous silica/silicon is presented. Optical dyes are immobilized on porous silica templates for flow-through optical sensing. Fluorescence results from the immobilization of various dyes on porous silica for optical detection are listed. Hypothesis related to the pH measurement of water using the data from fluorescence spectroscopic measurements is presented. A brief summary of challenges that need to be addressed for a complete characterization of the flow through detection is outlined. A flow-through sensing device (FTSD) is designed and is successfully tested. Fluorescence results and characterization confirm the successful pH measurement from ratiometric techniques.

Chapter 5: Conclusions and Future Work: This chapter summarizes the the findings and results from this dissertation work. Future work that can be pursued from the results and knowledge gained from this work will be discussed.

Appendix: Porous Silicon Fabrication: This chapter outlines the methodology, processing techniques, and results implemented in the fabrication of porous silicon.

Various micro-fabrication technologies that include, UV-photolithography, RF-sputtered thin film deposition, thermal annealing, wet etch processing, RIE etch with different gasses, and electrochemical anodization of silicon are presented. Macroporous silicon membranes with a regular array of through-wafer pores ($> 500 \mu\text{m}$) in a 3.5 mm circle utilizing arrays of inverted pyramidal pits is fabricated for the pump media from boron doped *p*-type (100) silicon substrates with resistivities of 10 - 20 $\Omega\text{-cm}$ and 20 - 30 $\Omega\text{-cm}$. Porous silicon that is fabricated using a metal mask has a better pore profile when compared to a dielectric mask.

Chapter 2

Implementation of Porous Silicon

Membranes For Electro-Osmotic Pumps

2.1 Introduction

Electro-Osmotic pumps that utilized porous boric glass core and porous sintered glass frit were reported by Gan, et al. and Yao, et al. [36], [37]. These pumps have demonstrated figures of merit of $0.9\text{-}30\ \mu\text{L}/\text{min}/\text{V}/\text{cm}^2$ flow rates per unit applied voltage and unit area in addition to pressure per unit voltage performances of $304\text{ - }1013\ \text{Pa}/\text{V}$. Current EOPs suffer from low flow rates or low pressure capacities due to larger pore diameters and thin membranes [38]. In general, for specific application, there could be a compromise between

the flow rate and pressure generated by the EOPs. Electro-Osmotic flow (EOF) in micro and nano channels are greatly affected by the dimensions of the capillary. Fluid interaction with the capillary walls becomes more pronounced and significant as the capillary diameters becomes micro and nanoscale. Porous silicon membrane consisting of densely packed parallel channels is used as the pumping media for the pump in this work. With decreasing pore size to nano-scale, it is expected that this pumping media will produce reasonable flow rates and high pressures capacities.

The flow rates and pressure capacities obtained using porous silicon for EOP applications depends on the pore configuration that includes, pore diameter, pore depths and pore uniformity. Since the earlier demonstrated work by Zheng et al., [11] on porous silicon membranes for pore sizes of $\sim 3 \mu\text{m}$ and depths of $500 \mu\text{m}$, there is a strong motivation to pursue and implement porous silicon with pore sizes in the order of 100's of nanometers (nanoporous and mesoporous) for EOP applications. As the pore size becomes smaller, the pressure capacities obtained will be much greater and applications related to drug delivery in medical fields require such high pressures.

2.1.1 Electro-Osmotic Pump Theory

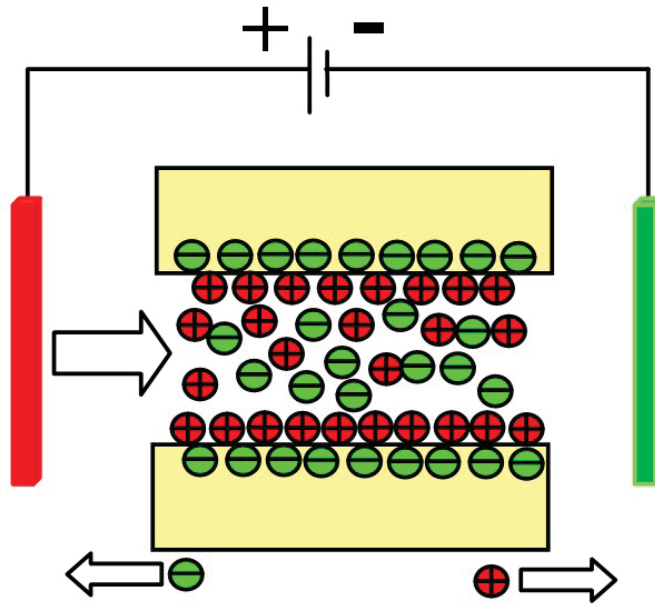
EOPs work on the phenomenon of fluid motion caused by the application of electric field on the ions that are bound to the sidewall of the capillary channels. The working fluid

needs to be a polar solvent having a pH value greater than 4 which is required for the formation of surface charge on the side walls of the pores [39]. The thin layer of SiO₂ on the pore walls when in contact with a fluid of above specifications achieves a negative surface charge due to the removal of H⁺ ions of the acidic silanol groups and hence results in an electrical double layer [EDL] [39]. With the application of external electric field, the ions in the EDL will experience a coulombic force, thereby moving in the direction of applied field and dragging the bulk fluid along. This resultant flow is called electro-osmotic flow (EOF) [39], [40]. Figure 2.1 shows EDL thickness in context of macroporous silicon and mesoporous silicon.

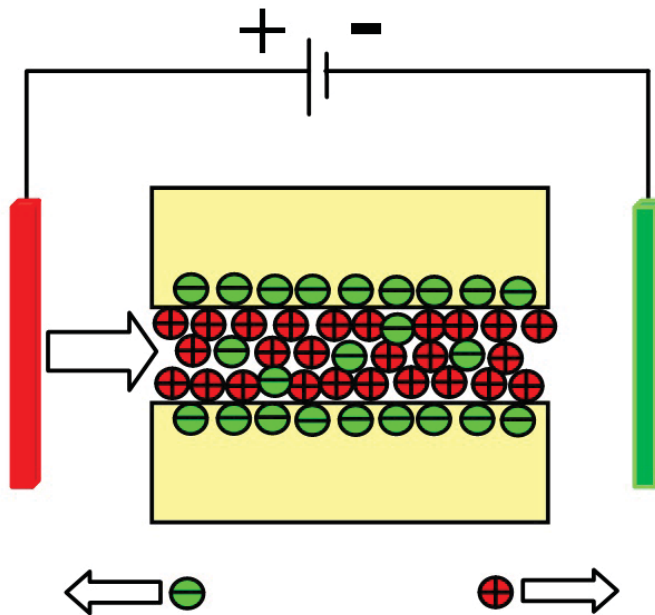
The flow rate of the fluid in the capillary channels becomes significant as the dimensions of the EDL becomes closer to order of the capillary channel size. Considering a single pore channel, the EOF for the porous membrane using Debye-Huckel approximation for zero back pressure is defined by equation Eq.(2.1) [41].

$$Q = -\frac{pA\varepsilon\zeta V}{\tau^2\eta L} \left[1 - \frac{2I_1(a/\lambda_D)}{(a/\lambda_D)I_0(a/\lambda_D)} \right] \quad (2.1)$$

In the Eq.(2.1), ζ is the zeta potential, p is porosity, τ is the tortuosity, L is the length of the channel, A is the cross-sectional area, ε is the dielectric constant of the fluid, V is the potential applied, η is the viscosity, λ_D is the EDL thickness known as the Debye shielding length given by the Eq.(2.2), a is the average pore radius, and I_0 , I_1 are the zero-order and



(a)



(b)

Figure 2.1: (a) EDL pore channel configuration in the case of a macroporous silicon, EDL is much smaller than the pore diameter and, (b) EDL pore channel configuration in the case of a mesoporous silicon, EDL is much larger than the pore diameter.

first-order modified Bessel functions of the first kind, respectively. A good review for the flow pattern is presented in literature and won't be reviewed in detail here [39].

$$\lambda_D = \left[\frac{\epsilon k T}{e^2 \sum_{i=1} Z_i n_{\infty, i}} \right]^{1/2} \quad (2.2)$$

In the Eq.(2.2), k is the Boltzmann constant; T is temperature of the working fluid; and e is the charge of an electron.

The maximum pressure generated across the pores is obtained from Eq.(2.3) [41].

$$\Delta P_m = -\frac{8\epsilon E L \zeta}{a^2} \left[1 - \frac{2I_1(a/\lambda_D)}{(a/\lambda_D)I_0(a/\lambda_D)} \right] \quad (2.3)$$

In the case where the radius of the pore is much larger (>20 nm) than the thickness of EDL, the following approximation is considered [42].

$$\left[1 - \frac{2I_1(a/\lambda_D)}{(a/\lambda_D)I_0(a/\lambda_D)} \right] = 1 \quad (2.4)$$

For specific applications, high pressure values are required and pressures generated from the EOP demonstrated by Zheng et al. are relatively low (5.2 kPa at 60 V) due to the large $3 \mu\text{m}$ pore size of the porous media. As pressure obtained from the porous media

is inversely proportional to the square of the pore radius as shown in equation Eq.(2.3), it is expected that porous silicon with pore diameters ~ 100 nm should produce really high pressure values.

If the radius of pore is smaller than or equal to the EDL thickness, the part containing Bessel function in Eq.(2.1) and Eq.(2.3) can be approximated to as given by [42].

$$\left[1 - \frac{2I_1(a/\lambda_D)}{(a/\lambda_D)I_0(a/\lambda_D)} \right] = \frac{1}{8}(a/\lambda_D)^2 \quad (2.5)$$

Based on the above approximation, the pressure generated will be inversely proportional to the square of the EDL thickness and hence will result in a very high pressure. However, the Debye-Huckel approximation is not very accurate for the case when the EDL of the channel overlaps [43]. Based on the ratio of pore diameter to the EDL thickness, the pump efficiency would vary. It has been estimated that for DI water, the EDL thickness is 100 nm [44]. From the Eq.(2.1) and Eq.(2.3), it can be seen that for high flow rates, the radius of the pore channel should be large. On the contrary, high pressure can be generated if the pores have smaller radius.

Figure 2.2, Fig. 2.3 (a), and Fig. 2.3 (b) show the flow profile in different flow conditions for the EOP. In the presence of a hydrodynamic load, a frustrated flow profile is observed as shown in Fig. 2.2 due to any back pressure present that opposes the electro-osmotic flow. Due to this frustrated flow condition, in extreme cases, the flow

in the pore column can change and flow in an opposite direction [40]. In the case when there is no frictional load present on the pore column, the flow profile has the pattern as shown in Fig. 2.3 (a), the electro-osmotic flow. Fig. 2.3 (b) shows the pressure driven flow pattern.

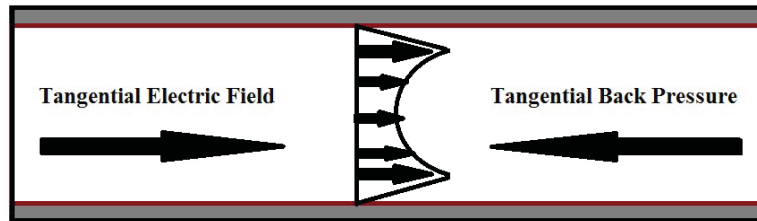


Figure 2.2: Schematic of EOP frustrated flow profile [40].

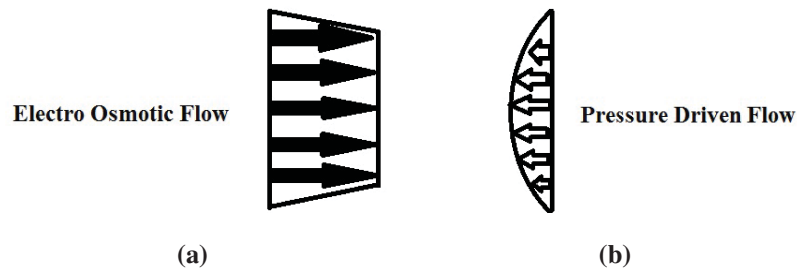


Figure 2.3: (a) schematic of EOP flow profile and, (b) schematic of EOP pressure driven flow [40].

An important parameter, the zeta potential is defined as the potential that is present between the surface pore wall of the porous membrane and the mobile layer of oppositely charged ions that isolate the charges present on the surface of the pore wall from the bulk liquid [42]. It is measured from the pore center to the pore wall with charged species. Zeta potential has an impact on the pressure and flow rates as it determines the thickness of EDL. Zeta potential also gives information regarding the stability of the flow in the pore

channel. The zeta potential cannot be measured but can be extracted from the experimental values of flow rates and pressure. An illustration of Zeta potential is shown in Fig. 2.4 [45].

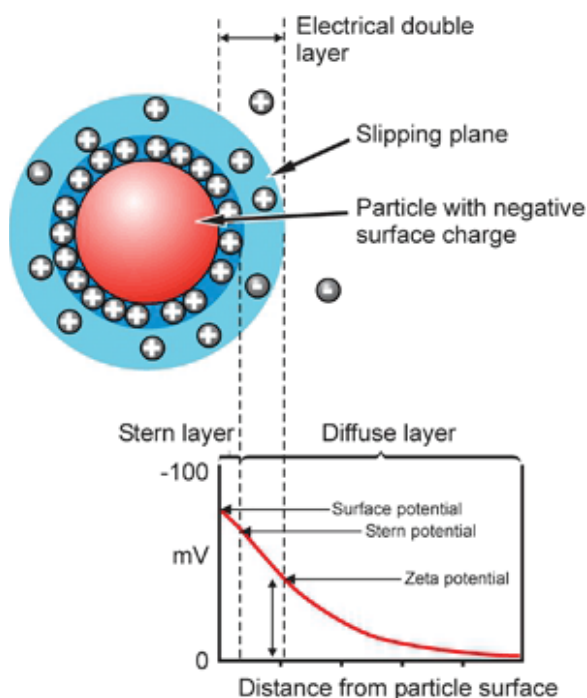


Figure 2.4: Illustration of zeta potential formed due to the charge distribution [45]. [Permission in Appendix].

2.2 Experimental Methods

The experiments for the fabrication of mesoporous silicon utilized unmasked boron doped *p*-type (100) silicon substrates with resistivity of 0.001 - 0.002 Ω -cm and substrate thickness of $525 \pm 25 \mu\text{m}$. Electrolyte solutions considered include, aqueous electrolyte (E1) consisting of 10^{-3}M cetyltrimethylammonium chloride (CTAC) with HF (49%), ethanol, and deionized (DI) water at a volume ratio of 1:2:3 and electrolyte (E2) consisting

of 10^{-3} M CTAC with HF (49%), ethanol, and DI water at a volume ratio of 1:1:1. Current densities of 5, 10 and 20 mA/cm² are applied for the electrochemical anodization. The substrates are treated with buffered HF solution to remove any native oxide to allow ohmic contact between electrode and the silicon substrate for anodization. Through-wafer mesoporous silicon membranes are fabricated by utilizing sacrificial silicon substrates [11]. In addition, boron doped *p*-type (100) silicon substrates with resistivity of 10 - 20 Ω -cm with substrate thickness of $525 \pm 25 \mu\text{m}$ are electrochemically anodized in electrolyte (E1) to form macroporous silicon substrates that are utilized for EOP pumping.

For the EOP test, macroporous silicon, mesoporous silicon, and mesoporous silica membranes are used for the flow rate and pressure measurements. Mesoporous silicon samples are thermally oxidized at 950 °C to form mesoporous silica membranes. DI water with 17 M Ω resistance is used as the working fluid. Spiral platinum electrodes are used for both anode and cathode and are positioned on either side of the porous media. Flow rate and maximum pressure experiments were performed using testing methods outlined by Zheng et al., in 2006 [11].

2.3 Results

2.3.1 Mesoporous Silicon Pore Characterization

Figure 2.5 (a)-(c), (e)-(g) shows the FE-SEM top-view and cross-sectional images of the mesoporous silicon samples at applied current densities of 5mA/cm^2 , 10mA/cm^2 , and 20mA/cm^2 for 1:2:3 electrolyte. Figure 2.5 (d) and (h) show the FE-SEM images of mesoporous silicon samples for 1:1:1 electrolyte at 10mA/cm^2 . Table 2.1 lists the experimental conditions and the etch rate and pore size obtained for the samples used at different applied current densities.

Table 2.1
Experimental conditions and the etch parameters for mesoporous silicon fabrication.

Electrolyte (E)	E1	E1	E1	E2
Current Density [mA/cm^2]	5	10	20	10
Etch Rate [μm]	0.12	0.23	0.4	0.28
Pore Size [nm]	20	40	200	20

It can be seen from the images in Fig. 2.5 that the pore size increases with an increase in applied current density. In general, the pore size varied from 20 nm to 200 nm for current density varying from 5mA/cm^2 to 20mA/cm^2 . The length of the pore is primarily in the $\langle 100 \rangle$ crystallographic direction with unit tortuosity. The side wall thickness of the pore is $10 \pm 5\text{ nm}$. Samples prepared with electrolyte E2 are more robust,

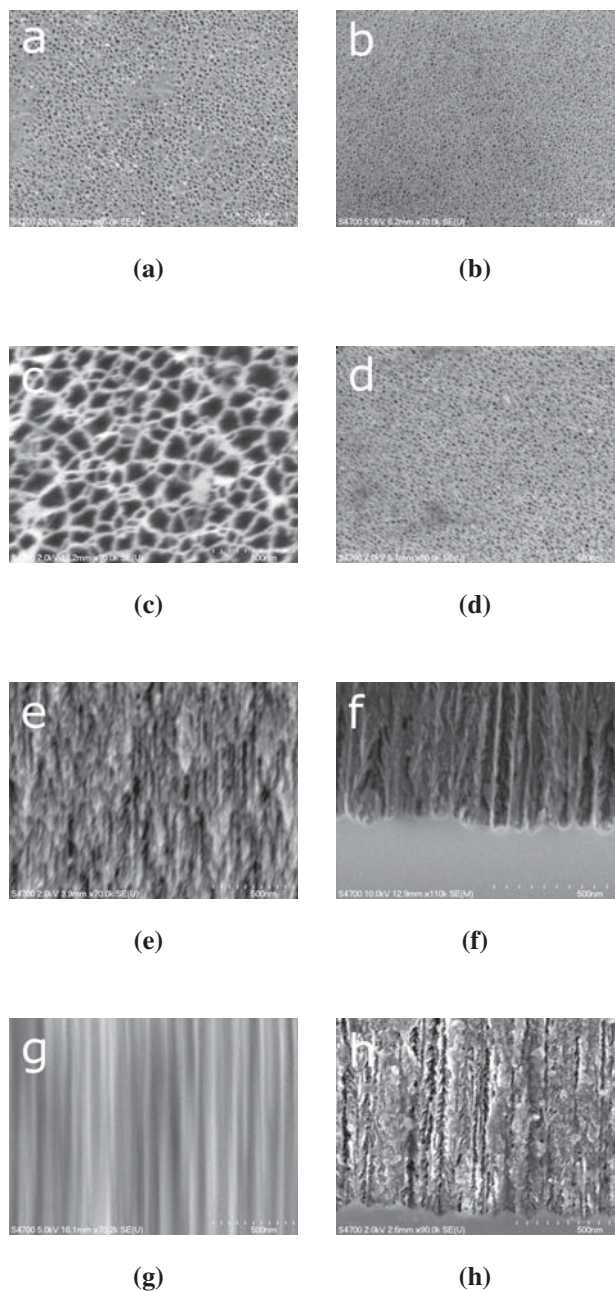


Figure 2.5: (a), (b), and (c) are the top-view images; (e), (f), and (g) are the cross-sectional images of porous silicon samples for electrolyte E1 at 5, 10, and 20 mA/cm² current densities respectively, (d) and (h) are top and cross-sectional view images for the sample in electrolyte E2 at 10mA/cm².

hence are implemented as the pump media for the EOP application. The pore size and porosity can be controlled by changing the applied current density and electrolyte chemistry within certain limits.

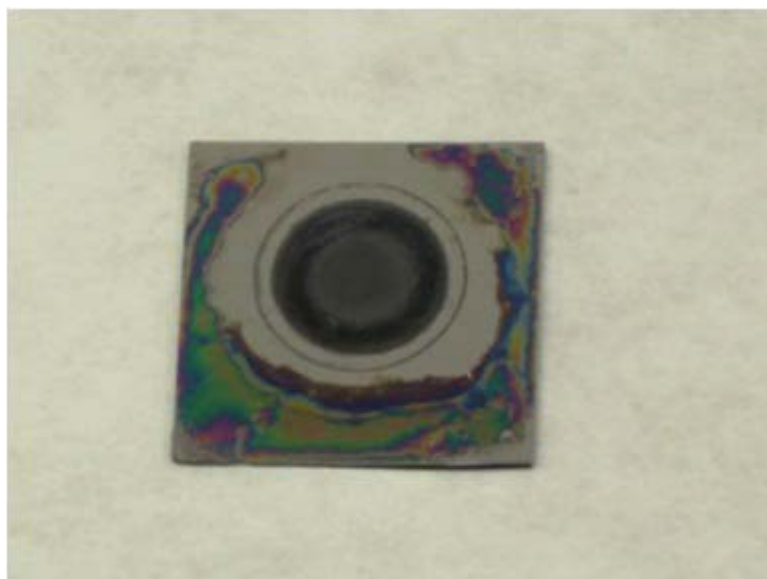
2.3.2 Mesoporous Silica Formation

After anodization, the samples are thermally oxidized in an oxidation furnace at 950 °C to completely oxidize and strengthen the pore walls. Fig. 2.6 (a) and Fig. 2.6 (b) show images of un-oxidized mesoporous silicon and completely oxidized mesoporous silica membranes.

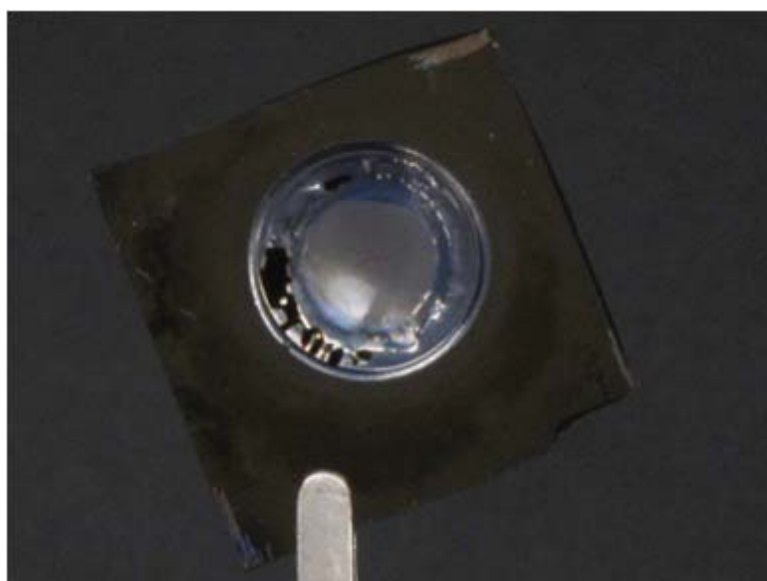
The unique properties of mesoporous silica compared to other materials are listed in Table 2.2.

2.4 EOP Test

To verify the experimental conditions, results obtained by Zheng et al. were reproduced [11]. The flow rate was measured by weighing the mass of the DI water and is converted to volume. A low dead-volume pressure sensor (Honeywell ASDX005G24R) is used to measure the maximum pressure for the EOP with a mesoporous membrane. Figure 2.7 shows the EOP setup utilized by Zheng et al. [11]. Figure 2.8 shows the configuration of the EOP setup.



(a)



(b)

Figure 2.6: (a) optical photograph of the top view of a 550 μm thick un-oxidized mesoporous silicon membrane, (b) optical photograph of a mesoporous silica membrane (oxidized sample).

Table 2.2
Physical characteristics of mesoporous silica in comparison to other porous membranes.

Material	Fabrication Process	Tortuosity	pore size, pore length	Other	Author
Mesoporous Silica	MEMS based processing-electrochemical anodization	~ 1	10-50 nm, $\sim 500 \mu\text{m}$	optically translucent, porous and efficient fabrication	Vanga et al.
Glass	Micro-machined	~ 1	4 cm wide and 1 mm long, 1 μm deep	not expensive	Chen and Santiago
Silica Particles	slurry-packing method	-	500-700 μm diameter	not reproducible	Zeng et al.
Glass Frit	Sintering	-	1.4, 40 mm diameter, 1-2 μm pore, 1-5 mm	not reproducible	S. Yao

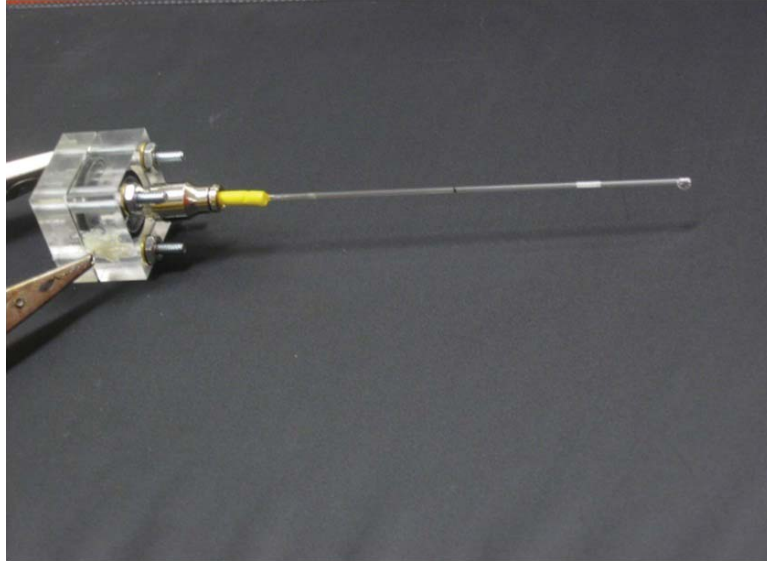


Figure 2.7: EOP setup utilized earlier by Zheng et al., for the flow measurements [11]. [Permission in Appendix].

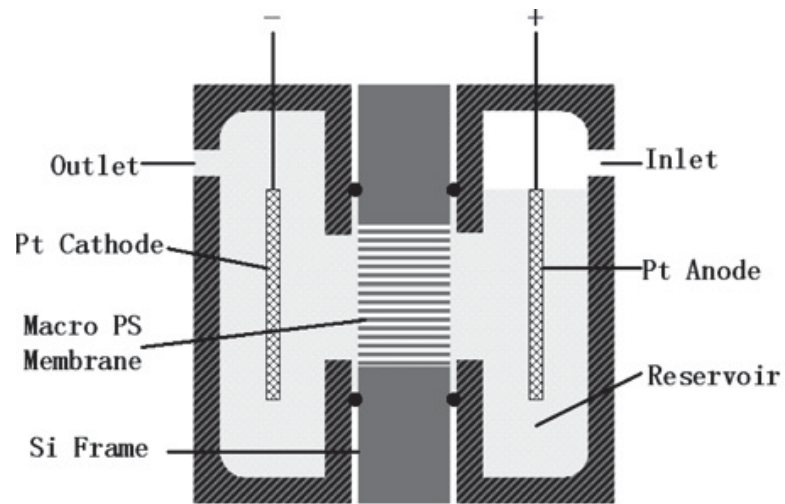
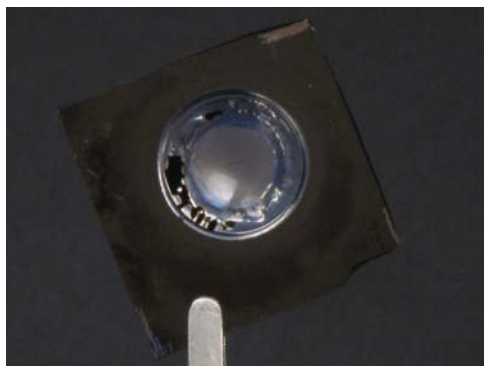


Figure 2.8: Schematic of the EOP based on porous silicon [11]. [Permission in Appendix].

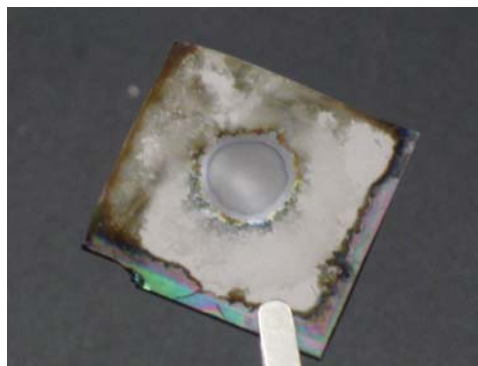
2.4.1 Flow Rate And Pressure Measurements

Flow rates of 20 $\mu\text{L}/\text{min}$ for a applied bias of 100 V and maximum pressures of 7300 Pa is achieved at 80 V for mesoporous silica membranes. The process involved in the measurement of the flow rates is illustrated in Fig. 2.9. Mesoporous silica sample was positioned on to the fixture as shown in Fig. 2.9 (c) followed by securely sealing the sample with a O-ring to prevent any water leakage. DI water is introduced into both sides of the reservoirs of the fixture using a syringe. Voltage from 10 - 100 V is applied, negative bias to the electrode closer to the exit port and positive on the other end. The water exiting the capillary tube is weighed for a fixed period (~ 3 minutes) of time and is converted to volume. Flow rate is measured by taking account of this volume flow over the fixed time by following the figure of merit analysis outlined by Yao, et al. [37].

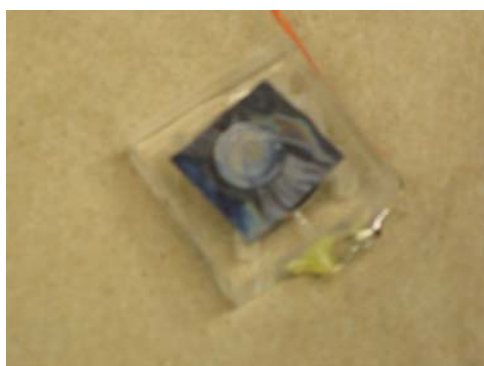
Results for the presented oriented mesoporous silica EO pump demonstrated a 2.8 $\mu\text{L}/\text{min}/\text{V}/\text{cm}^2$ flow efficiency and a 92 Pa/V pressure efficiency. Table 2.3 lists details for flow rates for different voltages for mesoporous silica membranes. Figure 2.10 shows the plot of EOP flow rate against the applied voltage for mesoporous silica membranes. Figure 2.11 shows the plot of EOP flow rate against the applied voltage for macroporous silicon membranes earlier demonstrated by Zheng et al. Flow rates and pressure capacities obtained by different authors is compared with the results in this work as listed in Table 2.4 [42].



(a)



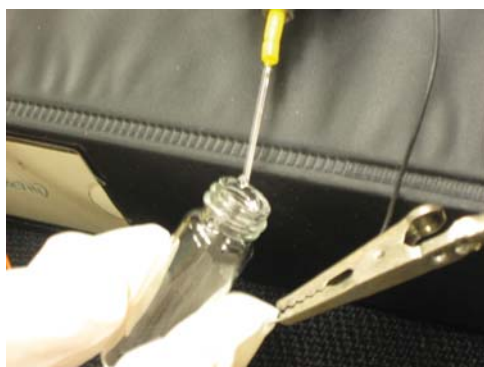
(b)



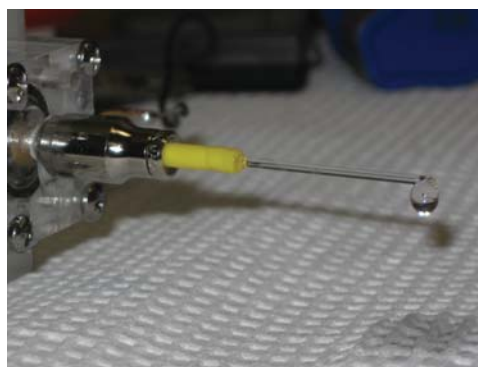
(c)



(d)



(e)



(f)

Figure 2.9: (a) top side of mesoporous silica sample, (b) backside of the mesoporous silica sample, (c) mesoporous silica sample on the fixture for mounting, (d) front side of the reservoir is filled with a syringe, (e) pumped DI water is collected in a vial, and (f) water exiting the capillary tube.

Table 2.3
Flow rate of the EOP pump against the applied voltage for mesoporous silica membrane.

Applied Voltage (Volts)	Flow rate ($\mu\text{L}/\text{min}$)
20	4.67
30	7.33
40	8
50	8.3
60	9.67
70	11.3
80	15.67
90	18
100	20.67

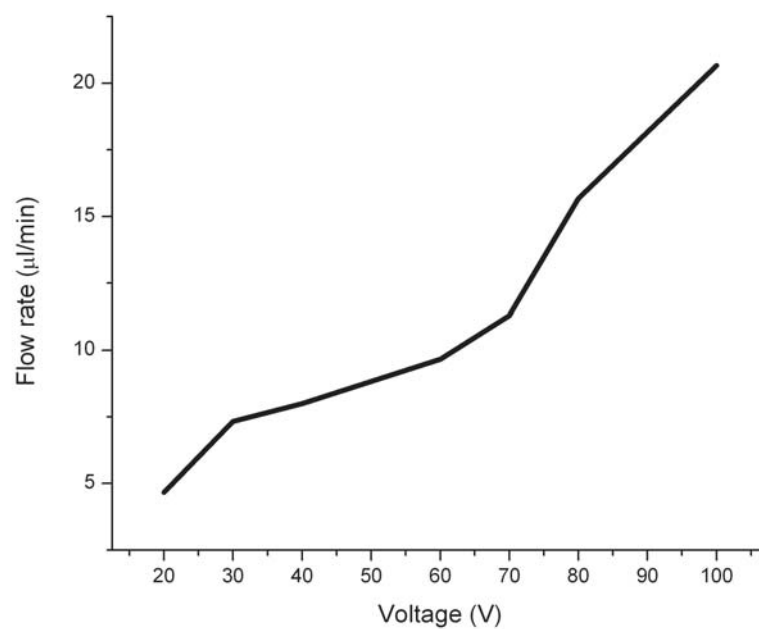


Figure 2.10: Experimental flow rate vs. applied voltage for the EOP based on mesoporous silica membrane.

Table 2.4
Flow rates and pressure comparison from this work with literature
[42]. [Permission in Appendix].

Pressure (kPa)	Flow rate (ml min ⁻¹)	Material (Process)	Working Fluid	Operating Voltage (V)	Author
5.2	11.9	Macroporous silicon (micro-fabrication)	DI Water	60	Zheng et al., 2007
4.48	8	Mesoporous silica (micro-fabrication)	DI Water	60	Vanga et al., 2010
NA	0.00002	Glass (micro-channel)	Water	2700	Jacobson 1994
NR	0.00009	Glass (micro-machined)	Water		
		Sintered glass beads (porous media)	Water, Methanol	2000	Ramsey 1997
150	3.0		NH ₄ OH	500	Gan 2000
5.0	NR	Quartz (micro-machined)	Phosphate buffer	40	Takamura 2001
33	0.015	Soda-lime glass (micro-machined)	Water	1000	Chen 2002
250	0.9	Packed Silica particles (porous media)	Water	1250	Zeng 2002
10	0.17	Si-glass (micro-machined)	Borate buffer	400	Laser 2003
130	33	Sintered glass frit (Porous media)	Borate buffer	100	Yao 2003

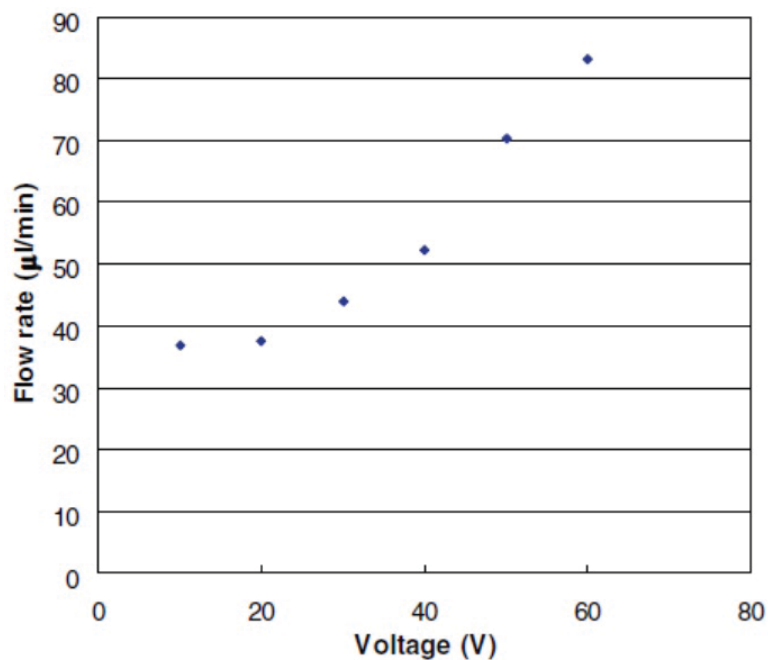


Figure 2.11: Experimental flow rate vs. applied voltage for the EOP based on macroporous silicon membranes [11]. [Permission in Appendix].

Figure 2.12 shows the setup utilized for pressure capacity measurements. The pressure sensor and multimeter voltage reading for the EOP pressure measurement is shown in Fig. 2.13.

Figure 2.14 shows the plot of EOP pressure test against the applied voltage for

Table 2.5
Pressure of the EOP pump against the applied voltage for mesoporous silica membrane.

Applied Voltage (Volts)	Pressure (Pa)
10	36.2
20	319
40	2190
60	4480
80	7380

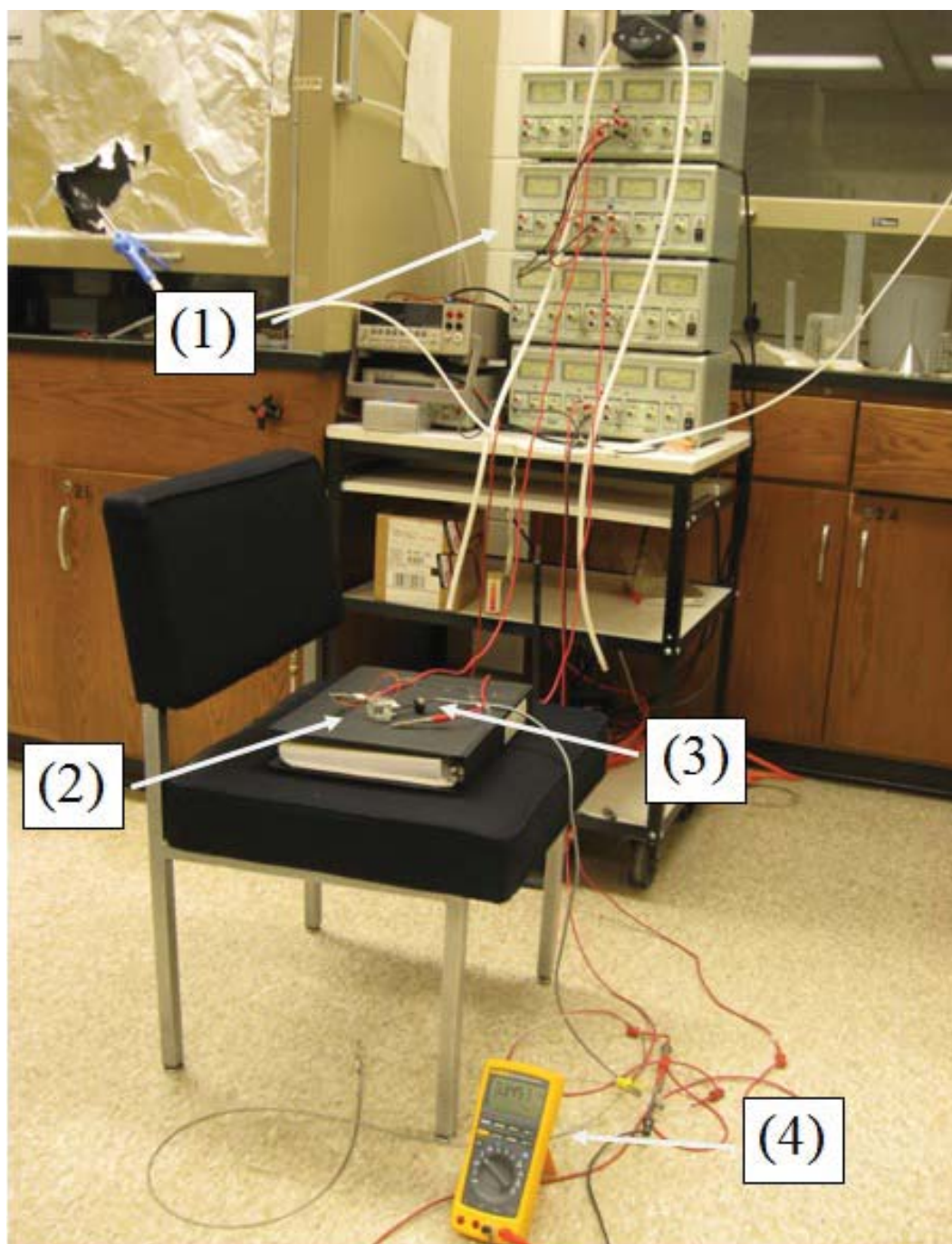
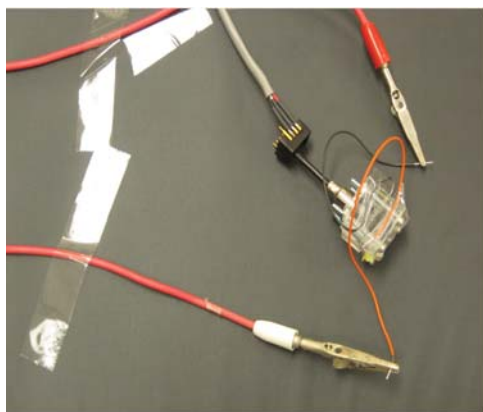


Figure 2.12: Experimental setup utilized for EOP pressure capacity measurements. In the figure, (1) is the voltage supply, (2) is the EOP fixture, (3) is the pressure sensor, and (4) is the multimeter with pressure equivalent reading in volts.



(a)



(b)

Figure 2.13: (a) pressure capacity measurement of the EOP, and (b) voltage reading across the pressure sensor as recorded on the multimeter.

mesoporous silica membranes. Table 2.5 lists the details for this test.

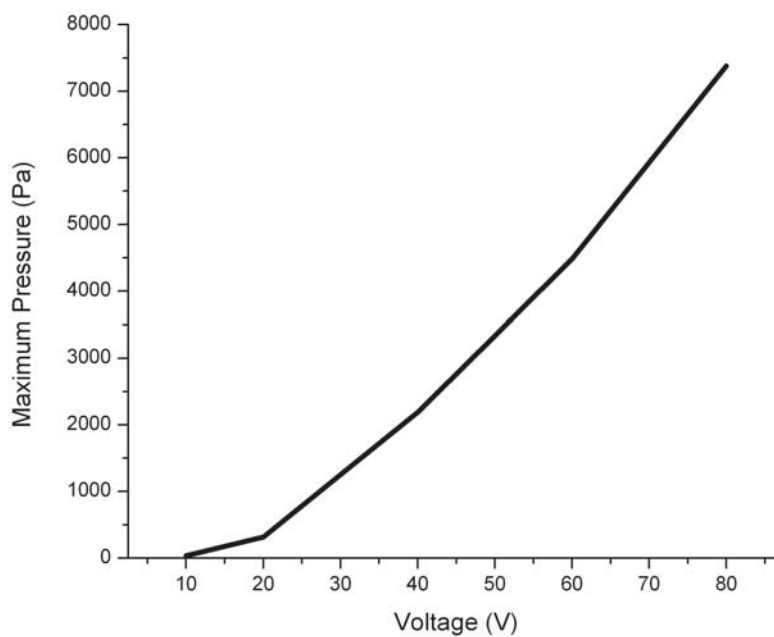


Figure 2.14: Experimental maximum pressure vs. applied voltage for the EOP based on mesoporous silica membrane.

Figure 2.15 shows the plot of EOP pressure test against the applied voltage for macroporous silicon membranes earlier demonstrated by Zheng et al.

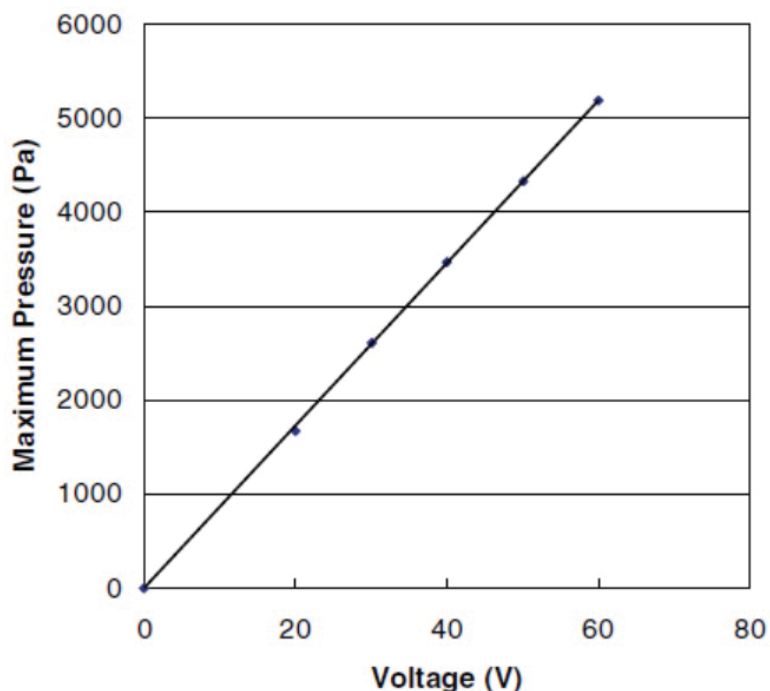


Figure 2.15: Experimental maximum pressure vs. applied voltage for the EOP based on macroporous silicon membranes [11]. [Permission in Appendix].

From the theoretical model using Eq.(2.1), Eq.(2.3) and Eq.(2.5), the mesoporous silica membrane would generate pressures of about 2×10^7 Pa and flow rates of about $8 \mu\text{l}/\text{min}$ at 60 volts. The flow rate achieved experimentally ($9 \mu\text{l}/\text{min}$ at 60 volts) is closer to the theoretical value ($8 \mu\text{l}/\text{min}$ at 60 volts), but the pressure value is contradicting. Various factors including resistance of the fluid in the EOP setup, resistance offered by the capillary tube, air trapped in the pump reservoirs and pore profile of the porous media caused a deviation from the expected linear behavior of the flow-rate measurements. Similar trend

for flow rate against applied voltage was observed by Zheng et al., for macroporous silicon [11].

For mesoporous silica membranes, at such small dimensions, the side walls of the pore cannot be considered to be smooth and the ridges present on the pore wall offers resistance to the flow. Frictional forces which depend on the channel aspect ratio and Knudsen number become significant at nano-scale dimensions. The presence of the EDL offers additional resistance to the flow. With the high resistance offered due to various factors, the time taken for the liquid around the electrode to be eventually pumped and be replaced by fresh water is probably high enough and this leads to electrolysis in the pump reservoir in which the electrodes are placed. With bubble formation, there is a high probability for the air bubble to block some of the pores and affect the performance of the pump. During the testing, reverse fluid flow was also observed. Electrolysis at the cathode at high bias could contribute to the reverse fluid flow and pressure generation. A combination of all the above mentioned factors could have contributed to a flow rate profile that deviated from a linear pattern for an applied voltage. A detailed theoretical review of the flow pattern in the flow regime ($0.001 < Kn \ll 0.1$) is presented in literature [47].

2.4.2 Pressure vs. Pore Size

Figure 2.16 shows a theoretical pressure value for different pore sizes obtained using Eq.(2.3). As the pore size of the porous media becomes smaller, the pressure increases to a larger value. This pressure increase is attributed to the increase of constriction for the flow of solvent across the porous media as the pore size becomes smaller which is in agreement with the Eq.(2.3).

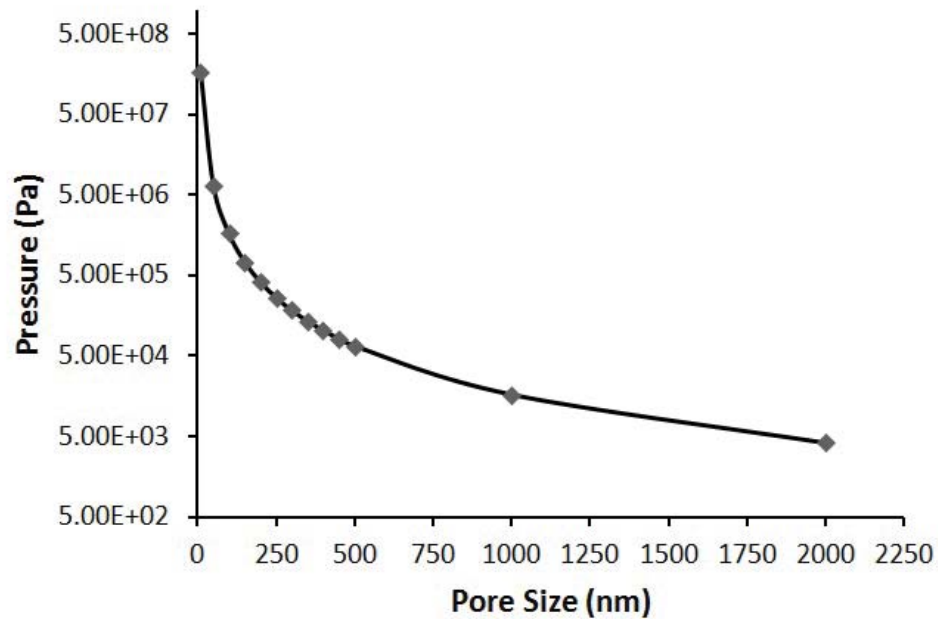


Figure 2.16: Theoretical maximum pressure generated vs. pore size of the porous silicon membrane.

2.4.3 Power Considerations For the EOP

The equations, Eq.(2.6) and Eq.(2.7) are utilized for estimating current and power required for EOP operation. Important parameters necessary for this estimation include, pore radius of the porous media, dimensions of the porous media, and properties of the working fluid. The configuration of EOP can be considered to be an equivalent of three resistors as shown in Fig. 2.17 consisting of, the reservoir in the left, the resistance offered by the porous silicon sample, and the reservoir on the right. The following values of the are considered that are listed in Table 2.6

Table 2.6
Parameters for current (I) and power calculations for EOP

Parameter	Value
Resistivity of DI water	17 MΩcm
Length of the pore	500 μm
Pore density of the porous media	$5.4 \times 10^6/\text{cm}^2$
Resistance of individual of the individual pore	R_{pore}
Resistance of the reservoir with DI water both left and right	$R_{left} = R_{right}$
Diameter of the Pt electrode	1 cm
Effective resistance of the pores in the porous region (resistance in parallel)	R_{eff}
Total system resistance	R_{system}
Diameter of the porous region	3.5 mm
Pore density in the porous region in the 3.5mm circular region	51×10^4

$$R = \frac{\rho L}{A} \quad (2.6)$$

$$R_{system} = R_{left} + R_{eff} + R_{right} \quad (2.7)$$

Using Eq.(2.6) and the parameters listed above, R_{pore} calculated is $836 \times 10^{10} \Omega$ and R_{eff} is 16.3 M Ω . Using Eq.(2.6), the resistance of the DI water in the left reservoir is calculated to be 21 M Ω . Total resistance of the system is calculated using Eq.(2.7) and is equal to 58.3 M Ω . The current (I) of the EOP system for 60 V is 1.02×10^{-6} A. The power consumption is 61.74×10^{-6} watts.

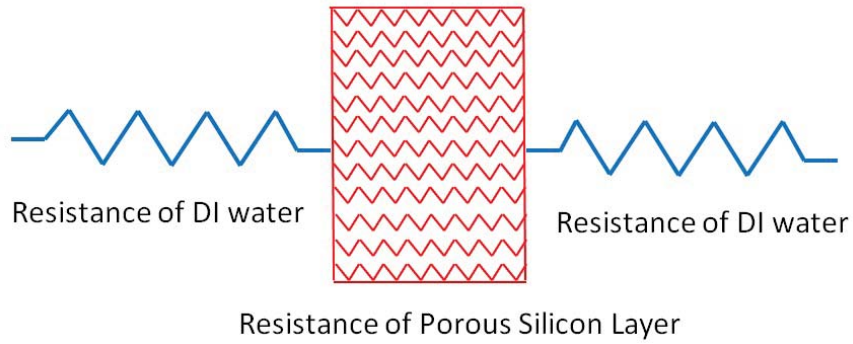


Figure 2.17: Equivalent resistance of DI water and porous silicon sample in the EOP configuration.

2.5 Fluid Permeability Test

In order to address and understand the issues related to the low flow rate observed for the EOP using mesoporous silica membrane, a permeability test for the porous membrane is performed. A syringe pump as shown in Fig. 2.18 is set to a flow rate of 0.21 ml/min and

is connected to the inlet of the pump reservoir in order pump the fluid through the porous membrane by pressure. A dead end pressure sensor was connected in parallel to the syringe pump inlet. Both macroporous silicon ($\sim 3 \mu\text{m}$) and mesoporous silicon membrane ($\sim 20 \text{ nm}$) are used as the pump media.

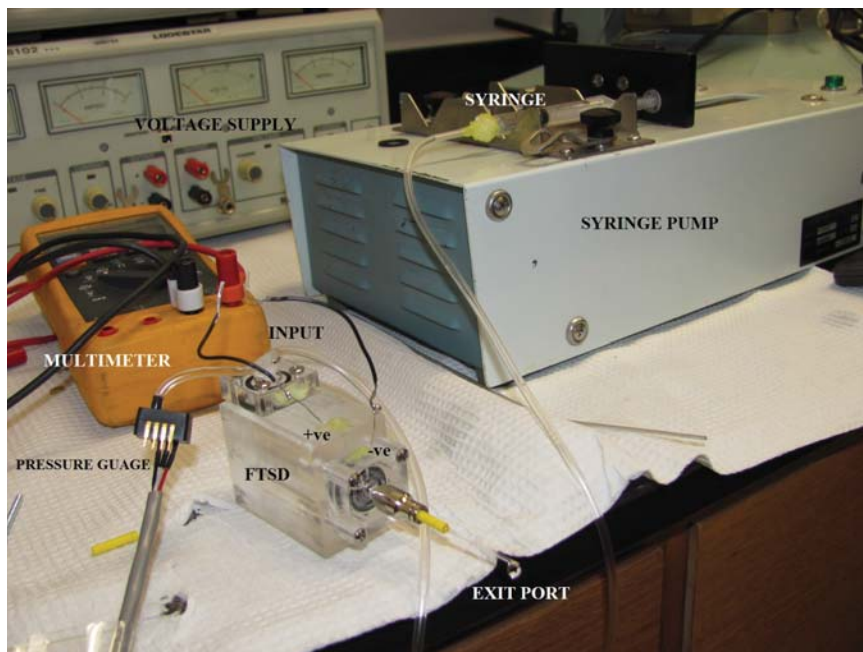


Figure 2.18: Fluid permeability setup used to check the fluid flow across the porous membrane in the EOP.

In the case of macroporous silicon, the pressure reached a constant value of 2700 Pa. In case of the mesoporous silicon sample, the pressure reached to the maximum limit of the sensor reading $\sim 34000 \text{ Pa}$ with a minimal flow rate at this pressure. Very low flow rates at such high pressures from the syringe pump test implies that the external voltages applied in the case of EOP test needs to generate equal or higher forces on the fluid molecules for them to overcome the capillary resistance and flow through the pores.

2.5.1 Stress in the Mesoporous Silica Membrane

Thermal oxidation of macroporous membrane gives significant strength to the porous membrane due to the oxide formation on the side walls of the pores. On contrary, the mesoporous silica membranes become very brittle due to high compressive stress and this makes loading/testing challenging.

Earlier work on various mesoporous silicon substrates show that these membranes have Young's Modulus values of 10 - 20 GPa [48]. These values are much lower than the bulk silicon with a Young's Modulus value of 160 GPa. To implement these membranes for the EOP testing, it is important to have a porous membrane that can withstand the testing process. Selectively porosifying the bulk silicon using a skeleton mask can improve the strength of the porous membrane. In this process, a mask pattern is formed on the silicon substrate using photolithography. With this mask, selective regions of $200\mu\text{ m}$ by $200\mu\text{ m}$ squares are formed using sputter deposited Cr/Au films and lift-off technique. Results from the selective etching using the mask are shown in Fig. 2.19.

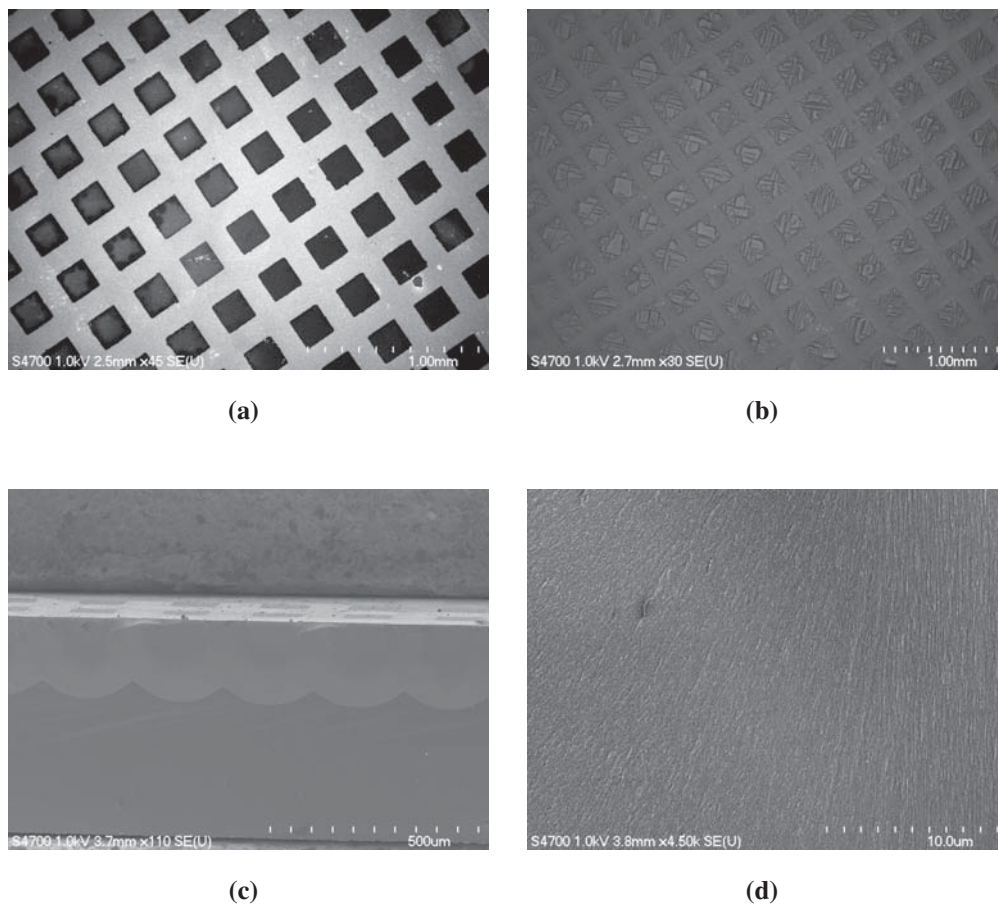


Figure 2.19: EOP mask pattern formed by selective porosifying of silicon, (a) the mask pattern, (b) porosified region, (c) cross-sectional image of the sample at low magnification, and (d) EOP mask cross-section at high magnification.

2.6 Summary

Through wafer macroporous silicon and mesoporous silica membranes are implemented for EOP application. Macroporous silicon is utilized as pump media to reproduce results of a large flow rate of $11.9 \mu\text{l min}^{-1} \text{mm}^{-2}$ and a maximum pressure of 5.2 kPa at 60

volts earlier demonstrated by Zheng et al. Mesoporous silica membranes are implemented as a porous media for EOP application for the first time to our knowledge. Flow rate and maximum pressure measurements of mesoporous silica membranes indicate that the smaller pore diameter improves maximum pressure response and impacts maximum flow rate based on morphology, yielding flow efficiencies of $2.8 \mu\text{l}/\text{min}/\text{V}/\text{cm}^2$ and pressures of 92 Pa/V. Initial pressure capacity measurements indicate that mesoporous silica samples can generate really high pressure values in accordance with theoretical pressure calculations of 2×10^7 Pa for a 10 nm pore size. Selective porousifying improved the strength of the mesoporous membrane and withstood many testing cycles. Permeability of the mesoporous silicon membrane is tested with the working fluid using a syringe pump test setup.

Chapter 3

Optical Properties of Mesoporous Silicon/Silica

3.1 Introduction

From the earlier chapters, it is evident that translucent mesoporous silica membranes with high surface area is a potential material for optical dye immobilization and can be implemented in the flow-through sensing device for pH measurements¹. In order to successfully implement mesoporous silica for flow-through detection, it is important to understand its optical properties as fluorescence measurements are performed on this

¹Parts of this chapter were previous published in the journal, Porous Semiconductors - Science and Technology, permission in appendix

material with immobilized dyes. Understanding how light couples into the mesoporous media will help in accounting for any losses involved both in transmission and reflection mode. Knowledge of optical constants, the refractive index and extinction coefficients will aid in improving the design and implementation of the device.

Figure 3.1 shows the typical transmission spectra of a 100 μm thick silicon sample. As can be seen, silicon becomes transparent in the IR region and it will be interesting to study the same for mesoporous silica membranes that are fabricated from silicon.

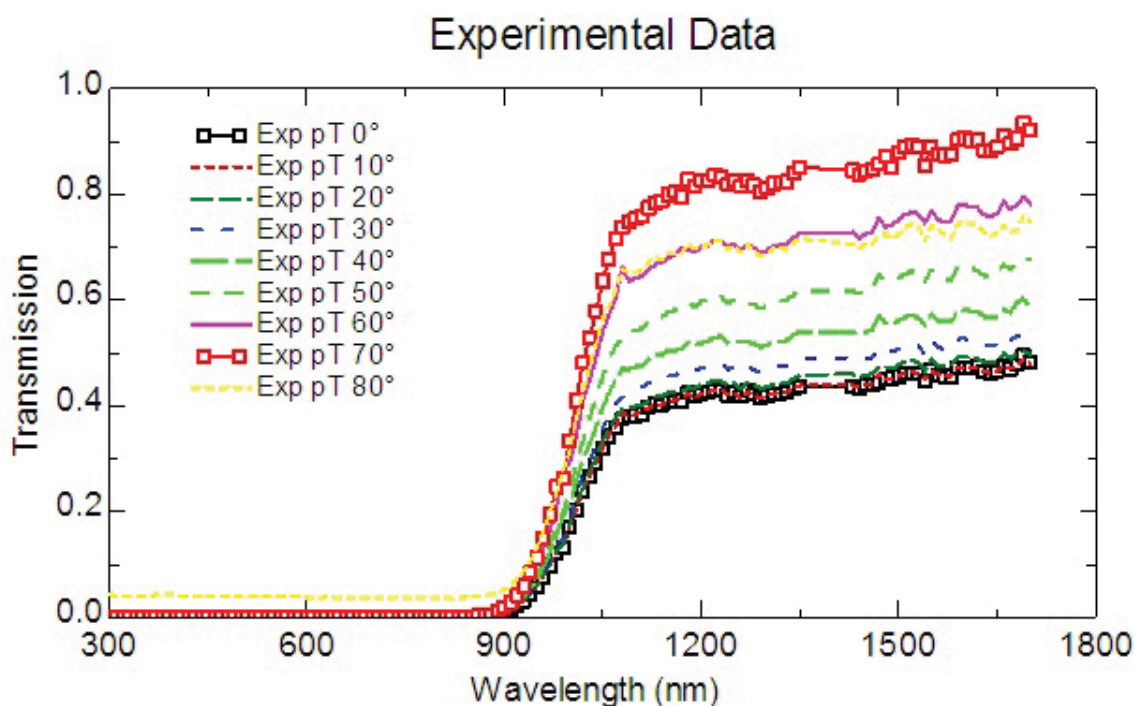


Figure 3.1: Silicon transmission from 200 nm to 1000 nm in a 100 μm thick silicon substrate.

The large specific surface area of porous silicon and the ability to tailor the pore size and morphology leads to sensing applications that utilize changes in its electrical,

chemical, and optical properties during sensing while interacting with gases and other fluids under study. Structural features of porous silicon layers such as pore size, porosity (p), and thickness (t) dictate how light interacts and gets modulated while passing through the porous region and are key parameters in optical and photonic systems. In the past, investigators have broadly explored the modulation of the bandgap and refractive index of porous silicon layers to produce devices such as Bragg reflectors [49], rugate filters, and other photonic bandgap structures enabling chemical, biochemical, thermal and other novel sensors and detectors [50]. Rugate filters can be fabricated from porous silicon substrates by gradually varying the porosity of the porous silicon by the modulation of applied current density [51]. While reflective sensing has been effectively leveraged, some sensing applications would be enabled with the potential for a flow through detection system. Thin films of porous silica that are formed from the thermal oxidation of porous silicon can be attractive for their use as cladding material of low refractive index for optical communications [52].

There is a limited literature available reporting the transmission behavior of macroporous silicon samples in the visible range [53]. Hutchinson et al., have performed a theoretical and numerical study on transmission and reflection of highly ordered mesoporous thin films [54]. They investigated the effect of pore size and porosity on these optical parameters using a simulation study on mesoporous 2D and 3D structures. Applications for antireflection coatings using porous silicon/silica films are appealing since the refractive index can be modulated from $n_{air} = 1$ to $n_{Si} = 3.5$ depending upon the

porosity and the sidewall oxide thickness [55]. With porous silicon, the relative refractive index can be tailored by the degree of thermal oxidation [56].

3.2 Experimental Methods

Experimental conditions for the fabrication of mesoporous silicon and mesoporous silica utilized for optical characterization in this chapter are listed in Chapter 2. In this work, Sample A and Sample B denote mesoporous silica samples (550 μm thick) anodized at 10 mA/cm^2 and 20 mA/cm^2 . Sample C denotes mesoporous silicon sample (600 nm thick porous layer) obtained after anodizing at 10 mA/cm^2 . All three samples were anodized in electrolyte consisting of 10^{-3}M CTAC, HF(49%), ethanol, and DI water at a volume ratio of 1:1:1 [35]. Optical transmission and reflection measurements utilized mesoporous silica membranes of thickness 550 μm . Refractive index measurements were performed using 600 nm and 1 μm thick un-oxidized and oxidized Sample C. Optical measurements were conducted using the J.A. Woollam V-VASE 32 Ellipsometer.

The impact of thermal oxidation on the morphology and oxide growth rate of porous silicon was earlier reviewed by Pirasteh et al. [57]. In their work, pore morphology before and after thermal oxidation was characterized and analyzed using scanning electron microscopy (SEM) and transmission electron microscopy (TEM) techniques. Thermal oxidation rates of porous silicon samples were evaluated using micro-Raman spectroscopy.

In order to confirm that the mesoporous silica sample shown in Fig. 2.6 in Chapter 2 is fully oxidized, an x-ray scan was performed on the sample. Figure 3.2 shows the diffraction spectra of amorphous quartz superimposed over the spectra of mesoporous silica indicating that the sample is amorphous and is silica. The absence of any notable peak at 69 deg (2θ angle) corresponding to silicon (004) plane confirms that the mesoporous silica membrane is fully oxidized.

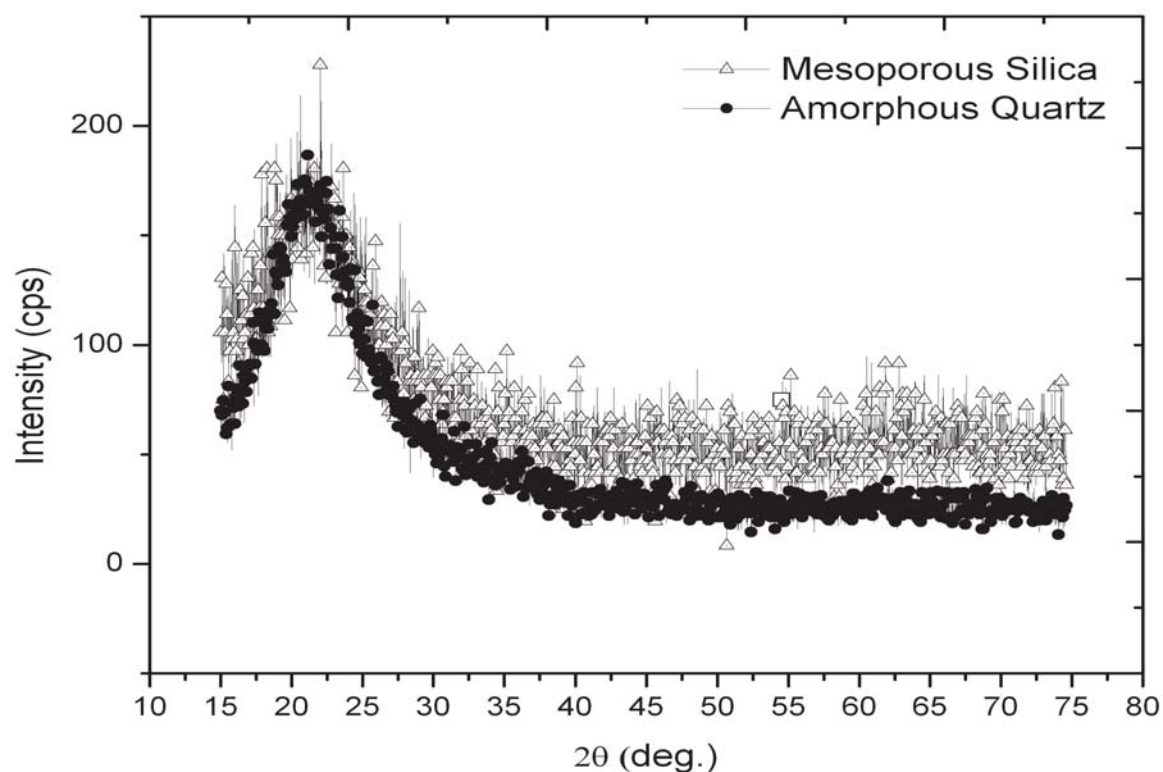


Figure 3.2: X-ray diffraction spectra of amorphous quartz substrate superimposed over the spectra of mesoporous silica.

3.3 Optical Measurements of Mesoporous Silica

Ellipsometry is a very effective and sensitive measurement technique that utilizes polarized light to extract optical and material properties of the sample under study. Ellipsometry is highly sensitive due to the fact that it utilizes the relative change in the phase of the reflected light compared to many other techniques that use the change in intensity of the reflected light. In addition, because ellipsometric measurements do not require measurement of the absolute intensity of the reflected light, no reference sample is required. Ellipsometry measures the change in polarization state of light reflected (or transmitted through) the surface of a sample. Extraction of the optical constants $n(\lambda)$ and $k(\lambda)$ for the fabricated mesoporous silica membrane is complicated as the thickness of the membrane used is in the order of $500\text{ }\mu\text{m}$. As the thickness of the film increases to several microns, the number of data oscillations becomes increasingly larger and becomes difficult to resolve at shorter wavelengths. The standard film thickness for spectroscopic ellipsometric measurements is less than $5\text{ }\mu\text{m}$ for visible to near infrared wavelengths. Increase in film thickness introduces surface non-uniformities and also the presence of any voids in the membrane or thin film impedes the process of determining the exact values. In order to extract the optical constants n and k , first ellipsometric parameters ψ and Δ are measured. Ellipsometry measures the ratio of the ψ and Δ and since the ratio is a complex number, it contains the phase information of the optical signal. Ellipsometry is used to measure parameters both for thin films and bulk materials including optical constants, thin film thickness,

doping concentration, surface and interfacial roughness, alloy ratio, crystallinity, optical anisotropy, and porosity [58].

3.3.1 Transmission Spectra

Optical transmission measurements were performed on $550\mu\text{m}$ thick mesoporous silica samples Sample A and Sample B.

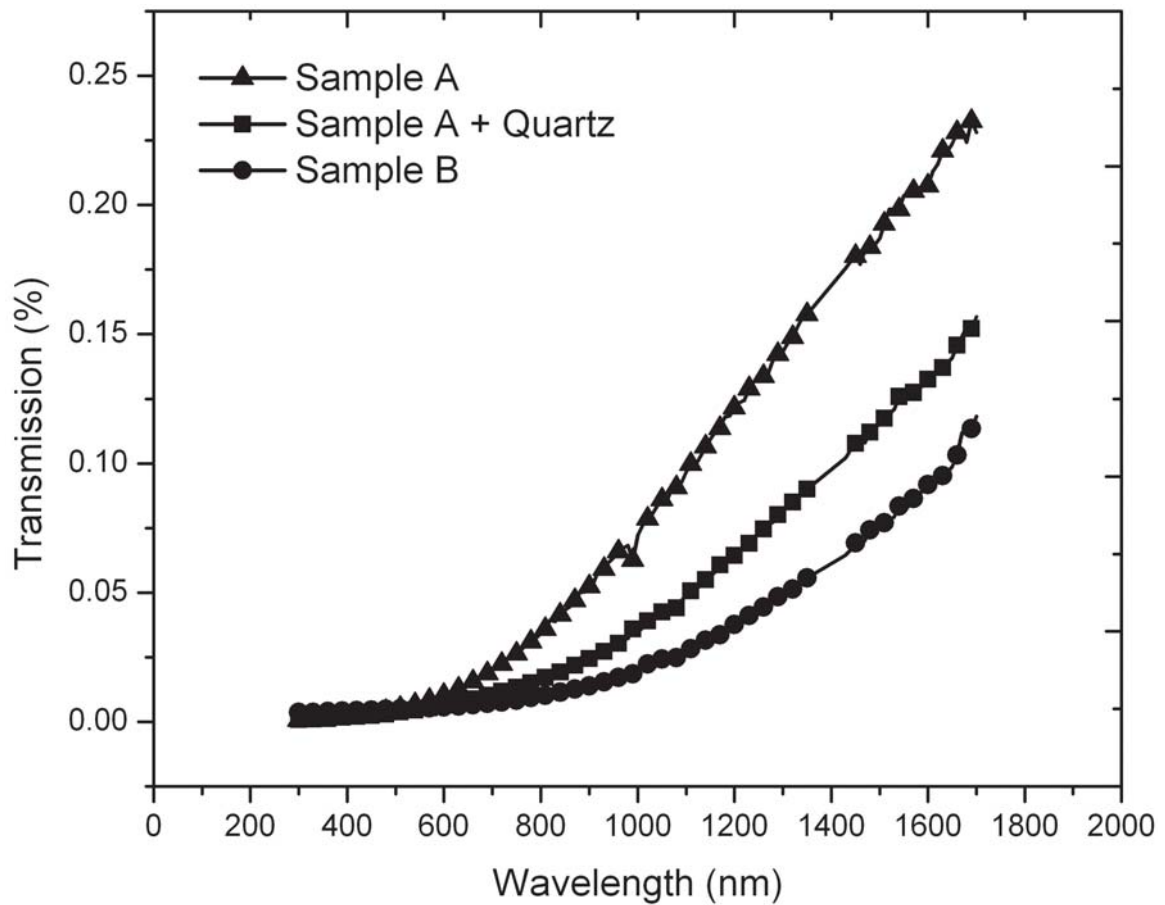


Figure 3.3: Transmission spectra for a typical mesoporous silica Sample A and Sample B with and without quartz substrate as a supporting base.

A quartz substrate was used as supporting base for the mesoporous silica samples during the optical measurements. Figure 3.3 shows the transmission spectra for Sample A and Sample B. From the initial optical characterization measurements, it was found that transmission for quartz approaches 90% at infrared wavelengths. As seen in the Fig. 3.3, there is attenuation of transmitted signal when the sample is mounted on the quartz substrate. This attenuation of intensity could be attributed to the air gap that lies between the sample and quartz substrate. Without the quartz substrate, Sample A has a transmission intensity of ~ 0.25 and Sample B has a transmission intensity of ~ 0.12 at 1700 nm. For a transparent media, the absorption coefficient of the material is related to incident and transmitted intensity by the Beer-Lambert's law given by the relation in Eq.(3.1),

$$I = I_0 e^{-\alpha(\lambda)t} \quad (3.1)$$

where I and I_0 are the incident and transmitted intensities, $\alpha(\lambda)$ is the absorption coefficient; and t is the thickness of the absorption media. The optical properties of mesoporous silica can be tuned or modulated by varying the pore size, pore volume, pore morphology and the thickness of oxide on the pore walls by the electrochemical anodization. Anodization at higher current density (Sample B) results in larger pore sizes with a thicker silicon sidewall compared to Sample A which was anodized at a lower current density. The optical properties of the mesoporous silicon and mesoporous silica samples are determined by the volume ratio of silicon, SiO_2 , and the air volume present in the pore. After thermal oxidation, Sample B has a thicker oxide layer on the pore walls compared

to Sample A. Also, it is proposed that there are more transmission losses for Sample B at the pore boundaries compared to Sample A which has a more continuous oxide layer with much smaller pores. The cumulative impact of these two effects resulted in a decrease in transmission for sample B compared to Sample A as seen in Fig. 3.3.

3.3.2 Angle Resolved Transmission Spectra

Figure 3.4 shows the ellipsometric configurations for the angular transmission and reflection measurements. Angle resolved transmission as well as angle resolved reflection measurements were performed on the 550 μm mesoporous silica Sample A. These measurements indicate the transmission as well as reflection losses as the incident light passes through or reflected at different angles from the sample. For the transmission measurements, Sample A was rotated on axis with respect to the incident beam and the detector was rotated from 0° to 45° in increments of 5° . For the reflection measurements, the detector unit is positioned in front of sample A as it is rotated by an angle.

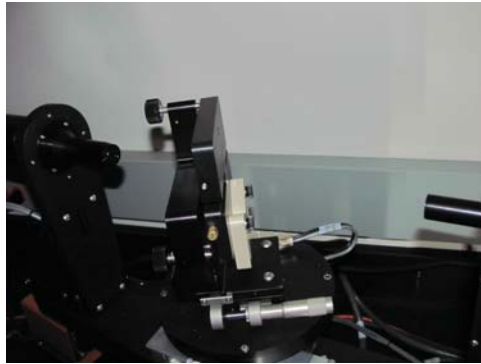
From the transmission spectra in Fig. 3.5, it can be seen that the transmission is maximum at normal incidence and minimum for 45° . This is because of the path length through the silica material that the incident light beam travels is at the minimum for the 0° incidence and the greatest for 45° in the measurement range. Optical transmission measurements in the range of 0.3 - 0.8 μm on macroporous silicon with through pores



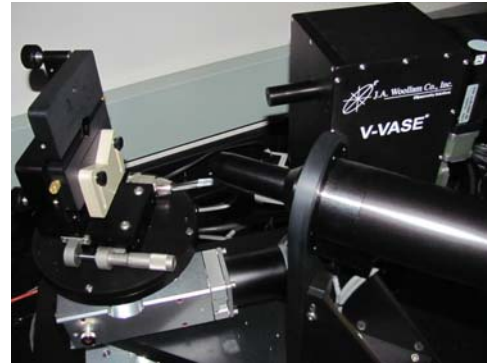
(a)



(b)



(c)



(d)

Figure 3.4: Ellipsometric configurations for angular transmission measurements, (a) normal Incidence, (b) $+30^\circ$, (c) -30° , and (d) reflection measurements at 20° .

of $200\ \mu\text{m}$ depth has been reported by Astrova et al. [53]. Figure 3.6 shows the angular dependence of the transmission of Sample A for 900 nm, 1200 nm, and 1500 nm wavelengths.

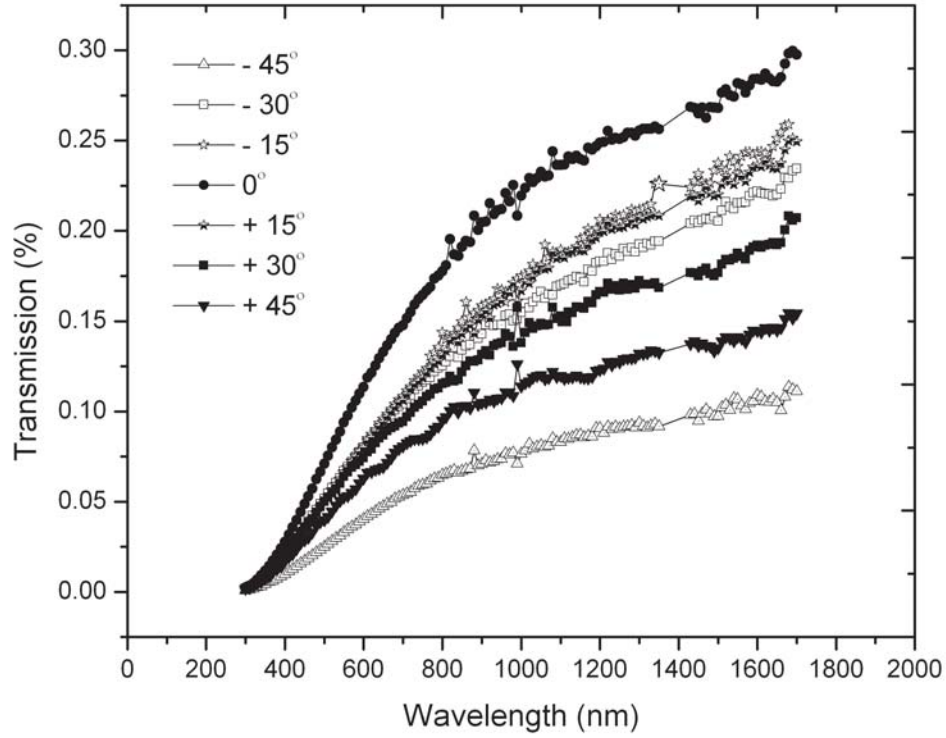


Figure 3.5: Angle resolved transmission spectra measurements from -45° to $+45^\circ$ for Sample A.

3.3.3 Angle Resolved Reflection Spectra

For a macroporous silicon substrate, the normal incident light propagates along the $\langle 100 \rangle$ direction, the light is transmitted through the pore cavity with refractive index $n \sim 1$ with SiO_2 and silicon as the absorbent media surrounding the cavity [53]. In the case of mesoporous silica, the light propagates through a medium of SiO_2 and air. The reflectance of the porous silicon membrane can be controlled by modifying the pore morphology or by

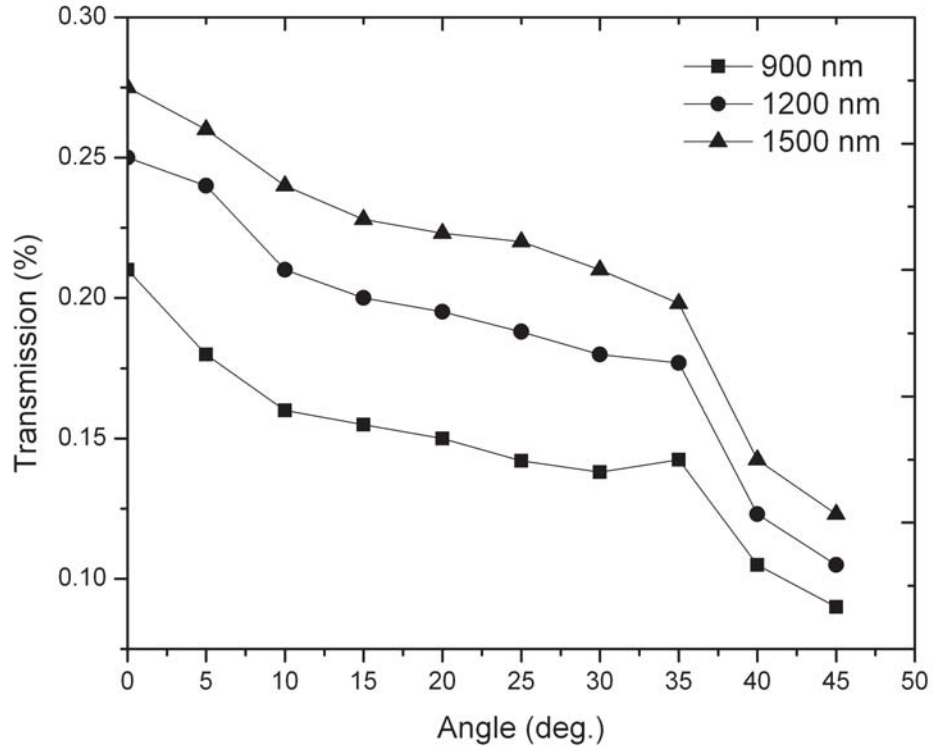


Figure 3.6: Variation of transmitted intensity vs. angle of incidence for for Sample A at 900 nm, 1200 nm, and 1500 nm.

filling the porous structure with other materials [57]. From Fig. 3.7, it can be seen that the reflectance decreases as the angle changes from 20° to 70° . The reflected intensity values are very low in magnitude as most of the incident light is transmitted. Figure 3.8 shows the angular dependence of the reflected intensity of Sample A for 900 nm, 1200 nm and 1500 nm wavelengths.

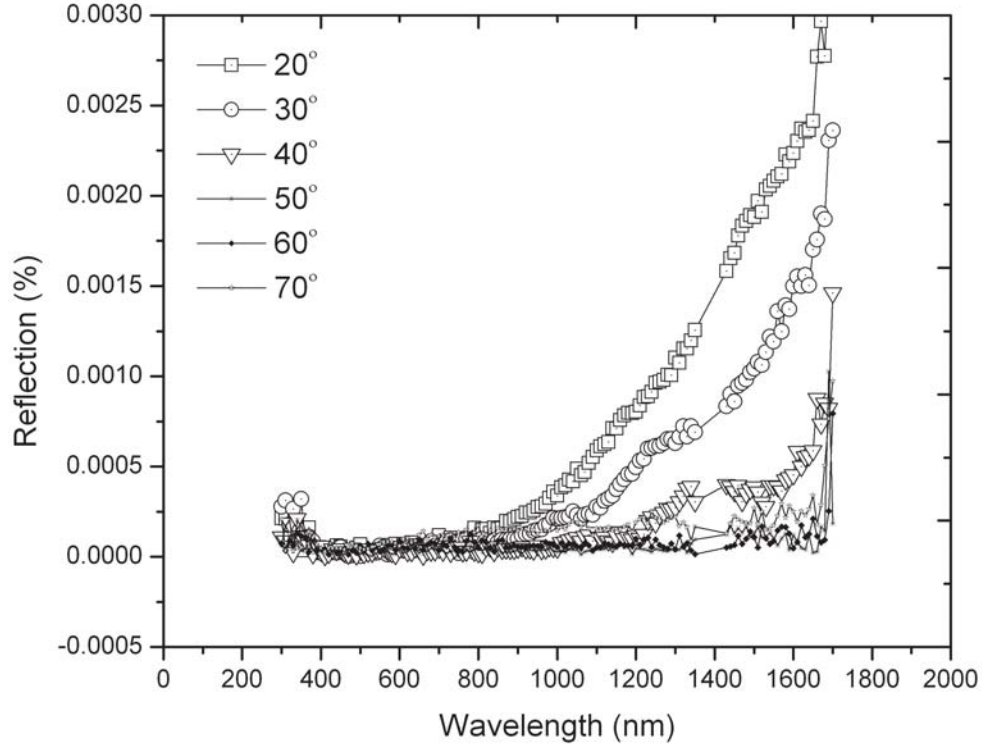


Figure 3.7: Angle resolved reflection spectra measurements from 20° to 70° for Sample A.

3.3.4 Optical Constants

The refractive index n and extinction coefficient k are important parameters for materials used for optical communications, filters and gratings. The complex refractive index is related to the extinction coefficient by the relation given in Eq.(3.2),

$$\tilde{n} = n + ik \quad (3.2)$$

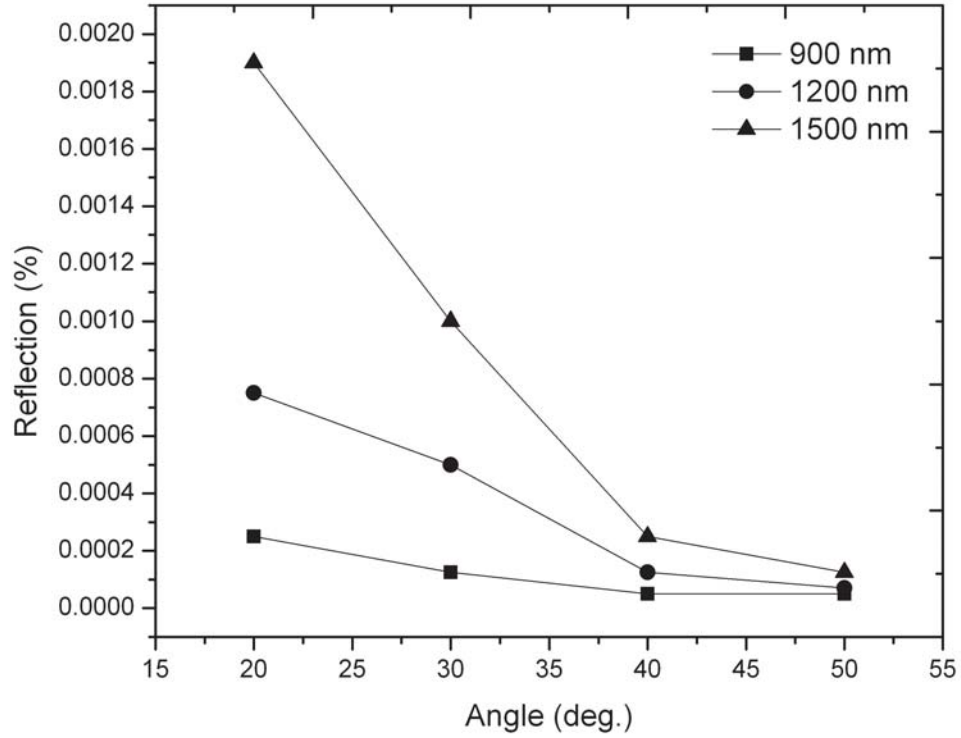


Figure 3.8: Variation of reflected intensity vs. angle of incidence for Sample A at 900 nm, 1200 nm, and 1500 nm.

Where \tilde{n} is the complex refractive index, n is the refractive index of the material, and k is the extinction coefficient, which are both obtained from the spectroscopic ellipsometric parameters ψ and Δ . Of the many models available, the Bruggemann model which uses effective medium approximation (EMA) is considered ideal for porous materials when the wavelength of the incident light is much greater than the dimensions of the pores [59], [55].

As it was difficult to perform ellipsometric measurements on $550 \mu\text{m}$ thick samples

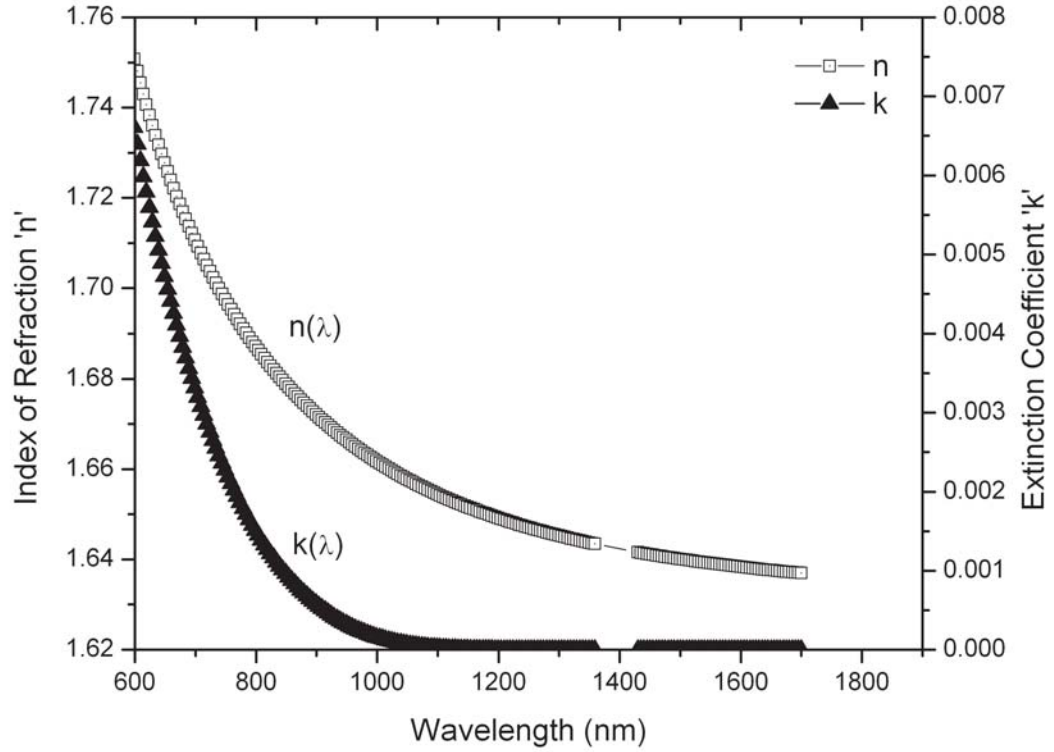


Figure 3.9: The measured refractive index (n) and extinction coefficient (k) of the mesoporous silicon Sample C (un-oxidized sample).

to extract the refractive index values, oxidized and un-oxidized mesoporous silicon Sample C were utilized and measurements were conducted at 70° angle. Figure 3.9 and Fig. 3.10 show measurements for n and k for un-oxidized and oxidized Sample C. The porosity and refractive index for porous silicon layer are related by the relationship given in Eq.(3.3),

$$p_{PS} = 1 - \frac{(1 - n_{PS}^2)(n_{Si}^2 + 2n_{PS}^2)}{3n_{PS}^2(1 - n_{Si}^2)} \quad (3.3)$$

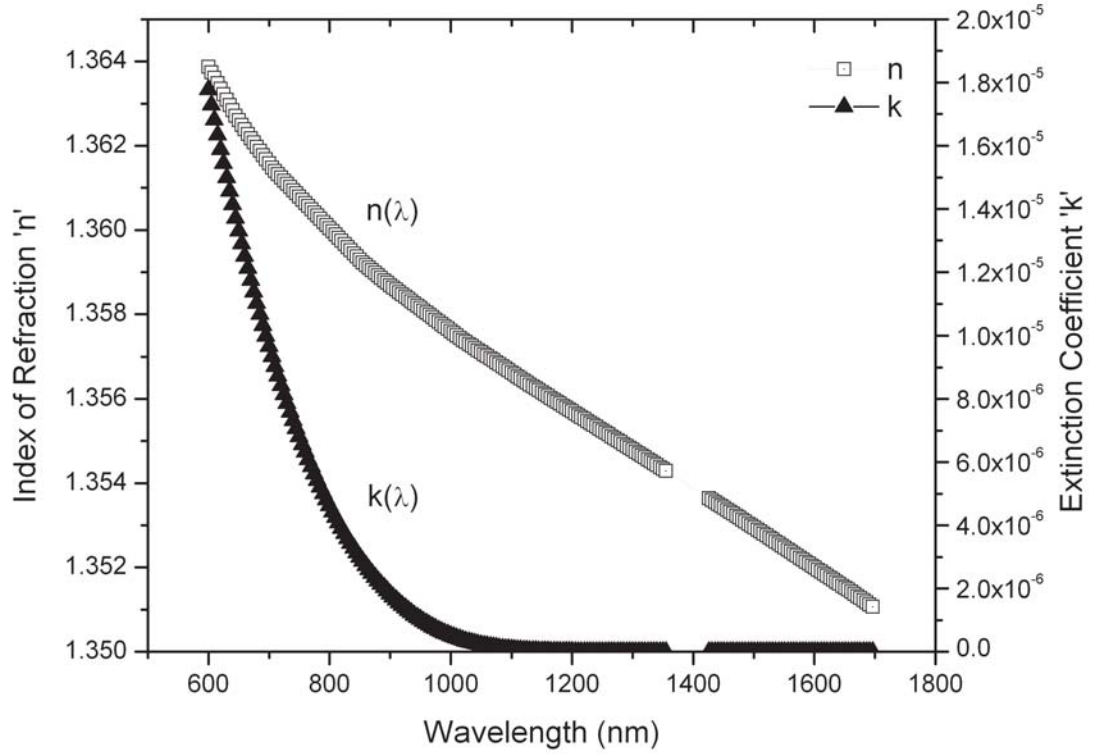


Figure 3.10: The measured refractive index (n) and extinction coefficient (k) of the mesoporous silica film (oxidized sample).

where p_{PS} is the porosity, n_{PS} and n_{Si} are the refractive index of porous silicon and crystalline silicon at a specific wavelength of light [55]. The experimental value of porosity for mesoporous silicon that was earlier reported for similar conditions is about 60% [60]. Using the Eq.(3.3) and the measured values of refractive index of mesoporous silicon Sample C of 1.66 and crystalline silicon of 3.5 at 1000 nm, the computed value of porosity of the sample C is $\sim 67\%$, which is in good agreement with past results [60]. The porosity values for mesoporous silicon and mesoporous silica are estimated based on high resolution FE-SEM top view imaging of the samples through image processing

analysis using Image J software and assuming a columnar porosity as indicated by the cross sectional FESEM imagery of Fig. 2.5 from Chapter 2. Total pore area versus total sample area was utilized to provide an estimate of porosity. For the mesoporous silicon Sample C, a porosity value of 57.6% was obtained while adjusting the threshold by 10% in the Image J software. This value of porosity is comparable to the value obtained using the Bruggemann model. The porosity of mesoporous silica film is estimated using the following expression in Eq.(3.4) [61],

$$p_{OPS} = 1 - 2.27 \frac{t_{PS}}{t_{OPS}} (1 - p_{PS}) \quad (3.4)$$

In the above equation, t_{PS} and t_{OPS} are the mesoporous silicon and mesoporous silica film thicknesses obtained through SEM imaging. Parameter p_{PS} is the porosity value of mesoporous silicon obtained from the SEM and Image J analysis. For the oxidized mesoporous silica Sample C, a porosity value p_{OPS} of 24% was obtained using Eq.(3.4), which is comparable from the model fit value of 27% using Eq.(3.3) which utilized the measured refractive index values. The modeled thickness of the mesoporous silicon film is about 600 nm with Mean Squared Error (MSE) of 53, and for mesoporous silica it is about 1200 nm with an MSE of 48, which agrees with the experimental values. Oxidized Sample C has a refractive index value lower than un-oxidized Sample C as can be seen by comparing Fig. 3.9 and Fig. 3.10.

The modeling for n and k was done from 600 nm - 1700 nm to obtain the best fit.

Refractive index values for dense silica as reported is about 1.46 [62]. A very detailed study of porosity measurements on oxidized porous silicon samples is reported by Charrier et al. [61], [63]. The decrease in refractive index of un-oxidized mesoporous silicon from 1.66 in the IR region to 1.36 for mesoporous silica is shown in the plots in Fig. 3.9 and Fig. 3.10 confirming the presence of fully oxidized silica membranes. From Eq.(3.1), and the measured experimental data, the absorption coefficient for the 550 μm mesoporous membrane anodized at 10 mA/cm² is calculated to be 31.8 cm⁻¹. Using Beer's law as in Eq.(3.5),

$$\alpha = \frac{4\pi}{\lambda}k \quad (3.5)$$

The extinction coefficient k is calculated for the 550 μm thick material to be 2.5×10^{-4} at 1000 nm. From Fig. 3.10, the measured extinction coefficient for a 1 μm mesoporous silica film is 7.5×10^{-7} . While both values indicate a weakly absorbing material, the extinction coefficient of a 1 μm mesoporous silica film is much lower than that of the 550 μm mesoporous silica sample. A direct comparison between the bulk and the thin film cannot be drawn at this time, rather these differences serve to highlight the differences in the optical properties of the bulk vs. thin film behavior of the material.

3.4 Summary

Optical characterization on mesoporous silica membranes was performed using ellipsometry from 300 - 1000 nm. From the transmission measurements on mesoporous silica, it is observed that there is a decrease in absorption loss for the oxidized mesoporous silica sample A (anodized at lower current density with smaller pore diameter) compared to mesoporous silica sample B (anodized at higher current density with a larger pore diameter). X-ray diffraction measurement on mesoporous silica samples confirms the presence of fully oxidized membranes. Angular transmission as well as angular reflection decreases with decrease in incident angle. The refractive index (n) values for oxidized and un-oxidized mesoporous silicon Sample C at 1000 nm are 1.36 and 1.66. The decrement in refractive index implies that the mesoporous silicon has been oxidized into mesoporous silica, given that the refractive index of bulk silicon is ~ 3.5 and bulk silica is ~ 1.4 . The extinction coefficient (k) for a thick ($550\text{ }\mu\text{m}$) mesoporous silica samples is 2.5×10^{-4} and for a thin ($1\text{ }\mu\text{m}$) mesoporous silica is 7.5×10^{-7} . The porosity decreased with thermal oxidation of porous silicon and is confirmed by Bruggemann model as well as Image J analysis. The initial measurements of normal incidence optical transmission indicate promising results to use these mesoporous silica membranes for visible to the near infrared regime applications. Potential applications that could result from mesoporous silica material include flow through porous membrane for chemical and biological detections.

Chapter 4

Flow-Through Sensing Using Fluorescence Measurements

4.1 Introduction

This chapter presents some of the fluorescence studies done in collaboration with Ms. Qili Hu and Dr. Sarah Green from the Chemistry Department at MTU. Ms. Hu's major contribution includes developing the chemistry and fluorescence measurements².

Chapter 2 and Chapter 3 have demonstrated the significant components of the flow-through sensing device including material fabrication, characterization and testing.

²Parts of this chapter were previous published in the journal, IEEE-Nano, permission in appendix

The final task involves integrating the electro-osmotic pumping and fluorescence detection for a complete flow through sensing system that will be used for measuring the pH of different solvents.

Understanding the activity of hydrogen ions (pH) is one of the most important parameters for studying fresh studies. Optical pH sensing has many advantages over electrochemical techniques including high sensitivity, absence of reference signal, immunity to electrical interference, comparative ease of miniaturization, and potential for remote sensing [64].

Fluorescein is a pH dependent fluorescent dye and its pH-dependent excitation spectra allows for pH determination from ratiometric based measurement. In this study, fluorescein is covalently bonded to the internal surface of porous silica through surface reaction with self-assembled monolayer of trichlorosilanes [65] and fluorescence excitation spectra is considered for pH measurement in comparison to other above mentioned techniques.

4.2 pH Measuring Mechanism

A brief introduction to the theory involved in pH measurement using the fluorescence intensity spectra is presented here. Understanding the quality of waters require a

measurement of the concentration of hydrogen ion activity (H^+) or the pH (negative logarithm of hydrogen ion concentration). Spectrophotometric pH measurements involves the use of acid-base indicators that change their color depending on the pH of the solution they are in. For a weak acid indicator, the dissociation is given by Eq.(4.1) [66].



where HL^- is the acidic or protonated form, and L^{2-} is the basic or the un-protonated form.

The equilibrium expression K_a corresponding to the second dissociation is written as

$$K_a = \left(\frac{[H^+][L^{2-}]}{[HL^-]} \right) \left(\frac{\gamma_{H^+}\gamma_{L^{2-}}}{\gamma_{HL^-}} \right) \quad (4.2)$$

In the expression Eq.(4.2), K_a is the acidity constant (the acid ionization constant or the indicator equilibrium constant) in the reaction. γ 's are the individual or single ion activity coefficients. In the expression Eq.(4.2), the pH is given by Eq.(4.3),

$$pH = -\log ([H^+] \gamma_{H^+}) \quad (4.3)$$

The pH can also be written as Eq.(4.4),

$$pH = pK_a + \log \frac{[L^{2-}]}{[HL^-]} \quad (4.4)$$

Also, $[L^{2-}]$ and $[HL^-]$ are related to the intensity ratios $I[L^{2-}]$ and $I[HL^-]$ by Eq.(4.5),

$$\frac{[L^{2-}]}{[HL^-]} = \frac{I[L^{2-}]}{I[HL^-]} \quad (4.5)$$

where, $I[L^{2-}]$ and $I[HL^-]$ are the absorption or fluorescence intensity ratio of the species $[L^{2-}]$ and $[HL^-]$ from the experiment. The pH of the solution can be calculated using the above intensity ratios. Absorbance spectra corresponding to $I[L^{2-}]$ and $I[HL^-]$ forms of cresol red (sodium salt) is shown in Fig. 4.1 [66].

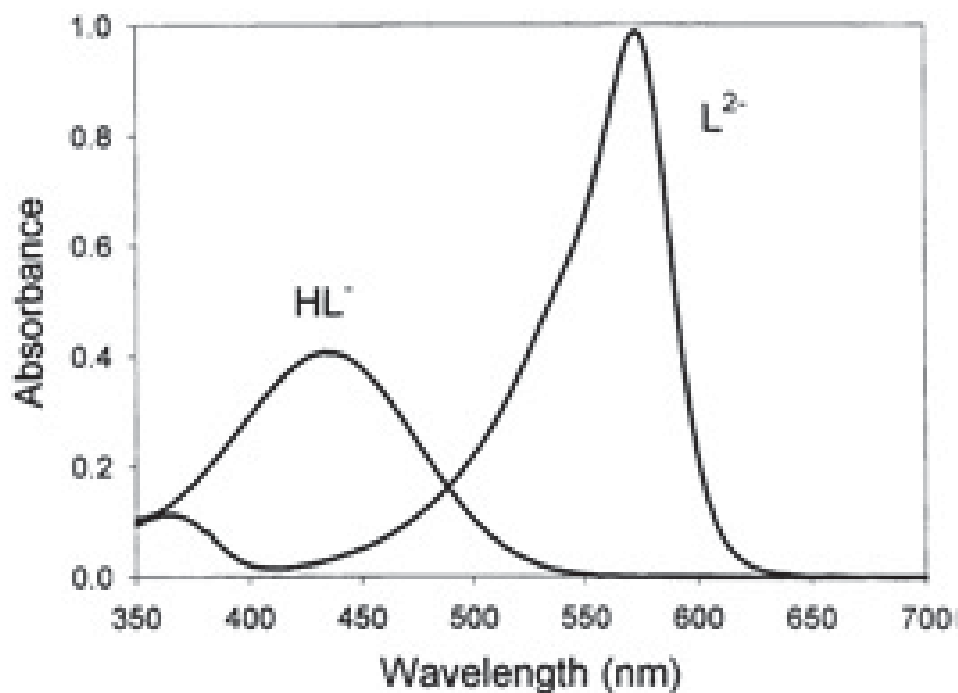


Figure 4.1: Absorbance spectra corresponding to $I[L^{2-}]$ and $I[HL^-]$ forms of cresol red (sodium salt). The ionic concentration of protonated HL^- form is 1.80×10^{-5} M (pH 4.5) and the ionic concentration of deprotonated L^{2-} is 1.53×10^{-5} M (pH 12). pH measurements are obtained from the absorbance spectra at 439 nm, 577 nm, and 724 nm [66]. [Permission in Appendix].

4.3 Flow-Through Sensing Device

A schematic of the meso-scale pump body that is fabricated using plexiglass for the flow-through sensing device (FTSD) configuration designed for pH measurements of fresh water using indicator dyes that are immobilized on porous silica templates is shown in Fig. 4.2. As shown in Fig. 4.3, there is an additional port on the FTSD to load the sample and refill the reservoir. The exterior walls of the fixture are mirror polished to reduce scattering during detection. The dye coated mesoporous silica sample is held on a slot machined on a thin slab of plexiglass. As described earlier, during the testing operation, the buffer solution interacts with the porous silica chip and leads to different fluorescence signals as the pH of the solution is changed. During the sensing phase, the incident light (excitation source) from the lamp of the fluorometer passes through the fixture walls and is incident on the dye coated porous silica membrane. The emitted fluorescent signal passes through the fixture walls and is directed towards the detector.

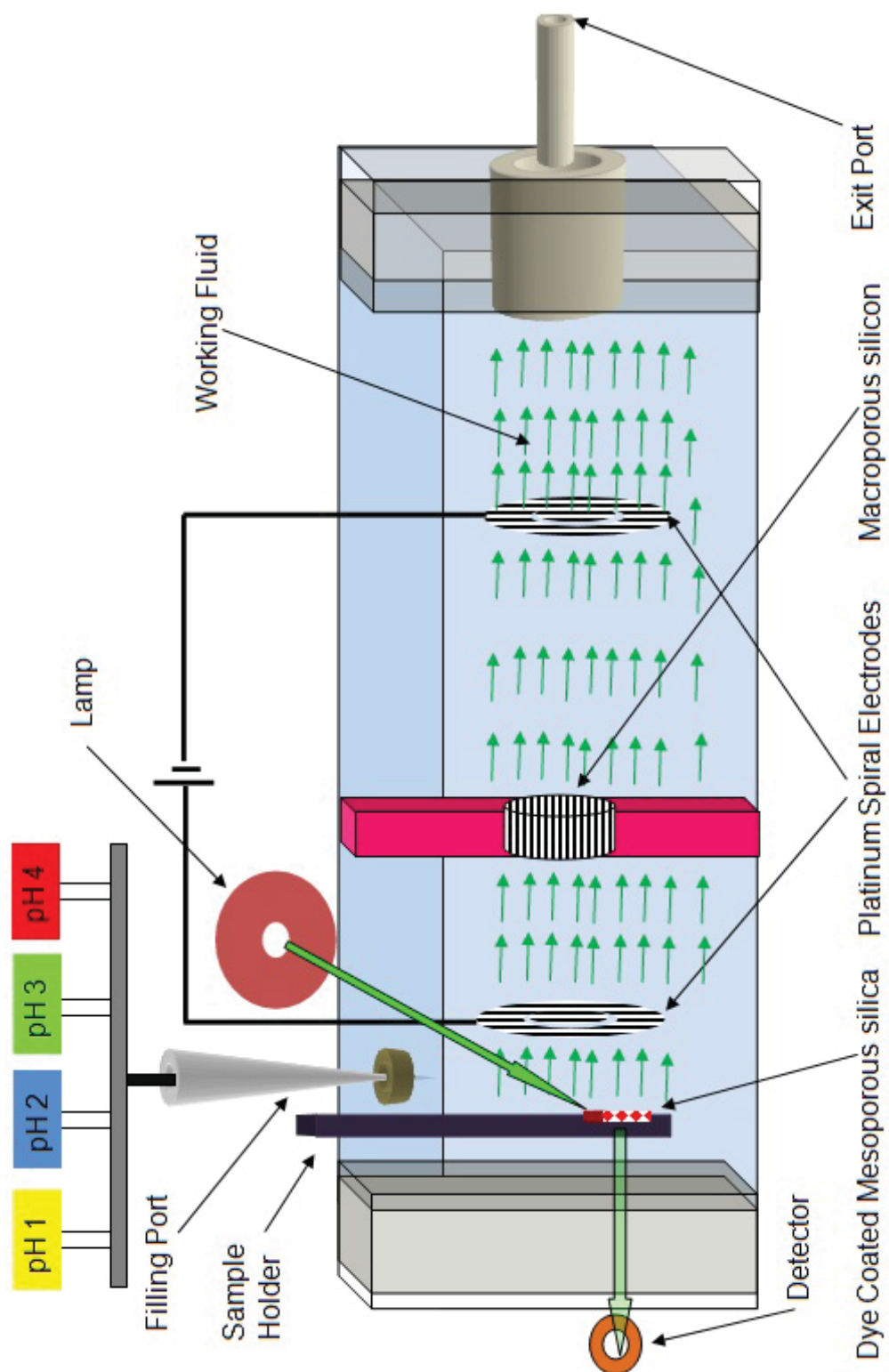


Figure 4.2: Schematic of the flow-through sensing device used in the study.

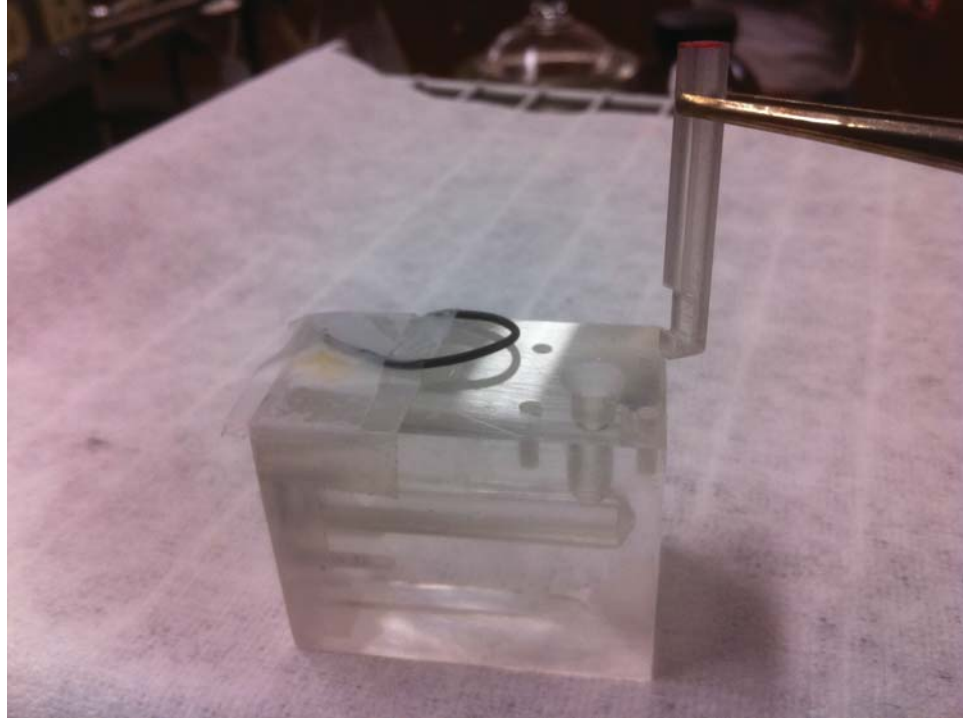
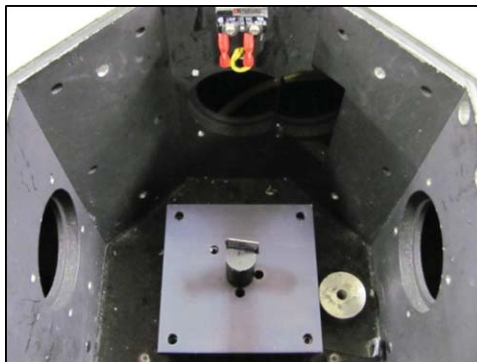
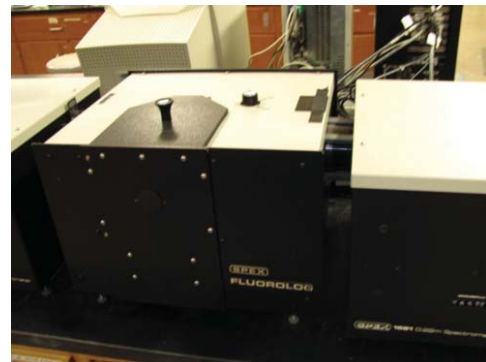


Figure 4.3: Fixture of the flow-through sensing device used in the study.



(a)



(b)

Figure 4.4: (a) porous silicon sample positioned on the fluorometer table for testing, (b) SPEX FLUOROLOG 1681 fluorometer setup.

Fig. 4.4 shows the SPEX FLUOROLOG 1681 fluorometer used for the fluorescence measurements.

4.3.1 Monolayer Preparation- Immobilization of Dye

The high surface area of porous silicon has created an interest in introducing different materials into pores. The surface of the anodized sample is terminated with various silicon-hydrogen bonds but will quickly form a thin native oxide when exposed to the ambient. The conventional methods of immobilizing a dye include soaking the sample in the dye or dispersing the dye on the sample surface using a syringe. For efficient infiltration and impregnation of the dye, the size of the dye molecule should be much smaller than the pore diameter. Figure 4.5 shows the different hypothetical configurations for dye immobilization that could be implemented during the experiment. Figure 4.5 (a) & Fig. 4.5 (b) shows the FE-SEM top and cross-sectional view of macroporous silicon. Figure 4.5 (c) & Fig. 4.5 (d) shows the dye on an un-oxidized porous silicon sample. Figure 4.5(e) & Fig. 4.5 (f) shows an oxidized porous silicon sample. Figure 4.5 (g) & Fig. 4.5(h) shows the dye on an oxidized porous silicon sample.

Silicon with a thin native oxide, quartz slides, and porous silica substrates have been used to explore the immobilization of fluorescein dye. All the substrates were cleaned for 1 hour in piranha solution (1:4 30 % H_2O_2 and concentrated H_2SO_4), rinsed several times with de-ionized water and dried in a dry air stream prior to any surface reaction. A glove box is utilized to perform the surface reactions in a nitrogen atmosphere. The freshly cleaned substrates were placed in a solution of 10 mM 3-aminopropyltriethoxysilane

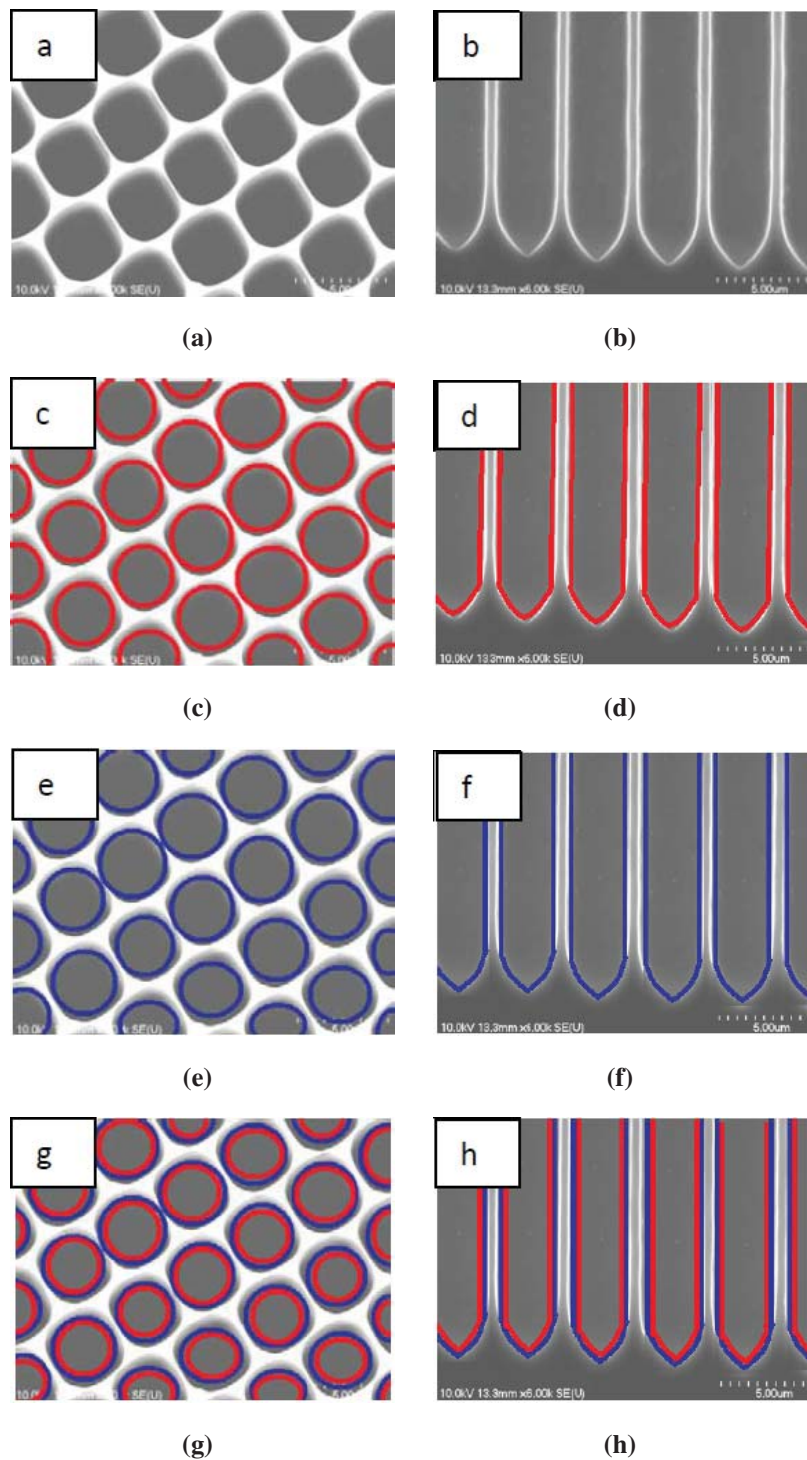


Figure 4.5: Hypothetical configurations for dye immobilization on porous silicon. (a), (b) are top and cross-sectional view of p (100) porous silicon sample, (c) & (d) dye coated sample, (e) & (f) oxidized porous silicon samples, and (g) & (h) dye coated on oxidized porous silicon.

(APTES) in dry toluene for 4 hours and then rinsed with toluene, dichloromethane, and ethanol [65]. The substrates were then placed in a solution of 0.1 mL of triethylamine and 10 mg fluorescein-5-isothiocyanate in 20 mL dry acetonitrile for 16 hours. Toluene and acetonitrile were freshly distilled. The chemical structures of fluorescein-5-isothiocyanate and fluorescein are shown in Fig. 4.6 (a) and Fig. 4.6 (b). The successful immobilization of fluorescein on the internal surface of porous silica is confirmed by the color change of porous silica before and after immobilization as shown in Fig. 4.7. The substrates were cleaned subsequently with acetonitrile, dichloromethane, ethanol and de-ionized water. All the substrates were immersed in de-ionized water before testing. Fluorescence spectra were recorded with a SPEX FLUOROLOG 1681 fluorometer. The pH of phosphate buffer solution was measured by a Accumet model 15 pH meter (Fisher Scientific), which was calibrated by pH 4.00, pH 7.00 and pH 10.00 standard buffer solutions. The dye coated porous silica substrate was immersed in buffer solution in the FTSD for all the fluorescent measurements.

4.3.2 Optical Constants of the Fluorescent Dye- Fluorescein

The optical constants, the refractive index (η) and extinction coefficient (κ) of the fluorescein were obtained from spectroscopic ellipsometric measurements. A monolayer of fluorescein dye is first immobilized on silicon wafer through covalent bonding between the dye and silicon. The refractive index of fluorescein is obtained by a Cauchy fit and it varied

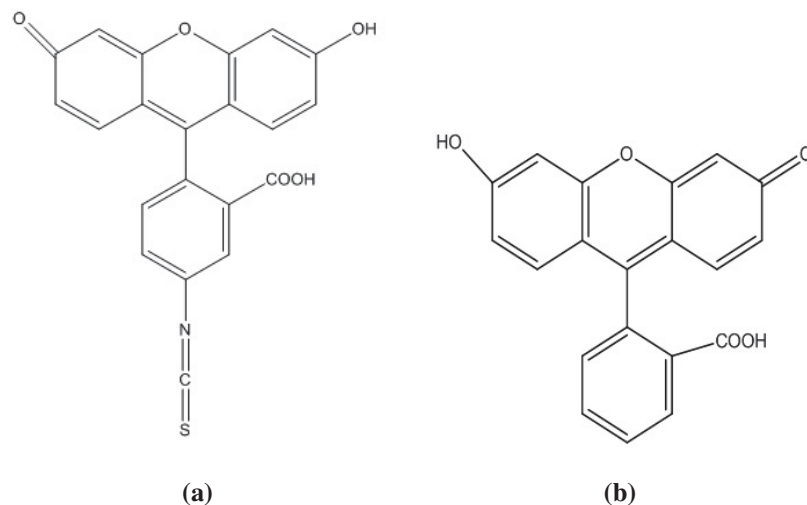


Figure 4.6: (a) chemical structure of fluorescein-5-isothiocyanate, and (b) fluorescein [Results from Qili Hu].

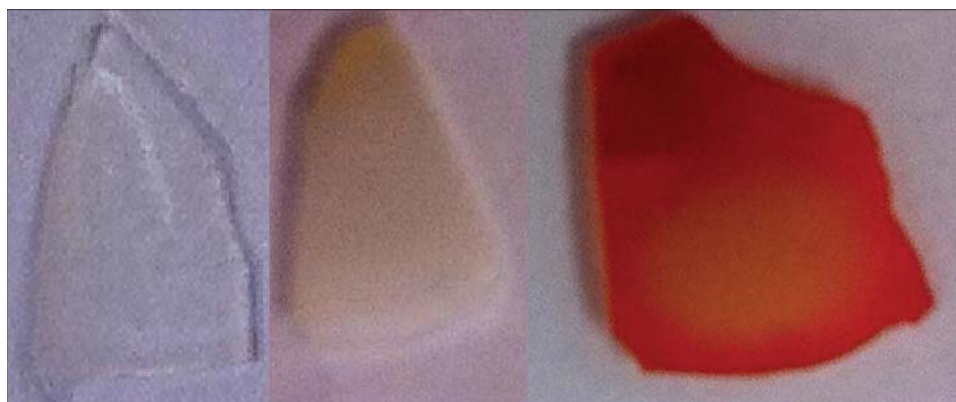


Figure 4.7: Images of porous silica untreated (left), immersed in fluorescein solution (middle) and fluorescein covalently bonded (right) [Results from Qili Hu].

from 1.5 to 2.4 in the wavelength 300 nm to 1000 nm as shown in Fig. 4.8. The thickness of the monolayer obtained is 3.2 nm with an MSE (mean square deviation) of 15.6. The model fit was performed by taking account of the 2 nm native oxide present on silicon. Optical measurements were obtained using a V-VASE 32 Ellipsometer (J.A. Wollam Co.).

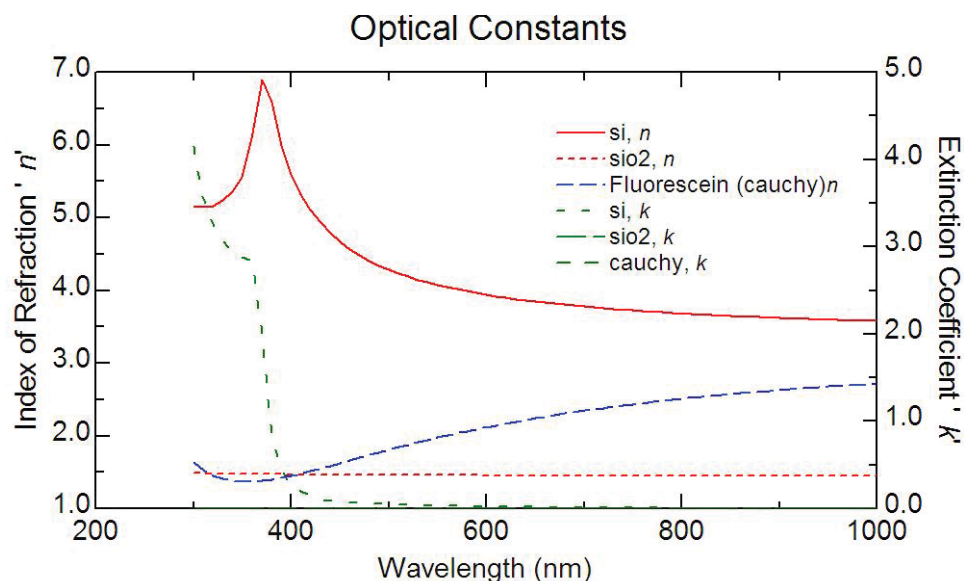


Figure 4.8: Variation of refractive index of fluorescein in the 300 - 1000 nm wavelength range.

4.3.3 Fluorescence Studies

All the fluorescence readings were taken under steady state conditions due to the ease of pH measurements. In this study, fluorescein was covalently bonded on the internal surface of porous silica to minimize leaching and improve sensor stability. It is observed that, compared to the covalently bonded fluoroscein on a flat quartz slide, the immobilization on porous silica increases the amount of dye for pH measurements, which resulted in 5 - 10 times higher fluorescence intensity. It exhibited two different pH-dependent excitation peaks corresponding to the protonated (acidic, 468 nm) form and the deprotonated (basic, 490 nm) form and a single emission peak (512 nm). The presence of dual excitation peaks facilitates the ratiometric pH measurement.

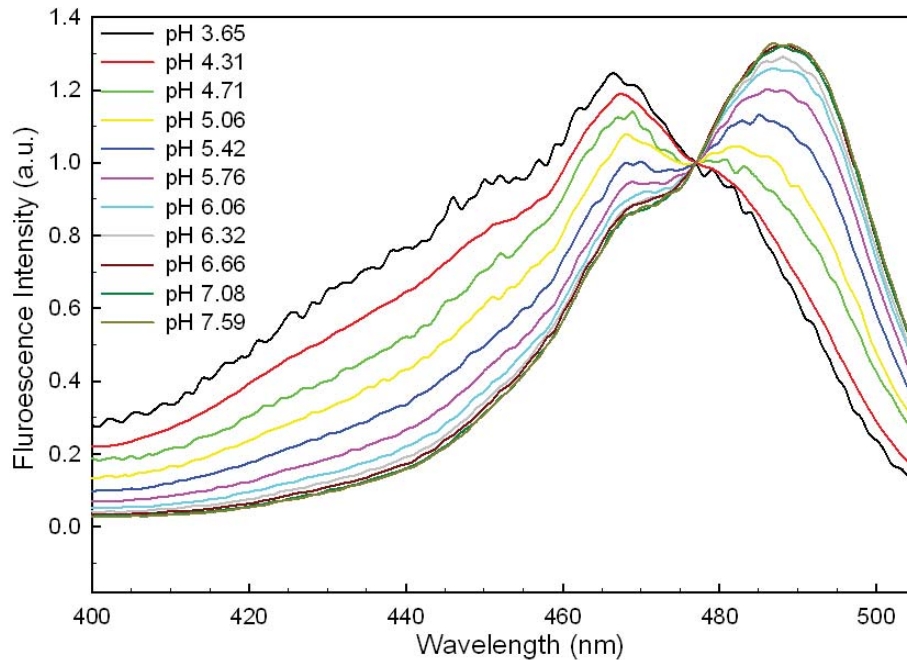


Figure 4.9: Normalized fluorescence excitation spectra of fluorescein (1.00 mM) in buffer solution with emission peak at 520 nm [Results from Qili Hu].

The fluorescence excitation spectra were recorded in the range of 400 - 505 nm with emission wavelength at 520 nm in phosphate buffer solution with 0.03 M ionic strength at room temperature. The dual excitation spectra of fluorescein in buffer solution as shown in Fig. 4.9 were similar to the excitation spectra of fluorescein on porous silica Fig. 4.10. The excitation peaks at 468 nm and 490 nm are apparent on both spectra. For ratiometric detection, the excitation intensity ratio (R) is defined here as the excitation intensity at 490 nm with 520 nm emission divided by the excitation intensity at 468 nm with 520 nm emission as well.

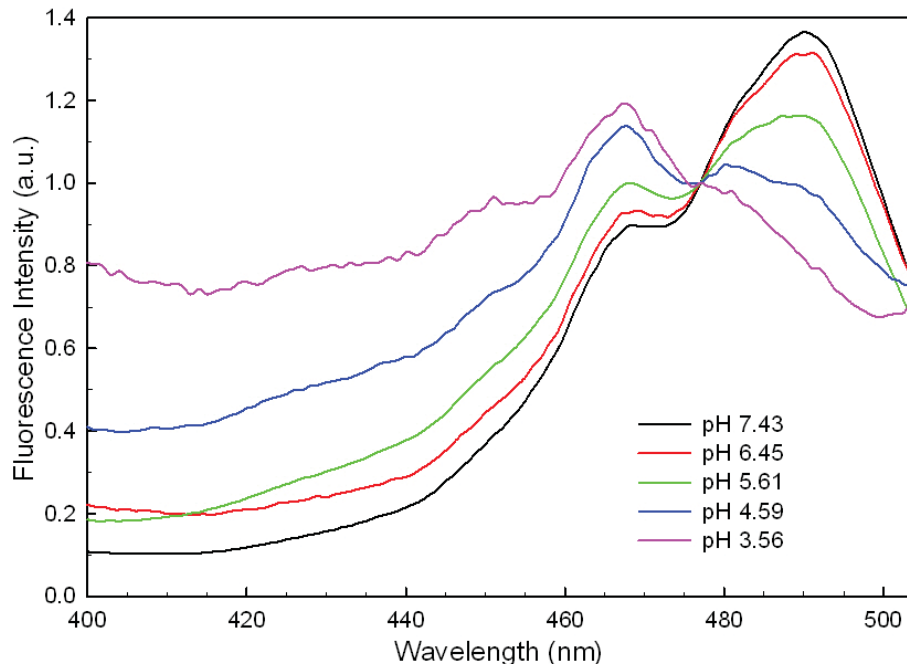


Figure 4.10: Normalized fluorescence excitation spectra of fluorescein immobilized on porous silica [Results from Qili Hu].

Fluorescein in buffer solution responded to pH over the range of 3.0 - 8.0 with the most sensitive dynamic range occurring between pH 4.6 and pH 6.6 ($R = 0.9928$) as shown in Fig. 4.11. Similarly, porous silica with immobilized fluorescein responded to pH over the range of 3.0 - 8.0. A linear relationship was observed between excitation ratio (R) of fluorescein and pH of buffer solution in pH range 3.0 - 7.5 ($R = 0.9862$) as shown in Fig. 4.12. In addition, the excitation ratio of fluorescein is relatively reproducible making it a promising pH sensor.

Upon covalent immobilization of fluorescein at the surface, the apparent acid dissociation constant, pK_a , changes by as much as 3 pK units [67]. This apparent pK_a

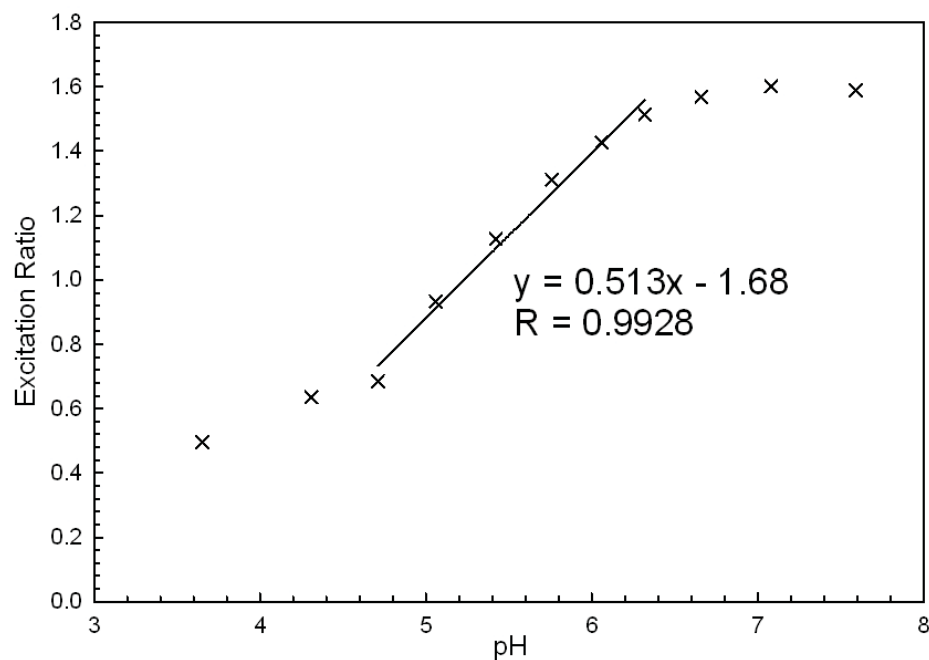


Figure 4.11: Relationship between pH and excitation ratio of fluorescein in buffer solution [Results from Qili Hu].

shift was observed in this study too, the apparent pKa of fluorescein slightly increased after immobilization as shown in Fig. 4.13. The apparent acid dissociation constant, pKa, can be obtained at pH values of crossing points. In Fig. 4.13, HA% and A-% represents the percentages of acidic and basic forms of fluorescein in the total concentration of fluorescein present. HA% and A-% values of fluorescein in buffer and porous silica at 468 and 490 nm are plotted against the different pH values from 3 - 8 respectively. As evident from the plot, in the lower pH range (pH 3 - 4), all the fluorescein molecules are in the acidic form with HA% is equal to 100 with corresponding A-% value of 0. Similarly, in the higher pH range (pH 6 - 8), all the fluorescein molecules are in the basic form with HA% equal to 0 and corresponding A-% value of 100. The slightly lower acidity value of fluorescein

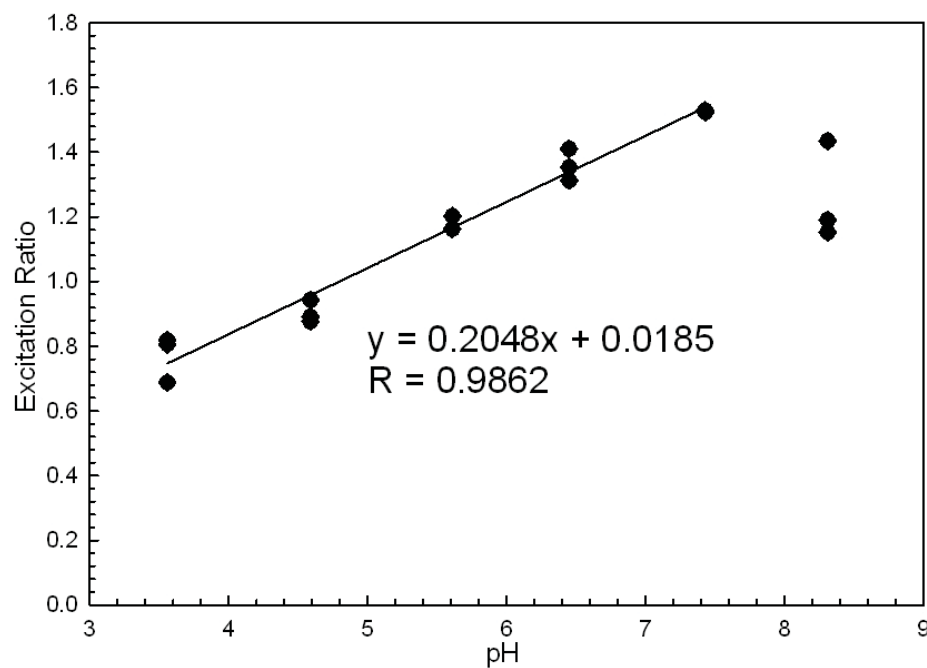


Figure 4.12: Relationship between pH and excitation ratio of fluorescein in porous silica [Results from Qili Hu].

(present in electronic ground state) that is immobilized on porous silica is attributed to the micro-environment from the porous network of porous silica.

4.3.4 Sensitivity of the pH Sensor

Sensitivity of a sensor is an important parameter which is defined as either the minimum change in input signal or parameter that results in a detectable output signal (DY/DX , the slope of the graph). From Fig. 4.11, the slope or sensitivity calculated for a unit pH change is 0.51 (change in excitation ratio), while the sensitivity in the case of fluorescein in porous

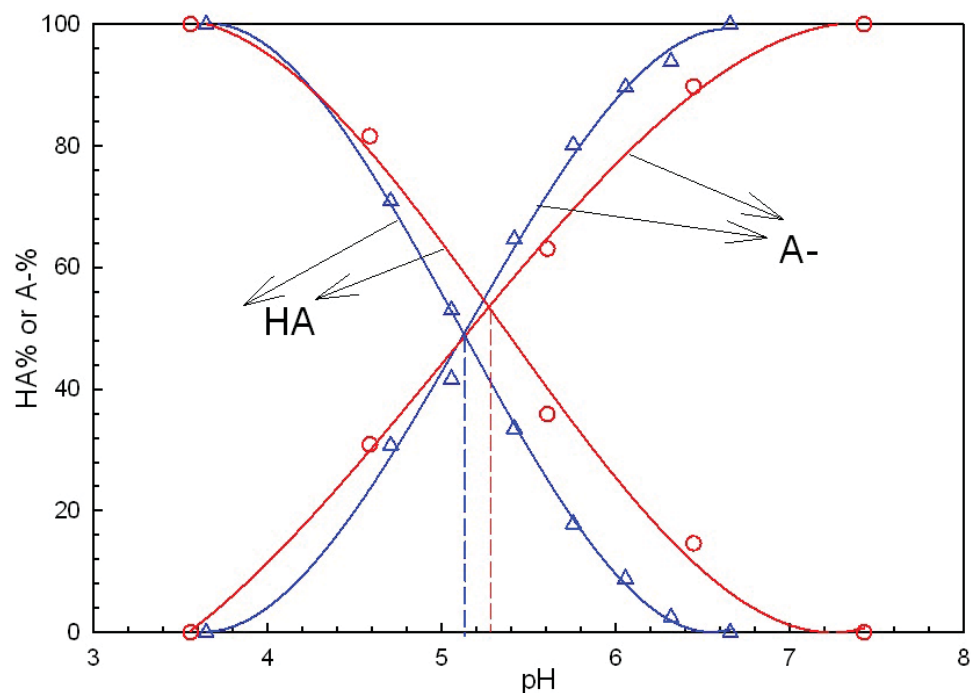


Figure 4.13: Plot of HA% and A-% of fluorescein vs. pH in buffer solution (blue triangles) and porous silica (red circles). Crossing points indicate pKa of fluorescein in different environments [Results from Qili Hu].

silica template from Fig. 4.12 is ~ 0.2 (change in excitation ratio).

The sensitivity of the sensor measurement is maximum when the acid and base forms of the dye are present in equal proportions, in the linear range of both Fig. 4.11 and Fig. 4.12. Higher acidic or basic forms results in saturation effects and is seen in the pH range of 3 - 4.6 and 6.4 - 8.0 in Fig. 4.11 which is not a useful sensing range.

Advantages of using porous silica templates for sensing applications include, infrequent need for preparation of mesoporous silica sensing template with dye compared to dye in buffer solution that is prepared frequently. Fluorescein immobilized on porous

silica template can be used for multiple experiments for a long time. Issues related to scattering from porous silica templates during sensing needs to be resolved as it reduces the amount of light or signal that reaches the detector and hence reduces the efficiency of the sensor. Further improvements are required for increasing the transparency of FTSD fixture walls as it also reduces the light that reaches the sensing material and the detector. In addition, all the signal coming from the sensing template (in a 360° radius) doesn't reach the detector as it is positioned at 90° with respect to the detector. Further engineering and optical design is required to capture the entire sample signal for sensing.

4.4 Real Time Implementation of FTSD in Lakes

The relatively compact size and light weight of the FTSD creates less challenges towards the actual implementation of the device for a real world testing of pH of waters in lakes and reservoirs. As mentioned earlier, the FTSD device could be mounted or suspended on a buoy or a robotic vehicle. Important factors that should be considered while transferring the FTSD from a lab environment to a lake or reservoir involves the power supply to provide the necessary current and voltages.

4.5 Summary

Mesoporous silica templates have been successfully implemented for the immobilization of fluorescein for fluorescence studies. Electro-osmotic pump is successfully modified to incorporate dye immobilized mesoporous silica templates. Fluorescence results and characterization confirm the successful pH measurement from ratiometric techniques. A linear relationship is obtained between excitation ratio $I_{490/468}$ and solution pH ($R = 0.9862$) making it a good candidate for pH sensing.

Chapter 5

Conclusions And Future Work

A portable flow-through sensing system is proposed with the implementation of porous silicon technology. Macroporous silicon membranes with a regular array of through-wafer pores ($> 500 \mu\text{m}$) and diameters $3 - 4 \mu\text{m}$ in a 3.5 mm circle are fabricated utilizing arrays of inverted pyramidal pits. Both dielectric and metal masks are implemented as a mask material for anodization of silicon. A porous media that is compatible with the current micro-fabrication technology is fabricated successfully.

Through-wafer mesoporous silicon membranes are fabricated with near vertical and uniform pores with pore diameters of $10 - 200 \text{ nm}$ and pore depths of $500 \mu\text{m}$ by anodizing silicon substrates with resistivity of $0.001 - 0.002 \Omega\text{-cm}$. These porous membranes are thermally oxidized to form complete silica membranes that were used for

dye immobilization.

Macroporous silicon is utilized as pump media to reproduce results of a large flow rate of $11.9 \mu\text{l min}^{-1} \text{ mm}^{-2}$ and a maximum pressure of 5.2 kPa at 60 volts earlier demonstrated by Zheng et al. Flow rate and maximum pressure measurements on mesoporous silica membranes indicate that the smaller pore diameter improves maximum pressure response and impacts maximum flow rate based on morphology, yielding flow efficiencies of $2.8 \mu\text{l/min/V/cm}^2$ and pressures of 92 Pa/V. Challenges related to the mechanical strength of the porous membrane are addressed by considering alternate method of selective porosification of silicon. Permeability of the mesoporous silicon membrane is tested with the working fluid.

Optical characterization on mesoporous silica membranes was performed using ellipsometry from 300 - 1000 nm. This study was done to understand the behavior of the dye-immobilized porous silica templates during fluorescence measurements. From the transmission measurements on mesoporous silica, it is observed that there is a decrease in absorption loss for the oxidized mesoporous silicon samples compared to un-oxidized mesoporous silicon samples as expected due to the formation of SiO_2 [10]. X-ray diffraction measurement on mesoporous silica samples confirms the presence of fully oxidized membranes. Angular transmission as well as angular reflection decreases with decrease in incident angle.

The refractive index (n) values for oxidized and un-oxidized mesoporous silicon

Sample C at 1000 nm are 1.36 and 1.66 respectively. The decrement in refractive index implies that the mesoporous silicon has been oxidized into mesoporous silica, given that the refractive index of bulk silicon is ~ 3.5 and bulk silica is ~ 1.4 at 1000 nm. The extinction coefficient (k) for a thick ($550\ \mu\text{m}$) mesoporous silica samples is 2.5×10^{-4} and for a thin ($1\ \mu\text{m}$) mesoporous silica is 7.5×10^{-7} . Difference of three orders of magnitude in k is a direct measurement of the opacity of mesoporous silica sample. The measured absorption coefficient (α) for the $550\ \mu\text{m}$ thick mesoporous silica membrane is $31.8\ \text{cm}^{-1}$. The porosity (p_{PS}) of mesoporous silicon (Sample A) calculated from the experimental values obtained using ellipsometric measurements is 67%, which compares very well to the experimental results obtained by Zheng et al. at 60%.

The porosity decreases with thermal oxidation of porous silicon and is confirmed by Bruggemann model as well as Image J analysis. The initial measurements of normal incidence optical transmission indicate promising results to use these mesoporous silica membranes for visible to the near infrared regime applications. Potential applications that could result from mesoporous silica material include flow-through porous membrane for chemical and biological detections.

Mesoporous silica and macroporous silicon samples have been successfully implemented for dye immobilization and electro-osmotic pumping for flow-through fluorescence sensing and are integrated into a flow-through sensing system as proposed in the research statement in Section 1.8 of Chapter 1. Fluorescence results and

characterization confirm the successful pH measurement from ratiometric techniques. A linear relationship is obtained between excitation ratio $I_{490=468}$ and solution pH ($R = 0.9862$) making mesoporous silica a good candidate for pH sensing. Porous silica membranes are efficient templates for immobilization of optical dyes and represent a promising method to increase sensitivity for small variations in chemical properties.

The FTSD represents a device topology suitable for application to long term monitoring of lakes and reservoirs. In real time implementation, the FTSD can be suspended using a buoy or a robotic vehicle for pH measurements. This implementation requires onboard power supply and fluorescence setup and require appropriate engineering.

5.1 Future Work

5.1.1 300 nm pore size for EOP

Porous silicon is a very promising material and has a potential for many new applications including microfluidics, micro gas chromatography, photovoltaics, nano-electronics, and super-capacitors. During this research, novel materials and applications were found that are based on porous silicon but were not pursued as they fall outside the scope of this dissertation.

From a theoretical calculation, mesoporous silica material implemented as a porous media for electro-osmotic pump should result in a really high pressure value. But from our research it was found that the flow rate and pressure capacities were limited by the 10 - 50 nm pore size when compared to a macroporous silicon sample with 3 μm pore size as there was restriction of water flow due to the size of water molecule (~ 100 nm). From the work of Chun et al., the electric double layer thickness can be reduced to 3 nm by the addition of pH buffers like tris-EDTA to the working fluid. Further experiments related to impact of these solutions on the performance of the porous membrane for EOP application is an important future study.

In order to obtain the desired flow rates and pressure capacities, it is important to identify the pore size and membrane thickness that would allow flow of fluid in the porous channels. Any pore size that is greater than the EDL thickness can offer promising results. A pore diameter in the range of 300 nm could be ideal for the desired applications. Challenges related to oxidizing the pores while keeping the membrane integrity need better understanding of controllability on the pore size. In addition, identifying the appropriate resistivities for silicon substrates that will produce pore sizes in the 300 nm range after electrochemical anodization is important and a thorough study is required.

Another approach for achieving a 300 nm pore size channels on a porous silicon sample may be to deposit materials onto the sidewalls of a 3 μm pore thereby reducing the pore size. Deposition techniques like electrolytic deposition (electro-deposition) or a

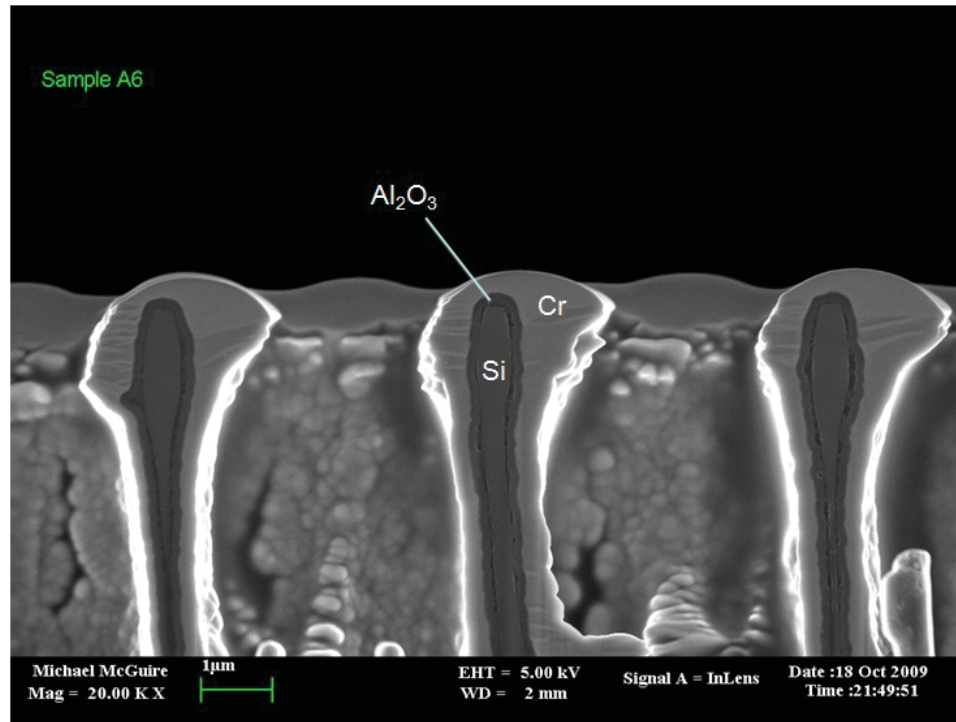


Figure 5.1: Atomic layer deposition of Al_2O_3 films in porous silicon done in collaboration with Dr. Conley at Oregon State University, OR. SEM image was made by ON Semiconductor in Gresham, Oregon. [Permission in Appendix].

vapor based deposition technology like ALD (Atomic layer deposition) can be pursued for depositing a very uniform and conformal coating inside the pores.

Figure 5.1 shows some initial study on depositing Al_2O_3 in the pores of porous silicon which was conducted in collaboration with Dr. John Conley at Oregon State University, OR [68].

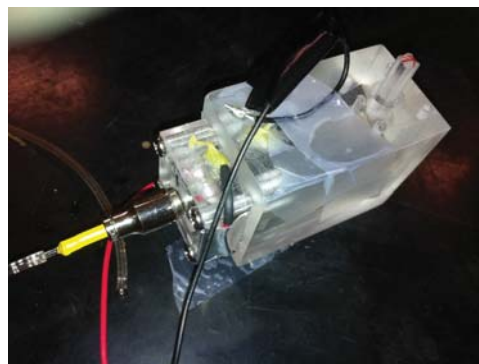
5.1.2 Flow-Through Measurement - FTSD

An important aspect for the FTSD that pertains to the dynamic measurement of fluorescent signal for pH measurements. An attempt was made to obtain fluorescence signal from the FTSD during the pump operation as shown in Fig. 5.2. The data was recorded in the following manner,

1. The reservoirs were first filled with DI water and a fluorescence reading was taken with the pump in operation.
2. With the pump still in operation, a couple of drops of buffer solution (pH=8, prepared by Qili Hu) were introduced into the larger reservoir. Fluorescence readings were taken after 1 min and 5 min. The pH of the liquid exiting the outlet of the FTSD is measured using pH paper. After a minute of pumping, the pH remained the same as DI water. But, after 5 minutes of pumping, pH reading reached a constant value of pH 8, a fluorescence reading was taken.
3. Again, a buffer solution of pH 5.1 was introduced into the reservoir and a fluorescence measurement was taken after 5 min. This demonstration of dynamic measurement of pH needs further study and optimization of the complete testing system.



(a)



(b)



(c)



(d)



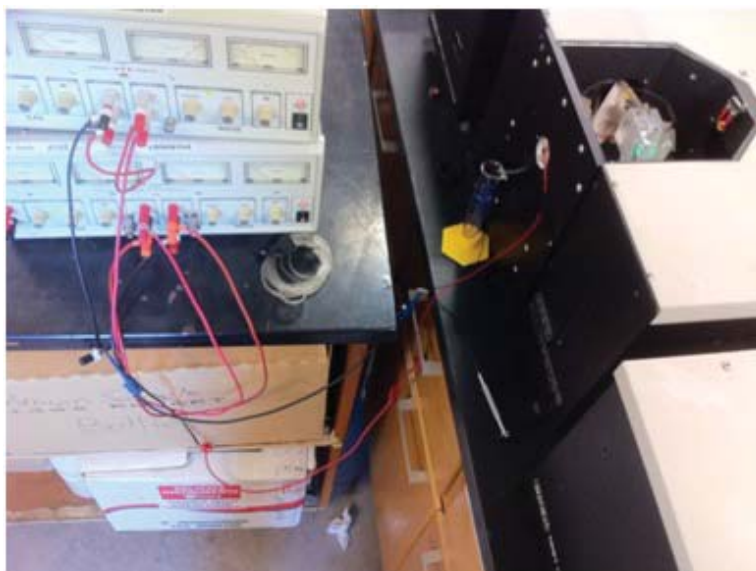
(e)



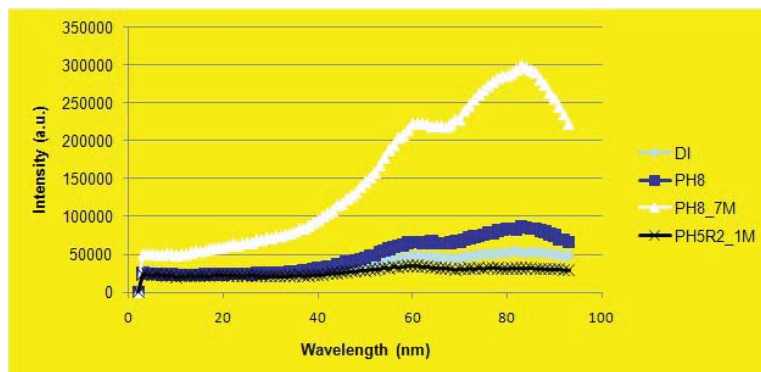
(f)

Figure 5.2: A preliminary test sequence for measuring different pH in a dynamic flow-through fluorescence experiment, a) water exiting the FTSD during operation, b) FTSD in operation, c) initial pH measurement with a pH paper, d) buffer solution with pH 8 is introduced, e) A new pH reading is taken, and f) Another reading taken at a different pH.

Figure 5.3 (a) shows the complete setup used for dynamic fluorescence measurements. Figure 5.3 (b) shows some initial fluorescence results as new solutions with different pH are introduced into the FTSD while the pump is in operation.



(a)



(b)

Figure 5.3: Setup utilized for dynamic flow-through fluorescence experiments, (a) complete setup for a dynamic flow-through pH sensing, (b) fluorescence results with different buffer solutions in the dynamic test setup.

Some challenges in the FTSD testing can be resolved after addressing the following,

1. Fabrication of uniform, planar, and sturdy mesoporous silica samples are critical in obtaining reproducible fluorescence results. Most samples that are fabricated are non-planar as the mesoporous silica sample bows during thermal oxidation as shown in Fig. 5.4. This bowing introduces a curvature to the sample making it harder for mounting as well as for obtaining a repeatable signal. Also being very fragile, the sample breaks easily and handling the sample becomes challenging. Porosifying larger wafers will result in relatively larger mesoporous silica samples that are easy to implement. Improvements in fixture design and positioning of the optical elements in future FTSD configurations will serve to improve resolution of the measured signal and reduce the impact of dead volume inside the fixture.
2. Further fluorescence characterization study is required to improve the resolution of pH measurements.
3. Thorough optical characterization of immobilized dyes on mesoporous silica samples is important for improving and understanding flow-through sensing.

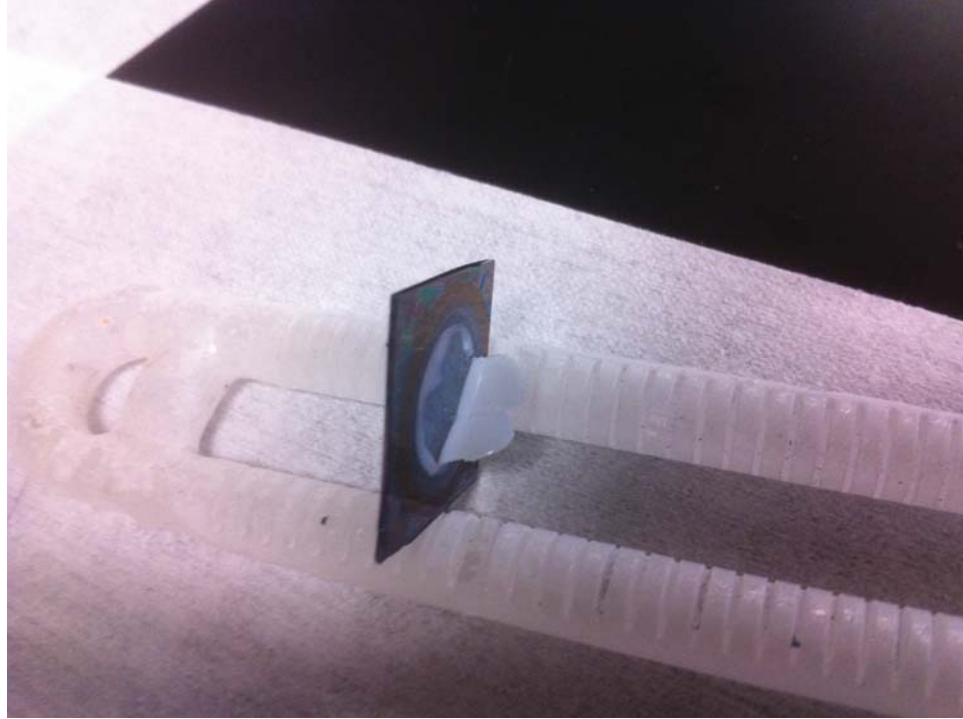


Figure 5.4: Bowing of mesoporous silica sample during thermal oxidation.

5.1.3 Silicon Nanorod Fabrication And Applications

Figure 5.5 shows SEM images of silicon nanorods (SiNRs) formed during the electrochemical anodization of *p*-type (100) silicon substrates at high current densities. The electrical, optical and mechanical properties of silicon nanorods and silicon nanowires could have some interesting applications. On an average, the SiNRs have lengths about 100 - 200 μm and widths varying from 100 - 400 nm.

There is a significant research and growing interest in integrating nanostructures for various applications including thermoelectric, photovoltaic, DNA sensing and high speed

switching devices [69], [70], [71]. Charge transport by the carriers in nanostructured materials has importance in nanosystem applications. SiNRs and SiNWs have been studied to much lesser extent compared to other materials like carbon nanotubes or ZnO nanorods or nanotubes and this could be attributed to fact that growing silicon nanorods or wires is not as well understood.

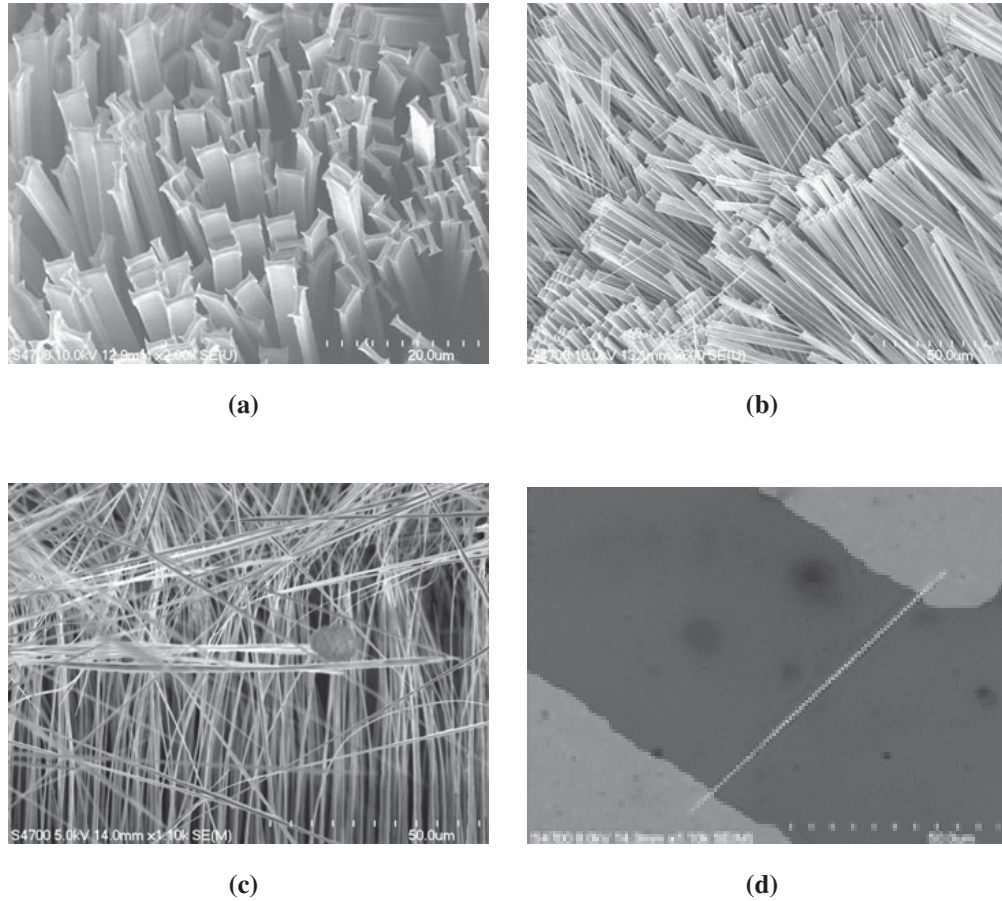


Figure 5.5: (a) Vertical silicon nanorod at high current density, (b) SiNR as etched at an angle, (c) SiNRs are drawn together after rinsing due to surface tension, and (d) silicon nanorod manipulated onto electrical contact pads for I-V measurements.

During electrochemical anodization the pore walls are formed along the $\langle 100 \rangle$

direction. The sidewalls of the pore with (100) planes break up at the edge of the pores that have comparatively high stress resulting in the SiNR profile as seen in the Fig. 5.5 (a). Figure 5.5 (b) shows the profile of SiNR as etched at an angle. In the Fig. 5.5 (c), SiNRs are drawn together after rinsing due to surface tension, and Fig. 5.5 (d) shows an SEM image of silicon nanorod manipulated onto electrical contact pads for I-V measurements.

For specific device applications, it is important to have good control over the physical dimensions of these SiNRs. Applied current density and substrate resistivity are two important parameters for this control. Substrates with a lower resistivity generate macro pores with thinner side walls, which effectively increase the total pore area [60].

References

- [1] <http://www.kywater.org/www/ramp/rmph.htm>
- [2] <http://contentdm.lib.byu.edu/ETD/image/etd2145.pdf>
- [3] D.J. Laser and J.G. Santiago, “A review of micropumps,” *Journal of Micromechanics and Microengineering*, vol. 14, pp. R35-R64, 2004.
- [4] J.P. Barber, D.B. Conkey and J.R. Lee, “Fabrication of hollow waveguides with sacrificial aluminum cores,” *IEEE Photonics Technology Letters*, vol. 17, pp. 363-365, 2005.
- [5] X. Wang, C. Cheng and S. Wang, “Electroosmotic pumps and their applications in microfluidic systems,” *Microfluidics and Nanofluidics*, vol. 6, pp. 145-162, 2009.
- [6] X.H. Yang and L.L. Wang, “Fluorescence pH probe based on microstructured polymer optical fiber,” *Optics Express*, vol. 15, no. 25, pp. 16478-16483, Dec. 2007.

- [7] J.C. Bruno, E. Lewis and J.Scully, "A novel technique for optical fiber pH sensing based on methylene blue adsorption," *Journal of Light Wave Technology*, vol. 13, no. 7, Jul. 1995.
- [8] O. Chailapakul, P. Ngamukot and A.Yoosamran, "Recent Electrochemical and Optical Sensors in Flow-Based Analysis," *Sensors*, vol. 6, pp. 1383-1410, 2006.
- [9] W. Gan, L. Yang and Y. He, "Mechanism of porous core electroosmotic pump flow injection system and its application to determination of chromium(VI) in waste-water," *Talanta*, vol. 51, pp. 667-675, 2000.
- [10] S. Yao, D. Huber and J.C. Mikkelsen, "Porous glass electroosmotic pumps: design and experiments," *Journal of Colloid and Interface Science*, vol. 268, pp. 143-153, 2003.
- [11] J.Z. Wallner, N. Nagar, C.R. Friedrich and P.L. Bergstrom, "Macro porous silicon as pump media for electro-osmotic pumps," *Physica Status Solidi a*, vol. 204, pp. 1327-1331, 2007.
- [12] R.Z. Zusman, C. Rottman and M.Ottolenghi, "Doped Sol-Gel Glasses as Chemical Sensors," *Journal of Non-Crystalline Solids*, vol. 122, pp. 107-109, 1990.
- [13] N.A. Yosuf and M. Ahmad, "flow-through optical fibre reflectance sensor for the detection of lead ion based on immobilised gallocynine," *Sensors and Actuators B*, vol. 94, pp. 201-209, 2003.

- [14] E. Thrush, O. Levi and W.Ha, "Integrated bio-fluorescence sensor," *Journal of Chromatography*, vol. 1013, pp. 103-110, 2003.
- [15] M. Dandin, P. Abshire and E. Smela, "Optical filtering technologies for integrated fluorescence sensors," *Lab on a Chip*, vol. 7, pp. 955-977, 2007
- [16] M. Staiano, M.D. Champdore and S.Borini, "New Emergent Nanotechnologies in Medical and Biochemical Applications: Advanced Fluorescence Protein-Based Nanosensors," *Current Chemical Biology*, vol. 1, pp. 3-9, 2007.
- [17] B.H. Weigl and O.S. Wolfbeis, "Capillary Optical Sensors," *Analytical Chemistry*, vol. 66, pp. 3323-3327, 1994.
- [18] A. Uhler, "Electrolytic shaping of germanium and silicon," *The Bell System Technical Journal* (USA), vol. 35, p. 333, 1956.
- [19] T.R. Turner, "Electropolishing Silicon in Hydrofluoric Acid Solutions," *Journal of The Electrochemical Society* (USA), vol. 105, p. 402, 1958.
- [20] L.T. Canham, "Silicon quantum wire array fabrication by electrochemical and chemical dissolution of wafers," *Applied Physics Letters* (USA), vol. 57, p. 1046, 1990.
- [21] Y. Watanabe and T. Sakai, Japan Patent No. 49-19030 (1974), UK Patent No. 1287221 (1972), USA Patent No. 3640806 (1972).
- [22] K. Seno, Japan Patent No. 49-19019 (1974).

- [23] T.I. Cox, "Electroluminescence from porous silicon using solid state contacts," in Properties of Porous silicon, L. Canham, Ed., London, UK: INSPEC, The Institute of Electrical Engineers, pp. 290-310, 1997.
- [24] M. Thurst, Measurement Science and Technology, Uk, vol. 7, pp. 26-9, 1996.
- [25] R.C. Anderson, R.S. Muller and C.W. Tobias, "Investigations of porous silicon for vapor sensing," *Sensors and Actuators A: Physical*, vol. 21-23, pp. 835-839, 1990.
- [26] A. Richter, Transducers (Japan), pp. 310-3, 1993.
- [27] D. Stievenard and D. Deresmes, "Gas Sensor Using an Aluminium-Porous Silicon Junction Application to the Detection of Non-Zero Molecular Dipole Moment," *Materials Research Society Symposium Proceedings (USA)*, vol. 358, pp. 599-604, 1995.
- [28] V. P. Bondarenko and V. A. Yakovtseva, "Optoelectronic applications of porous silicon", in Properties of Porous silicon, L. Canham, Ed., London, UK: INSPEC, The Institute of Electrical Engineers, pp. 356-263, 1997.
- [29] L.T. Canham, "Biomedical applications of porous silicon", in Properties of Porous silicon, L. Canham, Ed., London, UK: INSPEC, The Institute of Electrical Engineers, pp. 371-376, 1997.

- [30] V. Lehmann, "A new capacitor technology based on porous silicon", in Properties of Porous silicon, L. Canham, Ed., London, UK: INSPEC, The Institute of Electrical Engineers, pp. 390-396, 1997.
- [31] W. Lang and P. Steiner, "Porous silicon for thermal sensors. Sensors and Materials," *Sensors and Materials* (Japan), vol. 8, no. 6, pp. 327-344, 1996.
- [32] S. Zeng, C. Chen and J. Santiago "Electroosmotic flow pumps with polymer frits," *Sensors and Actuators B*, vol. 82, p. 209, 2002.
- [33] S. Yao and J. G. Santiago, "Porous glass electroosmotic pumps: Theory," *Journal of Colloid and Interface Science*, vol. 268, pp. 143-153, 2003.
- [34] D.J. Laser, A.M. Myers and S.Yao, "Silicon electroosmotic micropumps for integrated circuit thermal management," *Transducers, Solid-state Sensors, Actuators Microsystems*, 12th International Conference, vol. 1, pp. 151-154, 2003.
- [35] K. Vanga, D. Cheam, C. Middlebrook and P. Bergstrom, "Optical properties of thick ordered mesoporous silica membranes," *Physica Status Solidi (c)*, vol. 8, no. 6, pp. 1941-1945, 2011.
- [36] W. Gan, L. Yang and Y.He, "Mechanism of porous core electroosmotic pump flow injection system and its application to determination of chromium(VI) in waste-water," *Talanta*, vol. 51, pp. 667-675, 2000.

- [37] S. Yao, D. Huber and J.G. Santiago, "Porous Glass Electroosmotic Pumps: Design and Experiments," *Journal of Colloid and Interface Science*, vol. 268, pp. 143-153, 2003.
- [38] S. Muthu, F. Svec and Y.B. Gianchandani, "Enhanced electro-osmotic pumping with liquid bridge and field effect flow rectification," 17th IEEE International Conference on Micro Electro Mechanical Systems (MEMS 2004), pp. 850-853, 2004.
- [39] C. Lingxin, G. Yafeng and M.Jiping, Chinese Science Bulletin, vol. 48, no. 23, pp. 2572-2577, 2003.
- [40] P. Wang, Z. Chen and H.C. Chang, "A new electro-osmotic pump based on silica monoliths," *Sensors and Actuators B*, vol. 113, pp. 500-509, 2006.
- [41] C.L. Rice and R.J. Whitehead, "Electrokinetic Flow in a Narrow Cylindrical Capillary," *The Journal of Physical Chemistry*, vol. 69, pp. 4017-4024, 1965.
- [42] D.J. Laser and J.G. Santiago, "A review of micropumps," *Journal of Micromechanics and Microengineering*, vol. 14, pp. R35-R64, 2004.
- [43] S. Bhattacharyya, Z. Zheng and A.T. Conlisk, "Electro-osmotic flow in two-dimensional charged micro- and nanochannels," *The Journal of Fluid Mechanics*, vol. 540, pp. 247-267, 2005.

- [44] M.S. Chun, “Electrokinetic Flow Velocity in Charged Slit-like Microfluidic Channels with Linearized Poisson-Boltzmann Field,” *The Korean Journal of Chemical Engineering*, vol. 19, no. 5, pp. 1-6, 2002.
- [45] Malvern Instruments Ltd [www.malvern.com], Enigma Business Park, Grovewood Road, Malvern, Worcestershire WR14 1XZ, United Kingdom, Support Centre: Tel: +44 (0) 1684 891800
- [46] J. Zheng, M. Christophersen and P.L. Bergstrom, “Thick Macroporous Membranes Made of p-type Silicon,” *Physica Status Solidi (a)*, vol. 202, no. 8, pp. 1402-1406, 2005.
- [47] W.A. Khan and M.M. Yovanovich, “Optimization of PIN-FIN Heat Sinks in Bypass Flow Using Entropy Generation Minimization Method,” Proceedings of IPACK2007, Asme Interpack 07, 2007.
- [48] M.K. Oisten and P.L. Bergstrom, “A Young’s modulus study of n- and p-type porous silicon,” *Physica Status Solidi (a)*, vol. 206, no. 6, pp. 1278-1281, 2009.
- [49] I. Rea, M. Iodice and G.Coppola, “A porous silicon-based Bragg grating waveguide sensor for chemical monitoring,” *Sensors and Actuators B: Chemical*, vol. 139, pp. 39-43, 2009.
- [50] M. Haurylau, J. Zhang and M.Weiss, “Nonlinear Optical Response Of Photonic Bandgap Structures Containing PbSe Quantum Dots,” *Journal of Photochemistry and Photobiology A: Chemistry*, vol. 183, pp. 329-333, 2006.

- [51] E. Lorenzo, C.J. Oton and N.E. Capuj, "Porous silicon-based rugate filters," *Journal of Applied Optics*, vol. 44, no. 26, pp. 5415-5421, 2005.
- [52] D. Konjhodzic, H. Bretinger and F.Marlow, "Structure and properties of low-n mesoporous silica films for optical applications," *Thin Solid Films*, vol. 495, pp. 333-337, 2006.
- [53] E.V. Astrova, L.I. Korovin and A.D. Lang, "Optical Transparency of Macroporous Silicon with Through Pores," *Semiconductors*, vol. 37, no. 1, pp. 57-64, 2003.
- [54] N.J. Hutchinson, A. Coquil and A.Navid, "Effective Optical Properties of Highly Ordered Mesoporous Thin Films," *Thin Solid Films*, vol. 518, pp. 2141-2146, 2010.
- [55] A.P. Hakhoyan and S.V. Melkonyan, "Features of the refractive index of porous silicon with gradient porosity," *Armenian Journal of Physics*, vol. 1, pp. 146-150, 2008.
- [56] G. Rong, J.J. Saarinen and J.E. Sipe, "High sensitivity sensor based on porous silicon waveguide," *Materials Research Society Symposium - Proceedings*, vol. 934, 2006.
- [57] P. Pirasteh, J. Charrier and A.Soltani, "The effect of oxidation on physical properties of porous silicon layers for optical applications," *Applied Surface Science*, vol. 253, pp. 1999-2002, 2006.

- [58] R. Cisneros, C. Ramirez and C.Wang, "Ellipsometry and ab initio approaches to the refractive index of porous silicon," *Journal of Physics: Condensed Matter*, vol. 19, pp. 395010, 2007.
- [59] M. Gaillet, M. Guendouz and M.B. Salah, "Characterisation of porous silicon composite material by spectroscopic ellipsometry," *Thin Solid Films*, vol. 455-456, pp. 410-416, 2004.
- [60] J. Zheng, "Porous silicon technology for integrated microsystems," PhD dissertation, Electrical and Computer Engineering Department, MTU, Houghton, MI, 2006.
- [61] K. Barla, R. Herino, and G. Bomchil, "Stress in oxidized porous silicon layers," *Journal of Applied Physics*, vol.59, pp. 439, 1986.
- [62] E. Konjhodzic, H. Bretinger and U.Wilczok, "Low-n mesoporous silica films: structureand properties," *Journal of Applied Physics (A)*, vol. 81, pp. 425-432, 2005.
- [63] J. Charrier, V. Alaiwan and P.Pirasteh, "Influence of experimental parameters on physical properties of porous silicon and oxidized porous silicon layers," *Applied Surface Science*, vol. 253, pp. 8632-8636, 2007.
- [64] A. Hakonen and S. Hulth, "A high-precision ratiometric fluorosensor for pH: Implementing time-dependent non-linear calibration protocols for drift compensation," *Analytica Chimica Acta*, vol. 606, pp. 63-71, 2008.

- [65] S. Flink and F.C. Van Veggel, "Functionalization of self-assembled monolayers on glass and oxidized silicon wafers by surface reactions," *Journal of Physical Organic Chemistry*, vol. 14, no. 7, pp. 407-415, 2001.
- [66] C.R. French, J.J. Carr and M.D. Degrandpre, "Spectrophotometric pH measurements of freshwater," *Analytica Chimica Acta*, vol. 453, pp. 13-20, 2002.
- [67] J. Janata, "Do optical sensors really measure pH," *Analytical Chemistry*, vol. 59, pp. 1351-1356, 1987.
- [68] S.W. Smith, M. McGuire, D. Price, D. Allman, K.L. Vanga, P.L. Bergstrom, and J.F. Conley, unpublished work, Electrical Engineering and Computer Science, and Materials Science, Oregon State University, 3089 Kelley Engineering Center, Corvallis, OR 97331-5501.
- [69] A.I. Boukai, Y. Bunimovich and J.Tahir-kheli, "Silicon nanowires as efficient thermoelectric materials," *Nature*, vol. 451, pp. 168-171, 2008.
- [70] L. Hu and G. Chen, "Analysis of Optical Absorption in Silicon Nanowire Arrays for Photovoltaic Applications," *Nano Letters*, vol. 7, no. 11, pp. 3249-3252, 2007.
- [71] Z. Li, B. Rajendran and T.I. Kamins, "Silicon nanowires for sequence-specific DNA sensing: device fabrication and simulation," *Applied Physics A: Materials Science & Processing*, vol. A80, no. 6, pp. 1257-1263, 2005.

- [72] R.L. Smith and S.D. Collins, "Porous silicon formation mechanisms," *Journal of Applied Physics*, vol. 71, pp. R1-R22, 1992.
- [73] E.A. Ponomarev and L.C. Clement, "Macropore Formation on p-Type Silicon," *Journal of Porous Materials*, vol. 7, no. 1-3, pp. 51-56, Jan. 2000.
- [74] S. Tanaka, S. Fujimoto and O.Ito, "Laterally stacked glass substrates with high density electrical feedthroughs," *Journal of Micromechanics and Microengineering*, vol. 17, pp. 597-602, 2007.
- [75] R.L. Smith and S.D. Collins, "Porous silicon formation mechanisms," *Journal of Applied Physics*, vol. 71, pp. R1-R22, 1992.
- [76] A. Satoh, "Formation of Through-Holes on Silicon Wafer by Optical Excitation Electropolishing Method," *Japanese Journal of Applied Physics*, vol. 39, pp. 378-386, 2000.
- [77] Y. Tao and M. Esashi, *J. Micromechanical and Microengineering*, vol. 14, pp. 1411-1415, 2004.
- [78] K. Grigoros, S. Franssila and T.Sikunen, *Phys. Stat.sol. (a)*, vol. 202, p. 1402, 2005.
- [79] M. Christophersen, P. Merz, and H.Foll, "A new method of silicon microstructuring with electrochemical etching," *Physica Status Solidi (a)*, vol. 182, pp. 561, 2000.

- [80] V. Lehmann and H. Foll, "Formation Mechanism and Properties of Electrochemically Etched Trenches in n-Type Silicon," *Journal of Electrochemical Society*, vol. 137, no. 2, pp. 653-659, 1990.
- [81] C. Akinobu, "Mechanism and Characteristics of Through-hole Formation on Si Wafer by Optical Excitation Electropolishing Method," *Japanese Journal of Applied Physics*, vol. 39, pp. 1612-1621, 2000.
- [82] Y.J. Zhang, W. Li and K.J. Chen, "Application of two-dimensional polystyrene arrays in the fabrication of ordered silicon pillars," *Journal of Alloys and Compounds*, vol. 450, pp. 512-516, 2008.

Publications And Conference Proceedings

1. Kumar Vanga, Qili Hu, Sarah Green, and Paul Bergstrom, “Implementation of Porous Silicon Technology for Flow-Through Sensing Using Electro-Osmotic Phenomenon”, Paper ThPoT9.13 IEEE-NANO, Portland, OR 2011, citation waiting.
2. Kumar Vanga, Dawdon Cheam, Christopher Middlebrook, and Paul Bergstrom, “Optical properties of thick, ordered mesoporous silica membranes”, *Physica Status Solidi C* 8, No. 6, 1941-1945 (2011), Presented at the Porous Semiconductor-Science and Technology Conference, Valencia, Spain 2010.
3. Kumar L. Vanga, Karumbaiah N. Chappanda and Paul L. Bergstrom, “Electro-Osmotic Pump Based on Thick Oriented Mesoporous Silicon Membranes for High Flow-rates and Pressure Capacities” - Draft under review, Presented at the Porous Semiconductor- Science and Technology Conference, Valencia, Spain 2010.
4. R. Tewari, K. L. Vanga, W. Knudsen, C. Friedrich, “Process Characterization: Reactive Ion Etching of Micro Hot-Embossed Poly (Lactic Acid) Films”, *Biomedical Engineering Society*, Austin, TX 2010.
5. L. K. Vanga, M. K. Oisten, T. Ritzdorf, and P. L. Bergstrom, “Electric Field Effects on the Formation of Isolated Macro Porous Silicon”, *Electrochemical Society Transaction* 16 (3), 143, Honolulu, HI 2008.

Appendix A

Porous Silicon Fabrication

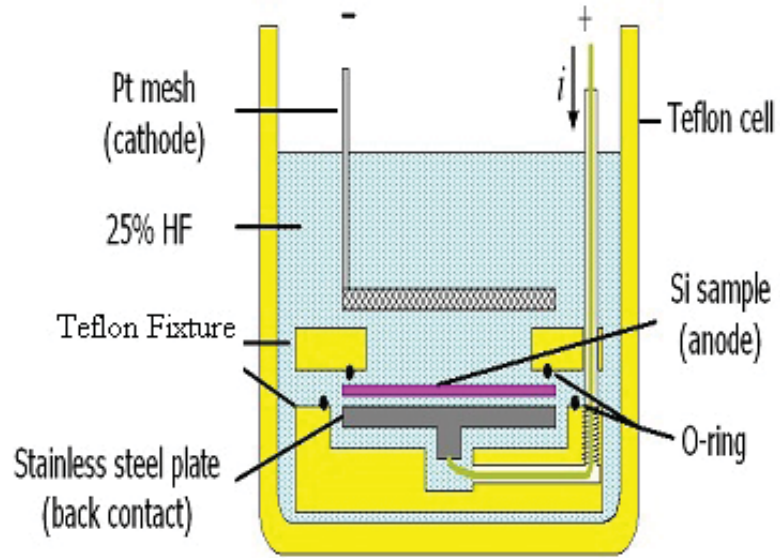
A.1 Introduction

This appendix outlines some of the fabrication processes and mechanisms utilized in the formation of porous silicon structures. Macroporous silicon which is one of the most common forms of porous silicon, is explored for *p*-type (100) silicon substrates using electrochemical anodization technique. Over the years, significant background research has built an understanding of the many aspects of the formation of porous semiconductors. These studies include understanding the effects on the pore formation by varying parameters like the applied current densities, crystal orientation, masking materials, electrolytic concentration and the impact of doping of the semiconductor substrate. In

addition, porous silicon's potential is attributed to its tunable refractive index, ability to engineer regular trenches, high oxidation rate, low thermal conductivity, and its high dissolution rate in anisotropic etchants like KOH and TMAH thereby still preserving the crystalline nature of silicon. A detailed explanation of the formation of porous silicon is listed elsewhere [72].

A.1.1 Electrochemical Anodization Setup

Galvanostatic setup was employed for all the electrochemical etch experiments conducted for the fabrication of porous silicon. In this work, A Keithley 2400 source-meter is utilized to anodically bias the substrate with respect to the electrolyte solution. In general, constant current is preferred as it allows better control of both the porosity, thickness uniformity of the porous region, and a good reproducibility. The electrochemical anodization configuration is shown in Fig. A.1 (a). As shown in Fig. A.1 (a), the single cell anodization involves a metal contact to the backside of the sample and is sealed by a O-ring such that the electrolyte interacts with the sample only from the front side. A top mesh electrode (Pt) acts as the cathode. The electrochemical fixture is shown in Fig. A.1 (b). A peristaltic pump is utilized for the electrolyte circulation, thereby maintaining the uniformity of the chemical species in the solution. The porous silicon uniformity can vary depending on the substrate doping and is more critical in case of highly resistive substrates which require backside metallic contact.



(a)



(b)

Figure A.1: (a) schematic of the electrochemical anodization setup, (b) electrochemical etching fixture utilized for the fabrication of porous silicon [60]. [Permission in Appendix].

A.1.2 Macroporous Silicon - *p* (100) Substrates

In general, porous silicon is formed on various silicon substrate types, which include *p*-type, p^+ , *n*, and n^+ with crystalline orientations primarily in (100) and (111) substrates. For the fabrication of porous media for the electro-osmotic pump, *p* type (100) samples with resistivities of 10 - 20 Ω cm and 20 - 30 Ω cm were electrochemically anodized in an electrolytic solution consisting of 1:2:3 ratio of 49% HF, ethyl alcohol, and DI (deionized) water. In order to reduce surface tension and viscosity associated with the electrolyte, Cetyltrimethylammonium chloride (CTAC) at 10^{-3} M is added to the solution.

Well-ordered arrays of pores on silicon are fabricated by using a multistage process flow, which include, thin film deposition of masking layers, lithographic patterning of defined arrays, anisotropic etching of silicon, reactive ion etching and electrochemical anodization. In order to improve the backside electrical contact between the silicon sample and metal electrode, wafers are first implanted on the backside (unpolished surface) with boron atoms. After the implantation, a backside drive-in of the dopants is performed using a thermal annealing step. Table A.1 shows the implantation specifications for silicon substrates.

In the case of *p*-type silicon substrates that are utilized for the fabrication of highly vertical and uniform pores, lithographically patterned and chemically etched pore

Table A.1
Boron dopant implantation conditions for improving backside silicon conductivity- Porous silicon formation.

Species	Boron
Isotope (mass)	-
Wafer Size (state mm or inch)	4 inch
Substrate Material	Silicon
Dose (ions/cm ²)	1.00 E ⁺¹⁵
Energy (keV)	80
Tilt Angle (degree)	7
Photo Resist	NO

initiation sites are preferred and often necessary. These pore initiation sites are typically the inverted pyramidal pits with sharp tips associated with anisotropic etching of silicon in a suitable etchant such as potassium hydroxide (KOH). Figure A.2 shows the detailed process flow considered for the fabrication of porous silicon earlier developed in Dr. Bergstrom's group at MTU and has been modified and further developed in this work. Some of the modifications include, design of new masks for lithographic pattern transfer to substrates, metal masks in addition to dielectric masking materials and new etch recipes are considered.

In order to selectively fabricate porous silicon in desired regions on the substrate, dielectric or metal masks are usually necessary. One of the key steps involved in the fabrication of porous silicon by electrochemical etching is depositing the three primary masking layers silicon dioxide (SiO₂), poly silicon (poly-Si), and silicon nitride (Si₃N₄) on the mirror polished surface (front side) as shown in the Fig. A.3 (a). After depositing the masking layers, the wafer will go through a rapid thermal annealing (RTA) step to relieve

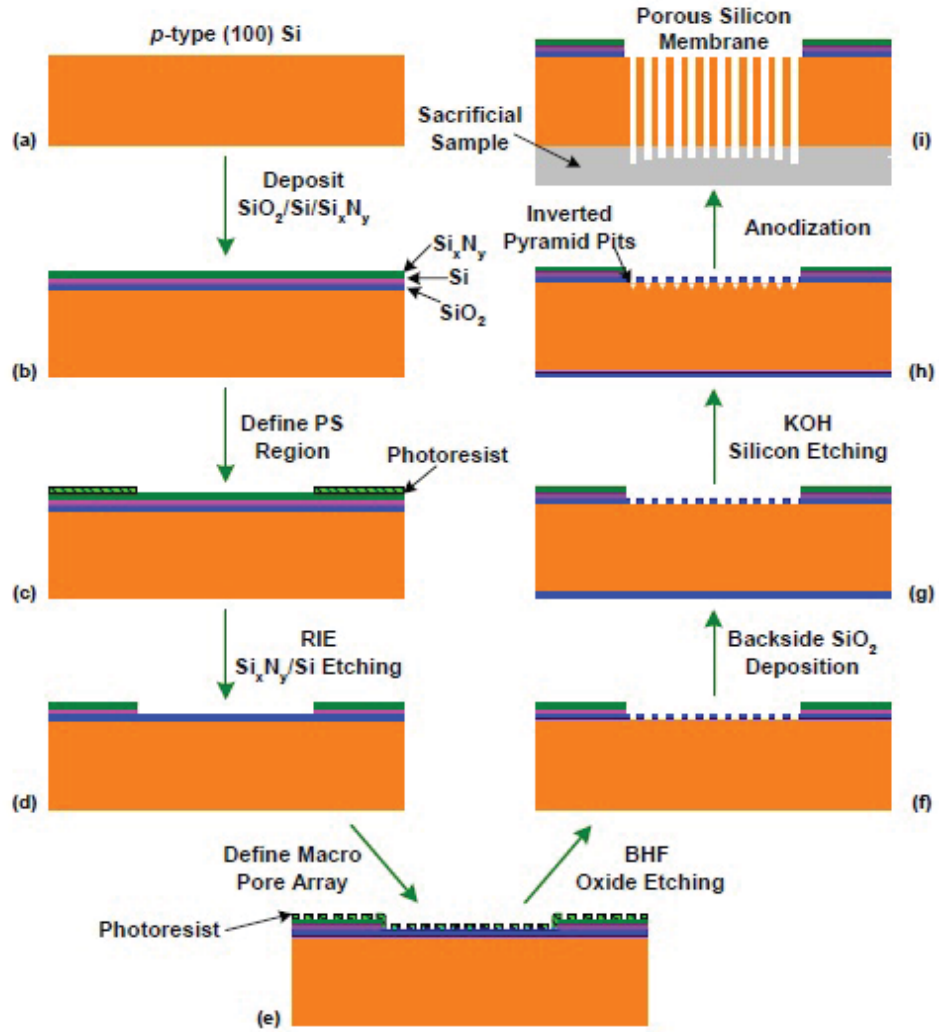


Figure A.2: Process flow for the fabrication of macroporous silicon: (a) *p*-type (100) silicon substrate with resistivity of 10 - 20 Ω cm or 17 - 23 Ω cm, (b) masking stack of $\text{SiO}_2/\text{Si}/\text{Si}_3\text{N}_4$ layers deposited using RF sputtering, (c) lithographically defined 3.5 mm circular opening for porous silicon formation, (d) transfer of the porous silicon region pattern onto the $\text{Si}/\text{Si}_3\text{N}_4$ layers by RIE, (e) 2 μm array is patterned on SiO_2 using lithography, (f) transfer the macro pore array pattern into the oxide layer by BHF etching or by RIE, (g) deposition of SiO_2 on the backside of the sample as mask isolation, (h) formation of inverted pyramidal pits by KOH etching, (i) formation of macroporous silicon membrane by anodizing with sacrificial sample [60]. [Permission in Appendix].

any stress present in the masking layers. In general, deposited films will have either tensile or compressive stress depending on the material.

In this study, we have investigated the formation of porous silicon in features with sizes ranging from 3 - 5 μm in a 3.5 mm diameter regions using chromium (Cr)/gold (Au) and Si_3N_4 masking layers by selectively forming porous silicon on the substrates.

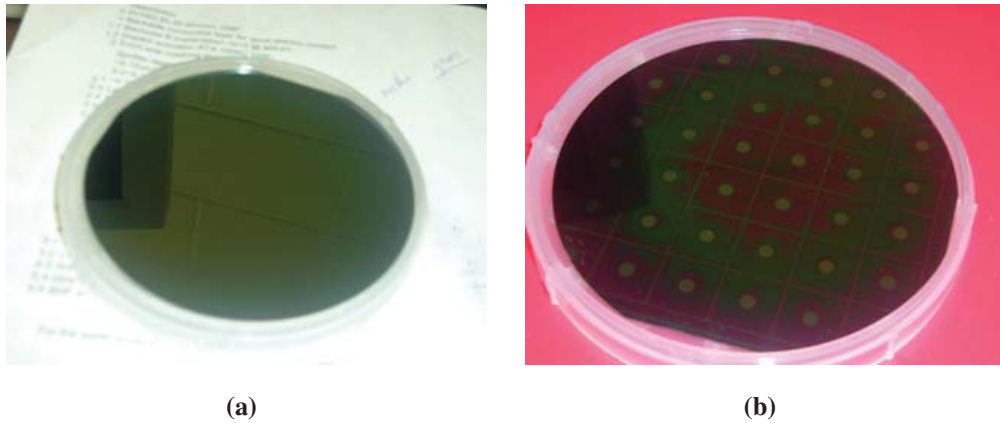


Figure A.3: (a) RF-sputter deposited mask stack on a *p*-type silicon substrate. Dielectric layers including, SiO_2 , poly-si and Si_3N_4 are the standard layers that are considered, and (b) photolithography is used to define 3.5 mm circular regions on the mask stack to selectively form porous silicon.

A.1.3 Photoresist Spinning

The spinning of photoresist is performed on a programmable spinner (Model WS-650MZ-23NPP/LITE). Depending on the desired feature size to be patterned on the

substrate, a specific photoresist is chosen. The thickness of the photoresist can be controlled to a certain extent by selecting a specific rotational speed on the spinner. Typical rotational speeds used are between 2000 - 3000 r.p.m. (rotations per minute) For selectively anodizing a pattern (3.5 mm region to be anodized on the silicon substrate with deposited masking layers) as shown in Fig. A.3 (b), the following steps are required.

The substrate is first rinsed in the spinner with IPA (isopropyl alcohol) to remove any dust or particles present on the substrate's surface. A prebake step is performed usually for 5 minutes on a hot plate at 105 °C to remove any moisture or solvents present on the substrate's surface. Next, a thin layer of adhesive HMDS (hexamethyl disilazane) is applied on the substrate. HMDS is an adhesion promoter between the photoresist and substrate, it reacts with the oxide surface present on the surface of silicon wafer forming a strong bond. Positive photoresist, Shipley 1817, is spun at 3000 R.P.M on the spinner for a minute followed by a soft bake. The photoresist spinner utilized is shown in Fig. A.4.

A.1.4 RF-Sputtering: Mask Deposition

An RF sputtering system similar to the one shown in Fig. A.5 is used for the thin film deposition. In general, a radio-frequency (RF) voltage is applied between the anode and cathode electrodes that causes the free electrons to collide and excite the the gas molecules present in the chamber resulting in the ionization of the gas resulting in anions, cations, and



Figure A.4: PR spinner utilized for coating the substrates before photolithographic process.

neutral species. Argon (Ar) is employed as the working gas for all the thin film depositions. During sputtering, the positive Ar ions (cations) that are created are accelerated towards the cathode, thereby causing the removal of the target atoms. The cathode usually the working electrode of material will be deposited onto the substrate, the substrate being placed on the anode. Relatively high vacuum (10^{-7} torr) is required to achieve high quality films with minimal defects and good adhesion to substrates. The masking layers or stack ($\text{SiO}_2/\text{poly}/\text{Si}_3\text{N}_4$) deposited on silicon have thicknesses of $0.12\ \mu\text{m}$ of SiO_2 , $0.2\text{-}0.3\ \mu\text{m}$ of poly-silicon and $0.15\ \mu\text{m}$ of Si_3N_4 .



Figure A.5: Perkin Elmer RF sputtering system employed for depositing various masking materials including metals and dielectrics.

A.1.5 Photolithography

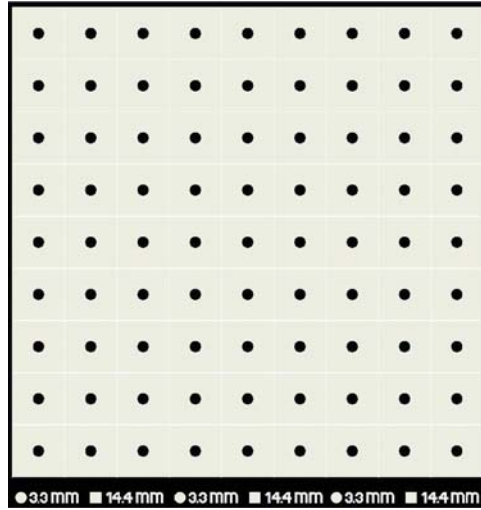
Using photolithography, an array of 3.5 mm openings is patterned on the mirror-polished surface as shown in Fig. A.3 (b). Photolithography has been one of the key reasons for the development of IC technology and further miniaturization of electronic devices. Resolution of the features and transfer of pattern is dependent on the wavelength of lamp source. In general, an UV (350 - 450 nm) lamp source is used to project the pattern on a optically flat silica/Quartz glass photo-mask to a substrate that is coated with a thin layer of light sensitive material known as photoresist. The photoresist that is used for creating the 3.5

mm openings is Shipley 1827. UV exposure is performed for 10-12 seconds at 17 W/cm^2 (check again) and is developed in the MF319 solution for ~ 5 minutes. The two primary types of masks, dark field and bright field masks similar to the ones shown in Fig. A.7 (a) and Fig. A.7 (b) are considered for creating the 3.5 mm openings.

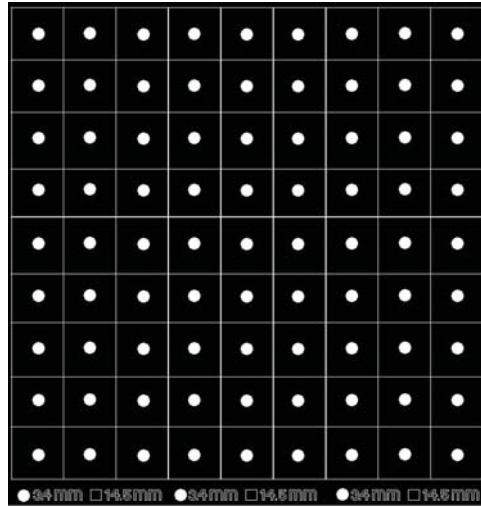
It is very important to ensure that all the photoresist is developed and no photoresist residue is left in the circular opening on the substrate. Photoresist residue in the mask opening will prevent any dry etching in the subsequent processing.



Figure A.6: EVG 620 photolithographic aligner utilized for pattern transfer through UV exposure.



(a)



(b)

Figure A.7: (a) dark field mask- shows the circular pattern with ~ 14.5 mm unit cell on a 4 inch mask pattern, (b) bright field mask- shows the circular pattern with ~ 14.5 mm unit cell on a 4 inch mask pattern designed using Cadence.

After transferring the 3.5 mm pattern to the substrate, a RIE step is performed to etch through the Si_3N_4 and poly-silicon films using photoresist as a mask. Photoresist is

Table A.2
Experimental conditions for the 2 μm pattern transfer.

Process Step	Parameter
Prebake	140 °C, 2-3 min
Spin Resist	3000 r.p.m
Soft bake	120 °C for 1 min
Lithography exposure (UV)	7 sec, hard contact
Develop	15-20 Sec
Hard bake	120 °C for 1 min

stripped and the wafer is cleaned in a piranha solution (a mixture of $\text{H}_2\text{O}_2 + \text{H}_2\text{SO}_4$) at 120 °C to remove any organic residues. To realize an array of pores, lithographic step is used to transfer a 2-micron array to the wafer. Since the features are in the μm range, positive photoresist, Futurrex is used for this step and is developed in RD6. The array as shown in Fig. A.8 (a) and Fig. A.8 (b) is patterned over the wafer (both the 3.5 mm opening and the outside regions). The parameters as shown in Table A.2 are considered for the UV exposure.

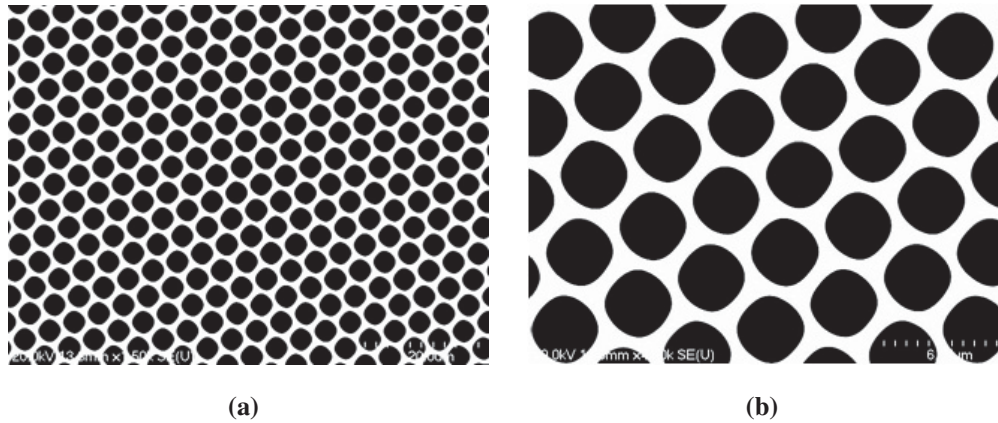


Figure A.8: (a) photolithographic pattern of 2 μm array used for the fabrication of porous silicon, (b) FE-SEM image of photolithographic pattern of 2 μm array on photoresist at high magnification.

After patterning the 2- μm array, the next process step involved is to etch through the 2-micron array on the SiO_2 layer in the 3.5 mm opening. This is a critical step as this etch through the oxide will dictate if the array of pyramidal pits will be formed in the 3.5 mm opening. Any thin layer of photoresist left in the openings that is not developed will act as a mask and prevents further dry or wet etching of the oxide.

A.1.6 Reactive Ion Etching

After the lithography step, the next process involves transferring the pattern on the photoresist onto the substrate. This is achieved through dry etching or wet etching. Dry etching, usually the reactive ion etching is considered due to the ease of handling and the anisotropy of the profile achieved. Also, issues related to disposal of the chemical that is involved in wet etch techniques is minimized in the case of dry etching. Also factors like viscosity and surface tension are reduced in the case of dry etching when compared to wet etchants which can prevent removal of material in small features. The important requirement for both wet etching and dry etching includes faithfully reproducing the patterns on the mask without distorting the features. Under etching, over etching, and distortion are some of the common problems associated with these etching techniques. In the case of ion etching, ions are accelerated towards the target (substrate) and physically bombard the substrate, thereby removing the material. This physical etch has some advantages as the etch doesn't result in any volatile products. This may result in slower

etch rates, hence a more reactive ion etching is desirable where there are two components, one pertaining to physical and the other to reactivity of the the gases that are used.

Reactive ion etching involves treating the sample in a plasma environment where reactive gases interact with the substrate both physically and chemically to remove material. Selective gases are chosen depending upon their reactivity and removal rate of the material under study. Typical gases that are considered in the silicon micro-fabrication processes involve fluorine or chlorine components that react with the substrate material. The reactive components or species of the gases are formed from the interaction of the gas molecules with the free electrons present in the plasma environment. In our study, typical gases that are employed include, SF_6 , CF_4 , O_2 , and Ar etc.

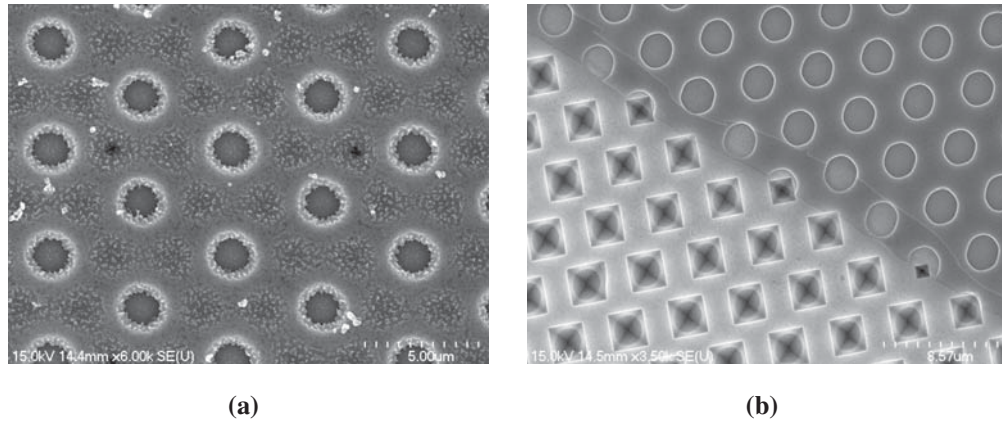


Figure A.9: a) FE-SEM etch pattern in the 2 μm array formed using Trion RIE/ICP, (b) etch boundary with inverted pyramidal pits where the outside region is selectively masked.

Figure A.9 (a) shows the FE-SEM image of the etch pattern in the 2 μm array formed using Trion RIE-ICP. Figure A.9 (b) shows the etch boundary with inverted

pyramidal pits where porous silicon is formed with outside region selectively masked.

A.1.7 Inverted Pyramidal Pits: Nucleation Sites

In addition to dry etching techniques, wet etching or wet bulk micromaching is also an important technique in realizing features in substrates. Exposing areas selectively thereby removing material with wet etchants is an efficient technique. Depending on the etchant as well as the crystallographic properties of the material to be etched, interesting patterns can be designed and fabricated. Appropriate masking materials or etch stops are utilized during the wet etching process. In general, a well characterized etch study pertaining to the etching of crystal planes is performed in understanding the etch effects and determining the etch rates. Usually, selective etchants like potassium hydroxide (KOH) that attacks the (100) planes much faster than (111) is considered in achieving inverted pyramidal pits. These (100) planes with more dangling bonds etch faster as the silicon atoms are more weakly bound to the rest of the lattice. Based on this, the etch rates of the three primary planes follow $(111) \ll (110) < (100)$ trend. FESEM images of pore initiation sites or the inverted pyramidal pits in *p* (100) silicon are shown in Fig. A.10. Figure A.10 (a) shows pyramidal pits on a 20-30 Ω -cm substrates, Fig. A.10 (b) shows pyramidal pits on a 10-20 Ω -cm substrate, Fig. A.10 (c) shows incomplete pyramidal pit at high magnification, Fig. A.10 (d) shows poor pyramidal formation due to mask failure, Fig. A.10 (e) shows a cross-sectional view of inverted pyramidal pits, and Fig. A.10 (f) shows half etched KOH

pits on a *p*-type (100) silicon substrate.

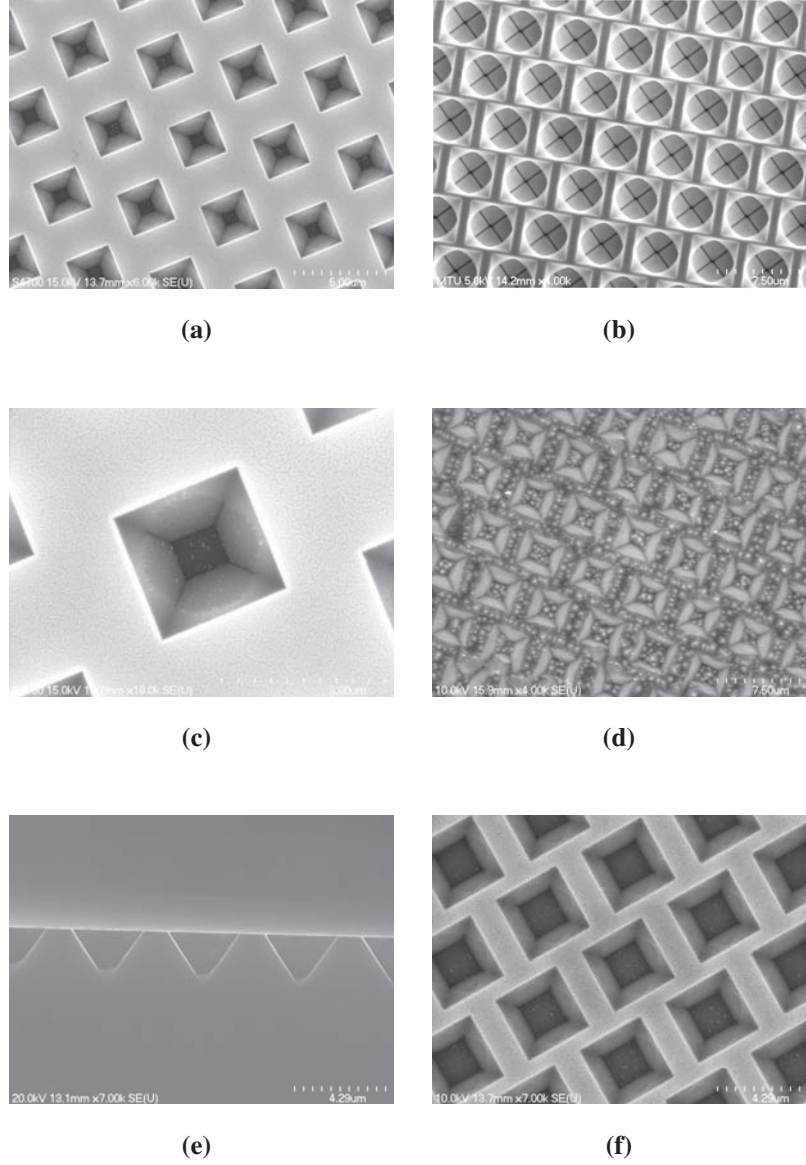


Figure A.10: (a) pyramidal pits on a 20-30 Ω -cm substrates, (b) pyramidal pits on a 10-20 Ω -cm substrate, (c) incomplete pyramidal pit at high magnification, (d) poor pyramidal formation due to mask failure, (e) cross-sectional view of inverted pyramidal pit, and (f) half etched KOH pits.

Figure A.11 (a) shows the setup used for performing anisotropic etching of silicon

for the formation of inverted pyramidal pits. The samples are placed in bath of KOH solution at 72 °C. Figure A.11 (b) shows a sample with mask peeling which was observed in the case of dielectric masks.

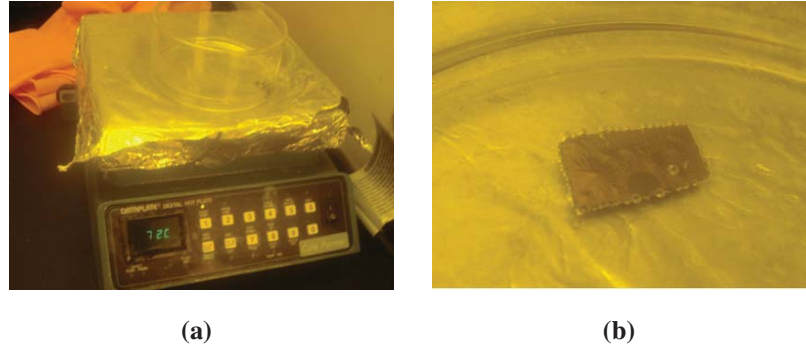


Figure A.11: (a) setup utilized to perform anisotropic etching of silicon to realize inverted pyramidal pits in a KOH bath, and (b) mask peeling observed in the case of dielectric mask.

A.2 Introduction to Porous Silicon

In the 1990's, Canham showed that certain porous silicon based materials can have large photoluminescence efficiency at room temperature in the visible region, a surprising result since the photoluminescence of bulk silicon is very low due to its indirect band gap and short radiative life time of charges [20]. Porous silicon has been of great interest because of its demonstrated application in sensing, photonic systems, and as an enabling technology for micro-machining [73]. Various techniques have been implemented in the past to achieve high aspect ratio pores (vias) with small diameters while maintaining a high aspect

ratio. Some of these techniques include deep reactive ion etching (DRIE), laser Machining and electro-discharge machining (EDM). However, these techniques are limited by sidewall scalloping, low aspect ratios, machining tailing or reaction byproducts, and micro cracks [74]. A detailed explanation of the formation of porous silicon is outlined elsewhere [75]. Porous silicon is classified according to the pore diameter, which can vary from a few nanometers to few microns depending on the formation parameters. In general there are three regimes for porous silicon which they can be classified as micro porous (few nm), mesoporous (tens of nm), macroporous (μm).

A.2.1 Porous silicon: Applied Current Density

Figure A.12 shows cross-sectional view of porous silicon formation at different current densities (Fig. A.12 (a) at 35 mA/cm^2 , Fig. A.12 (b) at 40 mA/cm^2 , Fig. A.12 (c) at 45 mA/cm^2 , and Fig. A.12 at (d) 50 mA/cm^2). The uniformity and sidewall profile improves with an increase in current density to a threshold, beyond which electro polishing takes place.

Selective electrochemical anodization of silicon for the formation of porous silicon is performed using masking materials like dielectric, metal, and doped or implanted substrates [74], [76], [77]. Insulating materials like silicon dioxide and silicon nitride are common masking materials for anodization [46], [78], [79]. Dielectric masking materials

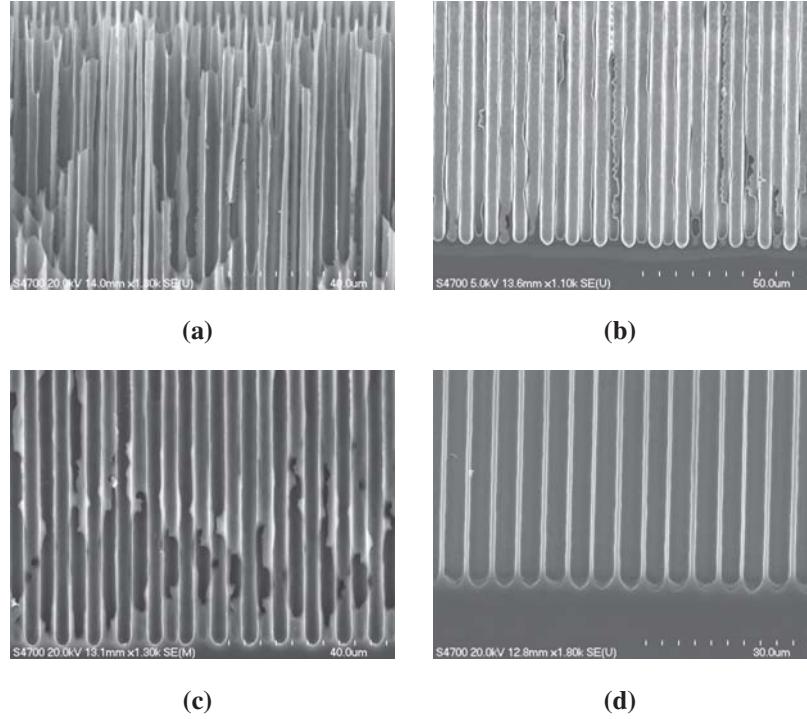


Figure A.12: Cross-sectional SEM view of macroporous silicon electrochemically anodized at current densities (a) 35 mA/cm², (b) 40 mA/cm², (c) 45 mA/cm², and (d) 50 mA/cm².

suffer from current crowding effect thereby resulting in a non-uniform porous region near the mask edge. Metallic masking materials have been recently explored to determine their impact in porous silicon anodization as they seem to have better control of electric field near and through the mask. Pore growth is controlled in part by the direction of the hole current in the substrate. The formation of uniform pores along the $\langle 100 \rangle$ direction occurs when positive holes accumulate at the tip of the inverted pyramidal pit due to the reduced radius of curvature, resulting in the decrease of the space charge region (SCR), hence allowing a larger hole current to flow, contributing to the pore propagation. The dimension of this tip must be significantly smaller than the surface roughness of walls of the pit to achieve the

geometrical field enhancement at the tip [80], [81]. With a dielectric masking material, the total current in the substrate is constrained by the opening of the feature area that is exposed to the electrolyte and results in a higher current density at the edge of the feature compared to center of the feature opening [78]. This current crowding effect results in undesirable pores at the edge of opening with pore depths higher than the center of the feature opening. Silicon nitride masking has the advantage that it is highly resistant to liquid HF etching compared to a gold mask. Sputter deposited gold is prone to pin hole defects that will cause undesired pore formation in the masked areas and will result in mask peeling during the electrochemical anodization experiment.

A.2.2 Thermal Oxidation

Thermal oxidation of both macroporous silicon and mesoporous silicon is performed using a 2 inch oxidation furnace as shown in Fig. A.13 (a) and Fig. A.13 (b). Macroporous silicon substrates are oxidized at 1000 °C to grow a thin thermal oxide on the pore walls to increase the strength of the porous membrane. Mesoporous silica samples are formed by the thermal oxidation of mesoporous silicon samples.

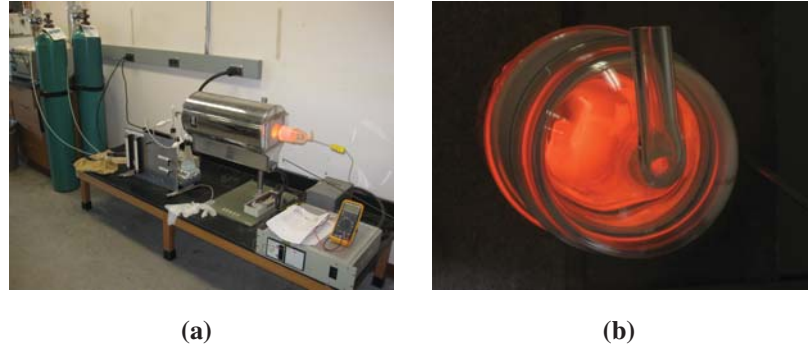


Figure A.13: (a) setup utilized for the thermal oxidation of porous silicon samples, (b) quartz tube furnace at 1000 °C.

A.2.3 Rapid Thermal Annealing

Annealing is a heat treatment technique that is widely used for altering the properties of deposited films. Commonly employed to retain the crystallinity of wafers after ion implantation, relieving stress in thin films and dopant activation. Compared to traditional annealing technique performed at a slow rate, RTA (rapid thermal annealing) is performed in a short duration, thereby altering the properties of a very thin layer or film and not necessarily altering the properties of the actual substrate. In conventional annealing, the heat treatment is slow with a low ramp rate. In our process, RTA was performed both for activating the dopants and also for relieving any stress present in the deposited films. Usually for RTA, the system is ramped to 1000 °C in a 30 second interval and then held at a steady state for 60 second period. The RTA furnace as shown in Fig. A.14 is purged with N₂ during the entire process. After the steady state step, the system is ramped to 100 °C in another 30 second period.



Figure A.14: Rapid thermal annealing system.

A.2.4 Through-Wafer Pores- Micro-polishing

Micro-polishing based on chemical mechanical polishing is utilized for polishing the porous silicon samples using Allied High Tech Products, Inc., CA (USA) at MTU. Polishing silicon wafers or porous silicon substrates is important for various applications including reducing the thickness of substrates, to create very smooth surfaces to reduce roughness, to open up pores from backside as in case of porous silicon. Applications related to gas diffusion in micro-channels such as fabricated from MEMS technology or a porous membrane require through pores.

As mentioned earlier, for certain applications its important to have a through-wafer porous silicon membrane. For the case of p (100) macroporous silicon, especially a sample

anodized with a dielectric mask results in a membrane that is not uniform as shown in Fig. A.15. These substrate require either a backside RIE or micropolishing step to open up the 3.5 mm porous region. Figure A.16 shows the setup and process involved in micro-polishing where Figure A.16 (a) shows porous silicon sample with polishing chuck, Fig. A.16 (b) shows porous silicon sample bonded to the chuck, placed on a hot plate, Figure A.16 (c) shows the Veeco micro polishing machine, and Figure A.16 (d) Sample polishing condition with water flowing.

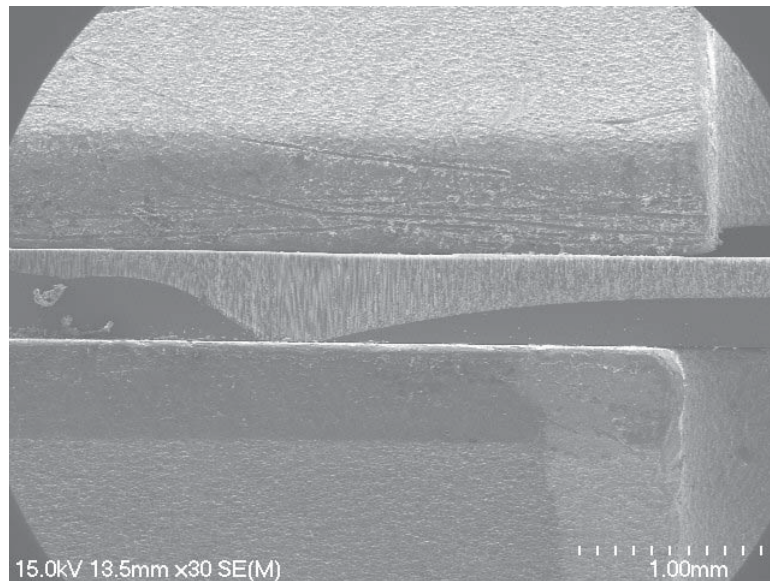


Figure A.15: Cross-sectional profile of macroporous silicon with current crowding effect seen using a dielectric mask stack (silicon nitride, silicon di-oxide and poly-silicon).

The 3.5 mm region on the back of the sample could also be exposed using RIE technique. This would require an additional lithography on the backside to create a 3.5 mm circular opening for material removal. Figure A.17 (a) and Fig. A.17 (b) show the pore profile of porous silicon formed from the backside etch using RIE. As the etch progresses,

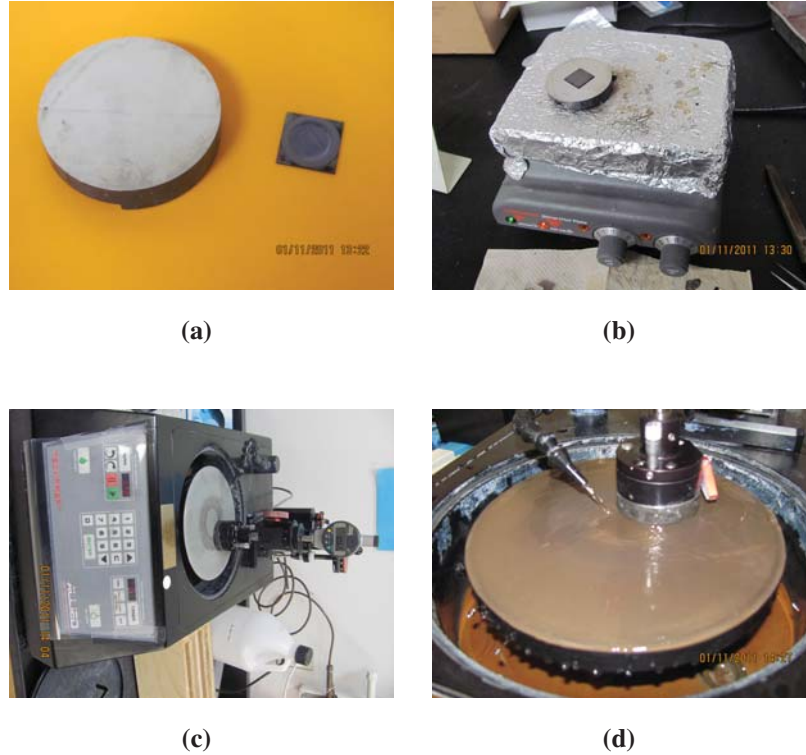


Figure A.16: (a) porous silicon sample with polishing chuck, (b) porous silicon sample bonded to the chuck, placed on a hot plate, (c) Veeco micro polishing machine, and (d) sample polishing condition with water flowing.

a dark circular pattern on the edge is exposed first due to the fact that the pores at edge of the 3.5 mm porous region are deeper than the ones at the center.

A.2.5 Lift-Off: Cr-Au Mask

This experiment was performed on a *p*-type (100) 10 - 20 Ω -cm sample and is utilized as an alternative to wet etching process. A 2 μ m array was patterned lithographically in the 3.5 mm region using the new (3.5 mm, 2 μ m array mask). Negative photoresist Microchem

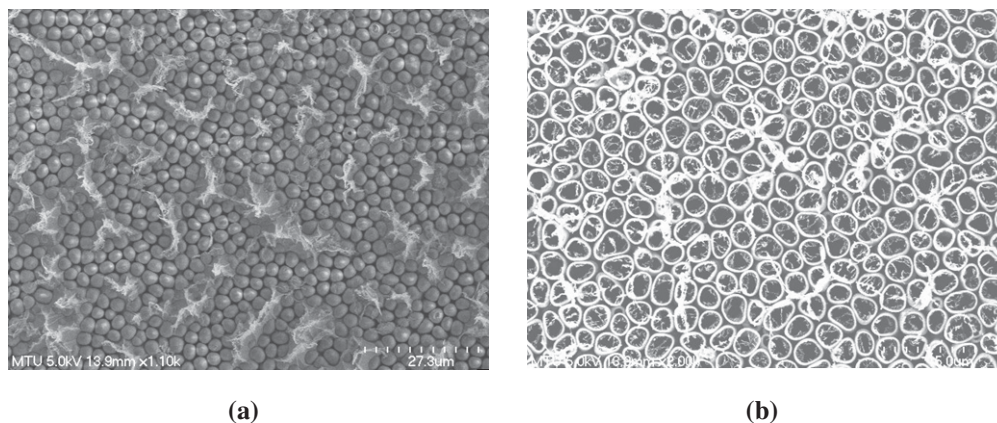


Figure A.17: (a) FESEM images of backside of the porous silicon membrane without pore openings after micro-polishing, and (b) with pore opening.

NR9G 1000PY was used. A 15 nm Cr and 50 nm Au is sputtered on this array. Lift-Off is then performed using acetone in an ultrasonic bath. Inverted pyramidal pits are then formed on this template using KOH solution. The detailed process for lift-off and wet etching utilized for the formation of 2- μ m array using metal mask (Cr-Au) is shown in Fig. A.18 and the process sequence is listed below.

1. The starting material is a 4" *p* – type(100) silicon substrate.
2. A photoresist is spun on the substrate typically at 2000 RPM.
3. The photolithography step, UV light is exposed through the desired mask.
4. The substrate is next developed in developer MF319 or RD6.
5. Metal deposition of Cr and Au films using sputtering or e-beam deposition. Metal is deposited all over including on photoresist.

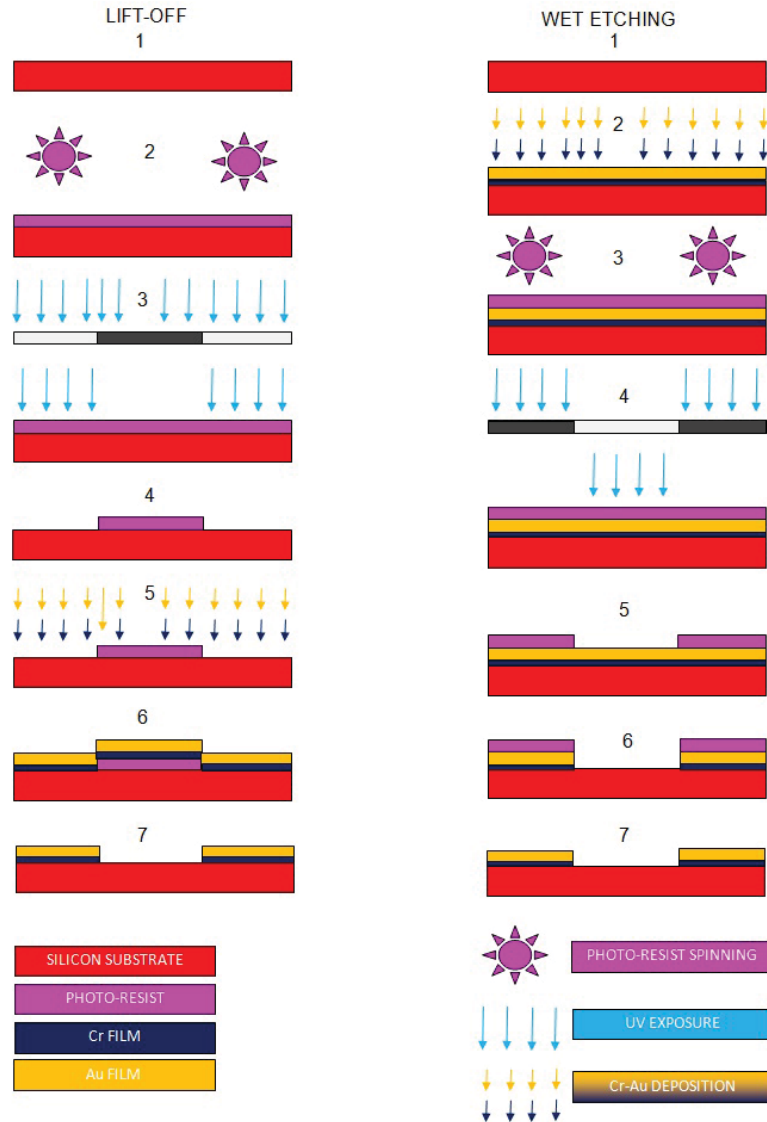


Figure A.18: A detailed process flow for lift-off technique and wet etching method utilized for the formation of inverted pyramidal pits on a metal mask.

6. Lift-Off is performed in an ultrasonic bath containing Acetone.

The process flow steps are listed below for Fig. A.18 using wet etching technique method.

1. The starting material is the substrate, a 4" silicon substrate is utilized in this work.
2. Metal deposition of Cr and Au films using sputtering or e-beam deposition.
3. A photoresist is spun on the substrate typically at 2000 RPM.
4. The photolithography step, UV light is exposed through the desired mask.
5. The substrate is next developed in developer MF319 or RD6.
6. Cr and Au are etched in Cr and Au etchants.
7. Photoresist is stripped using Acetone.

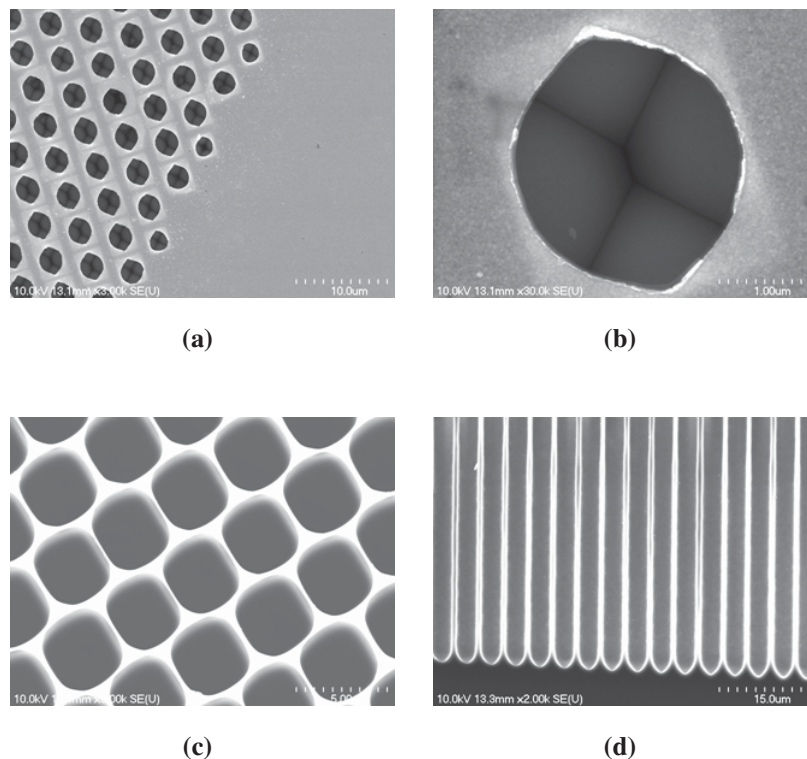


Figure A.19: (a) inverted pyramidal pore array with selective masking formed by metal lift-off and photolithography, (b) magnified image of a pyramidal pit, (c) top view of macroporous silicon array, and (d) cross-sectional view of porous silicon with a metal mask.

The metal mask, with Cr-Au layers (15 nm, 50 nm) had some defect formation during the ultrasonication, KOH etch, and after electrochemical etching. To get a good lift off on the 2 μm array with a Cr-Au mask (25 nm, 100 nm), a thicker photoresist was considered. Spin coating the resist twice will give a thicker resist film. Figure A.19 shows SEM images of macroporous silicon formed using a metal mask. Figure A.19 (a) shows the inverted pyramidal pore array with selective masking formed by metal lift-off and photolithography, Fig. A.19 (b) shows a magnified image of a pyramidal pit, Fig. A.19

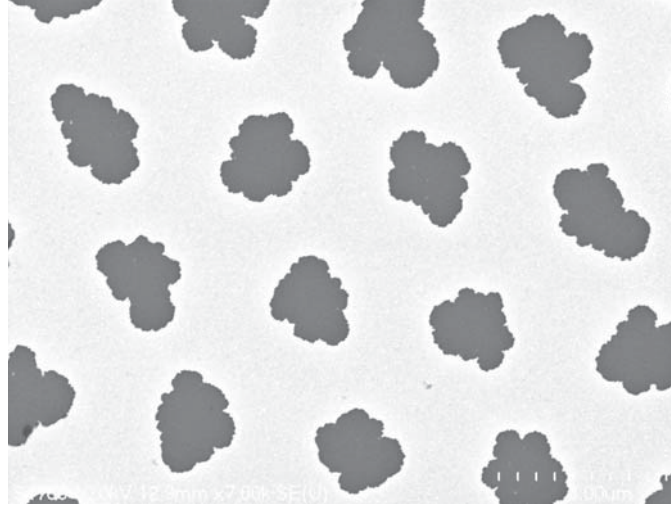


Figure A.20: 2 μm array of openings formed on Cr-Au mask using wet etching techniques for the formation of inverted pyramidal pits, the nucleation sites for the fabrication of porous silicon.

(c) shows a top view of macroporous silicon array, and Fig. A.19 (d) shows cross-sectional view of porous silicon with a metal mask.

Figure A.20 shows the top view SEM image of 2 μm array of openings on a metal mask formed using wet etching technique. The pattern of the openings is not as uniform when compared to a lift-off technique but can provide an alternate approach in realizing similar features.

A.3 Pore Size Control: Spherical Polystyrene Beads

From the previous section, inverted pyramidal pits are necessary to control the size of the porous silicon structures in a p type silicon. Also as observed, there is a limitation on the smallest pore that can be formed due to the constraints in photolithographic pattern transfer which is dictated by the wavelength of lamp source. Another interesting technique, also studied by Zhang et al. [82] involves depositing a monolayer of polystyrene nanosphere beads onto the silicon substrate using the self organization phenomena to form a very uniform layer as shown in Fig. A.21. Figure A.21 (a) shows SEM image of un-etched

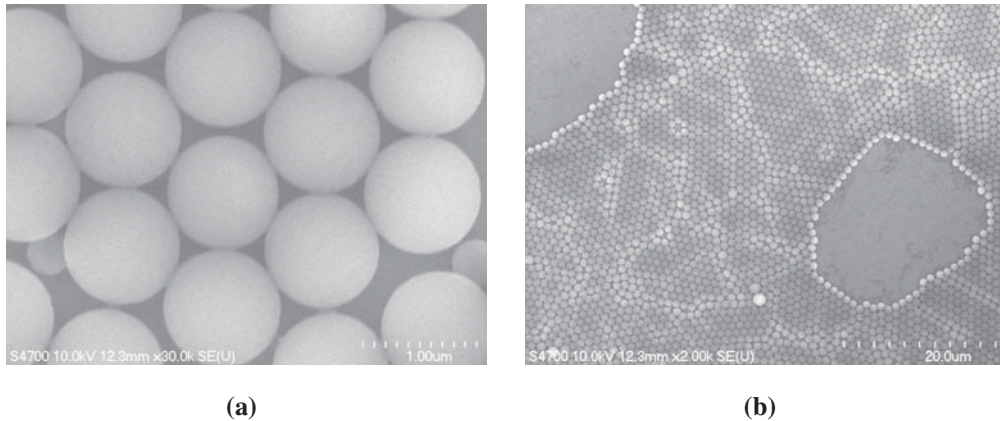


Figure A.21: (a) un-etched polystyrene beads at high magnification, (b) un-etched polystyrene beads at low magnification [Samples provided by Mr. Einar Haugan, the Institute for Energy Technology (IFE), Norway].

polystyrene beads at high magnification and Fig. A.21 (b) shows SEM image of un-etched polystyrene beads at low magnification. This polystyrene monolayer template has a potential to be used as a way to fabricate porous silicon with pores in 100's of nm which

has interesting applications in an electro-osmotic pump as discussed earlier. The initial size of the spherical polystyrene beads is $1\text{ }\mu\text{m}$. Using oxygen plasma, the size of the bead is reduced to much smaller dimensions as shown in Fig. A.22.

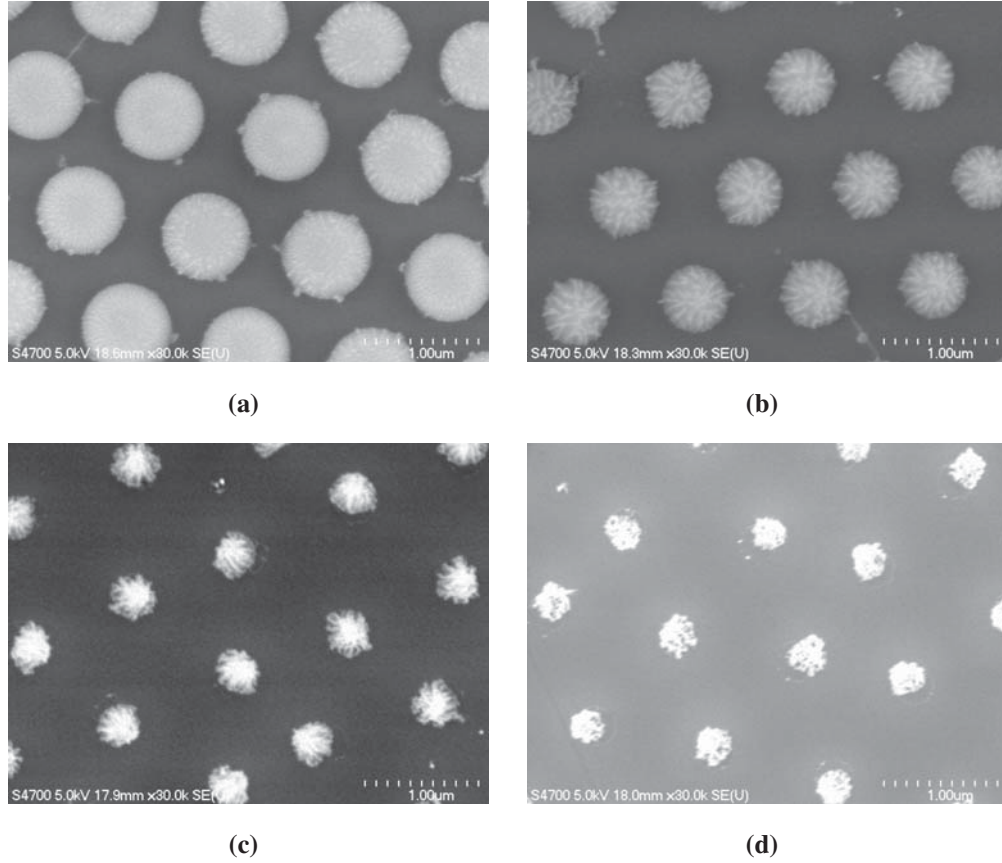


Figure A.22: March Jupiter etch pattern of polystyrene beads as a function of etch time in oxygen plasma. (a) one minute, (b) two minute, (c) three minute, and (d) four minute.

The following etch parameters are considered for controlling the diameters of the polystyrene beads, RIE: 100 W, O_2 : 50 SCCM, Pressure: 0.135 T. The measured etch rates are, for 1 min etch: BD (Bead Diameter) $\sim 820\text{ nm}$, 2 min etch: BD $\sim 630\text{ nm}$, 3 min etch:

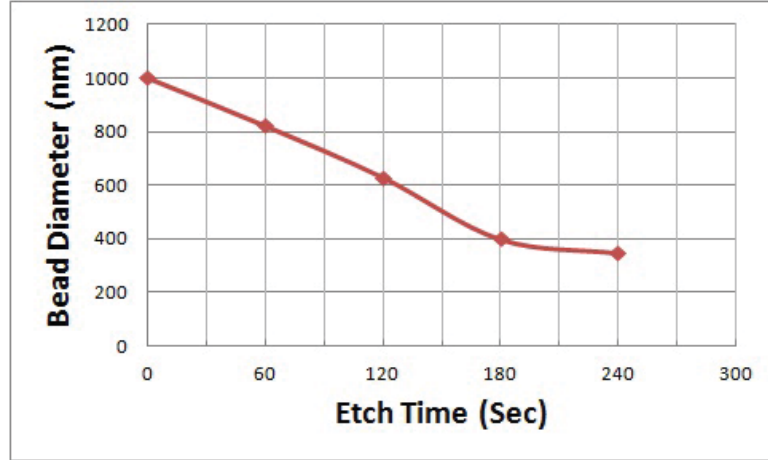


Figure A.23: Etch rate of polystyrene diameter as a function of etch time in oxygen plasma.

BD \sim 400 nm, 4 min etch: BD \sim 350 nm, and un-etched Beads: BD \sim 1000 nm. Plot in Fig. A.23 shows the reduction in bead size as a function of time in O_2 plasma. From the above data and plot, it is evident that the size of the polystyrene beads can be controlled to a great degree and has the potential to reduce the pore size of the porous silicon structures.

A.4 Summary

Various micro-fabrication processes that are implemented for the fabrication of porous silicon from *p*-type (100) silicon wafers are presented. Electrochemical anodization of silicon results in the formation of porous silicon. Porous silicon with highly vertical and uniform pores for EOP application is fabricated with pre-structuring silicon with inverted pyramidal pits. Other techniques including, thin film deposition, photolithography,

RIE and wet etching are presented. Effects of utilizing both dielectric and metal masks for anodization of silicon is studied. Other potential methods including using spherical polystyrene beads as template to create porous silicon structures in the 100's of nanometers is studied and some characterization involving reduction of size of polystyrene beads is performed.

Appendix B

Permission For Figures

Permission for figures in Chapter 1

Fig. 1.1

Dear Dr. Santiago, I am a doctoral student at MTU and would like to request permission to use Figure 15 from your journal in my PhD dissertation work. Citation- TOPICAL REVIEW, A review of micropumps, D J Laser and J G Santiago, J. Micromech. Microeng. 14 R35, Journal of Micromechanics and Microengineering Volume 14 Number 6, 2004. Kumar, Yes, you have my permission to use Fig 15 of Laser and Santiago review paper. Juan G. Santiago, Professor of Mechanical Engineering, Stanford University, Stanford, CA



Re: Permission to reproduce
Lakshman Kumar Vanga to: Permissions

25/04/2012 21:13

From: Lakshman Kumar Vanga <kumarvi@mtu.edu>
To: Permissions <permissions@iop.org>

Kumar L. Vanga

04/25/2012

Publishing Administrator,

Dear Madam/Sir,

I'm a doctoral student at Michigan Technological University and would like to request permission to use Figure 15 from your journal in my PhD dissertation work (Implementation of Porous Silicon Technology for a Fluidic Flow-Through Optical Sensor for pH Measurements).

✓ I will require Figure 15 from
Citation

TOPICAL REVIEW A review of micropumps, D J Laser and J G Santiago, J. Micromech. Microeng. 14 R35 doi:10.1088/0960-1317/14/6/R01, Journal of Micromechanics and Microengineering Volume 14 Number 6, 2004


PERMISSION TO REPRODUCE AS REQUESTED IS GIVEN PROVIDED THAT:

- (a) the consent of the author(s) is obtained
- (b) the source of the material including author, title of article, title of journal, volume number, issue number (if relevant), page range (or first page if this is the only information available), date and publisher is acknowledged.
- (c) for material being published electronically, a link back to the original article should be provided (via DOI).

IOP Publishing Ltd
Temple Circus
Temple Way
BRISTOL
BS1 6BE

30/4/2012
Date Rights & Permissions

Fig. 1.2(b)



RightsLink®

[My Orders](#)

[My Library](#)

[My Profile](#)

Welcome kumarv@mtu.edu [Log out](#) | [Help](#)

Home > [My Orders](#) > View Your RightsLink Orders

License Details

This is a License Agreement between Kumar Vanga ("You") and Elsevier ("Elsevier"). The license consists of your order details, the terms and conditions provided by Elsevier, and the [payment terms and conditions](#).

[Get the printable license.](#)

License Number	2872651332412
License date	Mar 19, 2012
Licensed content publisher	Elsevier
Licensed content publication	Journal of Non-Crystalline Solids
Licensed content title	Doped sol-gel glasses as chemical sensors
Licensed content author	Rivka Zusman,Claudio Rottman,Michael Ottolenghi,David Awnir
Licensed content date	June 1990
Licensed content volume number	122
Licensed content issue number	1
Number of pages	3
Type of Use	reuse in a thesis/dissertation
Portion	figures/tables/illustrations
Number of figures/tables/illustrations	2
Format	both print and electronic
Are you the author of this Elsevier article?	No
Will you be translating?	No
Order reference number	None
Title of your thesis/dissertation	Implementation of Porous Silicon Technology for a Fluidic Flow-Through Optical Sensor for pH Measurements
Expected completion date	Apr 2012
Estimated size (number of pages)	180
Elsevier VAT number	GB 494 6272 12
Permissions price	0.00 USD
VAT/Local Sales Tax	0.0 USD / 0.0 GBP
Total	0.00 USD

[← Back](#)

Copyright © 2012 Copyright Clearance Center, Inc. All Rights Reserved. [Privacy statement](#) . Comments? We would like to hear from you. E-mail us at customercare@copyright.com

Fig. 1.3

**ELSEVIER LICENSE
TERMS AND CONDITIONS**

Apr 24, 2012

This is a License Agreement between Kumar Vanga ("You") and Elsevier ("Elsevier") provided by Copyright Clearance Center ("CCC"). The license consists of your order details, the terms and conditions provided by Elsevier, and the payment terms and conditions.

All payments must be made in full to CCC. For payment instructions, please see information listed at the bottom of this form.

Supplier	Elsevier Limited The Boulevard, Langford Lane Kidlington, Oxford, OX5 1GB, UK
Registered Company Number	1982084
Customer name	Kumar Vanga
Customer address	508 Shelden Avenue Houghton, MI 49931
License number	2716060827681
License date	Jul 25, 2011
Licensed content publisher	Elsevier
Licensed content publication	Journal of Chromatography A
Licensed content title	Integrated bio-fluorescence sensor
Licensed content author	Evan Thrush, Ofer Levi, Wonill Ha, Ke Wang, Stephen J. Smith, James S. Harris
Licensed content date	26 September 2003
Licensed content volume number	1013
Licensed content issue number	1-2
Number of pages	8
Start Page	103
End Page	110
Type of Use	reuse in a thesis/dissertation
Portion	figures/tables/illustrations
Number of figures/tables/illustrations	4
Format	both print and electronic
Are you the author of this Elsevier article?	No
Will you be translating?	No

Fig. 1.4

Dear Dr. Smela, I am completing a doctoral dissertation at Michigan Technological University entitled "IMPLEMENTATION OF POROUS SILICON TECHNOLOGY FOR A FLUIDIC FLOW-THROUGH OPTICAL SENSOR FOR pH MEASUREMENTS." I would like to request your permission to reprint in my dissertation excerpts from the following: [Marc Dandin , Pamela Abshire and Elisabeth Smela , "Optical filtering technologies for integrated fluorescence sensors", Lab Chip, 7, 955-977 , 2007] The excerpts to be reproduced are: [Figure 1]. The requested permission extends to any future revisions and editions of my dissertation, including non-exclusive world rights in all languages, and to the prospective publication of my dissertation by UMI. These rights will in no way restrict republication of the material in any other form by you or by others authorized by you. Your signing of this letter will also confirm that you own [or your company owns] the copyright to the above-described material. If these arrangements meet with your approval, please sign this letter where indicated below and return it to me through email. Thank you very much. Sincerely, [Kumar Vanga] Kumar: You have our permission to use the figure with proper attribution in your thesis.

Prof. Elisabeth Smela Department of Mechanical Engineering Room 2176 Glenn
L. Martin Hall (Building 088) University of Maryland College Park, MD 20742 USA

Fig. 1.5(a),(b)

Grant of Permission

Dear Dr. Vanga:

Thank you for your interest in our copyrighted material, and for requesting permission for its use.

Permission is granted for the following subject to the conditions outlined below:

Figure 6: "Current Chemical Biology, 2007, 1, 3-9 3

1872-3136/07 \$50.00+.00 © 2007

Bentham Science Publishers Ltd.

New Emergent Nanotechnologies in Medical and Biochemical Applications:
Advanced Fluorescence Protein-Based Nanosensors Maria Staiano¹, Marcella de Champdoré¹, Stefano Borini², Andrea M. Rossi², Mosè Rossi¹ and Sabato D'Auria*

To be used in the following manner:

1. Bentham Science Publishers grants you the right to reproduce the material indicated above on a one-time, non-exclusive basis, solely for the purpose described. Permission must be requested separately for any future or additional use.
2. For an article, the copyright notice must be printed on the first page of article or book chapter. For figures, photographs, covers, or tables, the notice may appear with the material, in a footnote, or in the reference list.

Thank you for your patience while your request was being processed. If you wish to contact us further, please use the address below.

Sincerely,


Permissions & Rights Manager


Bentham Science Publishers Ltd

Email: permission@benthamscience.org


URL: www.benthamscience.com

Fig. 1.6

 Copyright Clearance Center

 RightsLink®

Home Account Info Help

 ACS Publications
High quality. High impact.

Title: Capillary Optical Sensors
Author: Bernhard H. Weigl et al.
Publication: Analytical Chemistry
Publisher: American Chemical Society
Date: Oct 1, 1994
Copyright © 1994, American Chemical Society

Logged in as:
Kumar Vanga
Account #: 3000432058
LOGOUT

PERMISSION/LICENSE IS GRANTED FOR YOUR ORDER AT NO CHARGE

This type of permission/license, instead of the standard Terms & Conditions, is sent to you because no fee is being charged for your order. Please note the following:


- Permission is granted for your request in both print and electronic formats.
- If figures and/or tables were requested, they may be adapted or used in part.
- Please print this page for your records and send a copy of it to your publisher/graduate school.
- Appropriate credit for the requested material should be given as follows: "Reprinted (adapted) with permission from (COMPLETE REFERENCE CITATION). Copyright (YEAR) American Chemical Society." Insert appropriate information in place of the capitalized words.
- One-time permission is granted only for the use specified in your request. No additional uses are granted (such as derivative works or other editions). For any other uses, please submit a new request.

Fig. 1.7

Dear Kumar, Thank you for contacting The Optical Society. OSA considers your requested use of its copyrighted material to be Fair Use under United States Copyright Law. It is requested that a complete citation of the original material be included in any publication.

Best, Hannah Bembia, Authorized Agent, The Optical Society. Citation X. H. Yang and L. L Wang, "Fluorescence pH probe based on microstructured polymer optical fiber," Opt. Express 15, 16478-16483, 2007

Fig. 1.9 (a)



RightsLink[®]

My OrdersMy LibraryMy Profile

Welcome kumarv@mtu.eduLog out | Help

Home > My Orders > View Your RightsLink Orders

License Details

This is a License Agreement between Kumar Vanga ("You") and Elsevier ("Elsevier"). The license consists of your order details, the terms and conditions provided by Elsevier, and the [payment terms and conditions](#).



[Get the printable license.](#)

License Number	2858290467332
License date	Feb 29, 2012
Licensed content publisher	Elsevier
Licensed content publication	Sensors and Actuators B: Chemical
Licensed content title	Electroosmotic flow pumps with polymer frits
Licensed content author	Shulin Zeng,Chuan-Hua Chen,Juan G Santiago,Jing-Ran Chen,Richard N Zare,Jennifer A Tripp,Frantisek Svec,Jean M.J Fréchet
Licensed content date	28 February 2002
Licensed content volume number	82
Licensed content issue number	2-3
Number of pages	4
Type of Use	reuse in a thesis/dissertation
Portion	figures/tables/illustrations
Number of figures/tables/illustrations	1
Format	both print and electronic
Are you the author of this Elsevier article?	No
Will you be translating?	No
Order reference number	None
Title of your thesis/dissertation	Implementation of Porous Silicon Technology for a Fluidic Flow-Through Optical Sensor for pH Measurements
Expected completion date	Apr 2012
Estimated size (number of pages)	180
Elsevier VAT number	GB 494 6272 12
Permissions price	0.00 USD
VAT/Local Sales Tax	0.0 USD / 0.0 GBP
Total	0.00 USD

Back

Copyright © 2012 Copyright Clearance Center, Inc. All Rights Reserved. [Privacy statement](#) . Comments? We would like to hear from you. E-mail us at customercare@copyright.com

Fig. 1.9 (b)



My OrdersMy LibraryMy Profile

Welcome kumarvl@mtu.eduLog out | Help

Home > My Orders > View Your RightsLink Orders

License Details

This is a License Agreement between Kumar Vanga ("You") and Elsevier ("Elsevier"). The license consists of your order details, the terms and conditions provided by Elsevier, and the [payment terms and conditions](#).

[Get the printable license.](#)

License Number	2857860098875
License date	Feb 28, 2012
Licensed content publisher	Elsevier
Licensed content publication	Journal of Colloid and Interface Science
Licensed content title	Porous glass electroosmotic pumps: design and experiments
Licensed content author	Shuhuai Yao,David E. Hertzog,Shulin Zeng,James C. Mikkelsen,Juan G. Santiago
Licensed content date	1 December 2003
Licensed content volume number	268
Licensed content issue number	1
Number of pages	11
Type of Use	reuse in a thesis/dissertation
Portion	figures/tables/illustrations
Number of figures/tables/illustrations	1
Format	both print and electronic
Are you the author of this Elsevier article?	No
Will you be translating?	No
Order reference number	None
Title of your thesis/dissertation	Implementation of Porous Silicon Technology for a Fluidic Flow-Through Optical Sensor for pH Measurements
Expected completion date	Apr 2012
Estimated size (number of pages)	180
Elsevier VAT number	GB 494 6272 12
Permissions price	0.00 USD
VAT/Local Sales Tax	0.0 USD / 0.0 GBP
Total	0.00 USD

Back

Fig. 1.10



[Home](#) [Account Info](#) [Help](#)



Requesting permission to reuse content from an IEEE publication

Title: Silicon electroosmotic micropumps for integrated circuit thermal management

Conference Proceedings: TRANSDUCERS, Solid-State Sensors, Actuators and Microsystems, 12th International Conference on, 2003

Author: Laser, D.J.; Myers, A.M.; Shuhuai Yao; Bell, K.F.; Goodson, K.E.; Santiago, J.G.; Kenny, T.W.

Publisher: IEEE

Date: 8-12 June 2003

Copyright © 2003, IEEE

Logged in as:
Kumar Vanga
Account #:
3000432058

[LOGOUT](#)

Welcome to RightsLink

IEEE has partnered with Copyright Clearance Center's RightsLink service to offer a variety of options for reusing IEEE content. Select the "I would like to ..." drop-down menu to view the many reuse options available to you.

I would like to...  make a selection 

Note: It is the requester's responsibility to determine whether a copyright and/or credit notice to the third-party owner appears nears the item. Permission to use any third-party material published in an IEEE publication must be obtained from the third-party owner. IEEE disclaims any responsibility for any use you make of content owned by third parties without their permission.

Copyright © 2012 [Copyright Clearance Center, Inc.](#) All Rights Reserved. [Privacy statement.](#)
Comments? We would like to hear from you. E-mail us at customercare@copyright.com

Permission for figures in Chapter 2.

Fig. 2.4

[April 25, 2012]

[Malvern Instruments Ltd
Enigma Business Park
Grovewood Road
Malvern, Worcestershire WR14 1XZ
United Kingdom]

Dear Madam/Sir,

I am completing my doctoral dissertation at Michigan Technological University, USA entitled "IMPLEMENTATION OF POROUS SILICON TECHNOLOGY FOR A FLUIDIC FLOW-THROUGH OPTICAL SENSOR FOR pH MEASUREMENTS." I would like your permission to reprint in my dissertation excerpts from the following:

[http://www.malvern.com/LabEng/technology/zeta_potential/zeta_potential_LDE.htm]

The excerpts to be reproduced are: [Schematic representation of zeta potential].

The requested permission extends to any future revisions and editions of my dissertation, including non-exclusive world rights in all languages, and to the prospective publication of my dissertation by UMI. These rights will in no way restrict republication of the material in any other form by you or by others authorized by you. Your signing of this letter will also confirm that you own [or your company owns] the copyright to the above-described material.

If these arrangements meet with your approval, please sign this letter where indicated below and return it to me through email. Thank you very much.

Sincerely,


[Kumar Vanga]

PERMISSION GRANTED FOR THE
USE REQUESTED ABOVE:

[Malvern Instruments Ltd]

Date: 26/4/12

Fig. 2.7, Fig. 2.8, Fig. 2.11, and Fig. 2.15



RightsLink[®]

[My Orders](#)

[My Library](#)

[My Profile](#)

Welcome kumarv@mtu.edu [Log out](#) | [Help](#)

Home > [My Orders](#) > View Your RightsLink Orders

License Details

This is a License Agreement between Kumar Vanga ("You") and John Wiley and Sons ("John Wiley and Sons"). The license consists of your order details, the [terms and conditions](#) provided by John Wiley and Sons, and the [payment terms and conditions](#).

[Get the printable license.](#)

License Number	2895171138988
License date	Apr 24, 2012
Licensed content publisher	John Wiley and Sons
Licensed content publication	physica status solidi (a) applications and materials science
Licensed content title	Macro porous silicon as pump media for electro-osmotic pumps
Licensed content author	J. Z. Wallner,N. Nagar,C. R. Friedrich,P. L. Bergstrom
Licensed content date	Apr 16, 2007
Start page	1327
End page	1331
Type of use	Dissertation/Thesis
Requestor type	University/Academic
Format	Print and electronic
Portion	Figure/table
Number of figures/tables	2
Original Wiley figure/table number(s)	Figure 2(b), Figure 4(a), Figure 4(b)
Will you be translating?	No
Order reference number	None
Total	0.00 USD

Back

Copyright © 2012 Copyright Clearance Center, Inc. All Rights Reserved. [Privacy statement](#) . Comments? We would like to hear from you. E-mail us at customercare@copyright.com

Table 2.4

Kumar, Yes, you have my permission to use Table 2: Dynamic micropumps and request your permission. Citation- TOPICAL REVIEW, A review of micropumps, D J Laser and J G Santiago 2004, J. Micromech. Microeng. 14 R35, Journal of Micromechanics and Microengineering Volume 14 Number 6. Regards, Juan G. Santiago, Professor of Mechanical Engineering Stanford University, Stanford, CA 94305-3030



To: permissions@iop.org,
Cc:
Bcc:
Subject: Permission to use some figures in my PhD Dissertation Work
From: "Kumar L. Vanga" <kumarvl@mtu.edu> - Monday 26/03/2012 20:40

Dear Madam/Sir,

I am a doctoral student at Michigan Technological University and would like to request permission to use part of a Table from your journal in my PhD dissertation work (Implementation of Porous Silicon Technology for a Fluidic Flow-Through Optical Sensor for pH Measurements).

I will require part of Table 2: Dynamic micropumps and request your permission.

✓ Citation

TOPICAL REVIEW A review of micropumps, D J Laser and J G Santiago 2004 J. Micromech. Microeng. 14 R35 doi:10.1088/0960-1317/14/6/R01
Journal of Micromechanics and Microengineering Volume 14 Number 6

Thank you for your help and I hope to hear from you soon. My contact details are listed below. Please let me know if you require any other details from me.

Sincerely,
Kumar Vanga

Contact Phone: 6107905549

Doctoral Candidate
WIMS MTU Student Leadership Council Chairperson
ECE GSG Representative
Department of Electrical and Computer Engineering
Michigan Technological University



PERMISSION TO REPRODUCE AS REQUESTED IS GIVEN PROVIDED THAT:

- (a) the consent of the author(s) is obtained
- (b) the source of the material including author, title of article, title of journal, volume number, issue number (if relevant), page range (or first page if this is the only information available), date and publisher is acknowledged.
- (c) for material being published electronically, a link back to the original article should be provided (via DOI).

IOP Publishing Ltd
Temple Circus
Temple Way
BRISTOL
BS1 6BE

27/03/2012
Date

Permission for the content in Chapter 3



My OrdersMy LibraryMy Profile

Welcome kumarv@mtu.eduLog out | Help

Home > My Orders > View Your RightsLink Orders

License Details

This is a License Agreement between Kumar Vanga ("You") and John Wiley and Sons ("John Wiley and Sons"). The license consists of your order details, the [terms and conditions](#) provided by John Wiley and Sons, and the [payment terms and conditions](#).

[Get the printable license.](#)

License Number	2895180192339
License date	Apr 24, 2012
Licensed content publisher	John Wiley and Sons
Licensed content publication	physica status solidi (c) Current topics in solid state physics
Licensed content title	Optical properties of thick ordered mesoporous silica membranes
Licensed content author	Kumar Vanga,Dawdon Cheam,Christopher Middlebrook,Paul Bergstrom
Licensed content date	Mar 2, 2011
Start page	1941
End page	1945
Type of use	Dissertation/Thesis
Requestor type	Author of this Wiley article
Format	Print and electronic
Portion	Full article
Will you be translating?	No
Order reference number	None
Total	0.00 USD

← Back

Permission for the content in Chapter 4



[Home](#) [Create Account](#) [Help](#)



Requesting permission to reuse content from an IEEE publication

Title: Implementation of porous silicon technology for flow-through sensing using electro-osmotic phenomenon

Conference Proceedings: Nanotechnology (IEEE-NANO), 2011 11th IEEE Conference on

Author: Vanga, K.L.; Qili Hu; Green, S.A.; Bergstrom, P.L.

Publisher: IEEE

Date: 15-18 Aug. 2011

Copyright © 2011, IEEE

User ID

Password

☐ Enable Auto Login

LOGIN

[Forgot Password/User ID?](#)

If you're a [copyright.com](#) user, you can login to RightsLink using your [copyright.com](#) credentials. Already a [RightsLink](#) user or want to [learn more?](#)

Thesis / Dissertation Reuse

The IEEE does not require individuals working on a thesis to obtain a formal reuse license, however, you may print out this statement to be used as a permission grant:

Requirements to be followed when using any portion (e.g., figure, graph, table, or textual material) of an IEEE copyrighted paper in a thesis:


- 1) In the case of textual material (e.g., using short quotes or referring to the work within these papers) users must give full credit to the original source (author, paper, publication) followed by the IEEE copyright line © 2011 IEEE.
- 2) In the case of illustrations or tabular material, we require that the copyright line © [Year of original publication] IEEE appear prominently with each reprinted figure and/or table.
- 3) If a substantial portion of the original paper is to be used, and if you are not the senior author, also obtain the senior author's approval.

Requirements to be followed when using an entire IEEE copyrighted paper in a thesis:

- 1) The following IEEE copyright/ credit notice should be placed prominently in the references: © [year of original publication] IEEE. Reprinted, with permission, from [author names, paper title, IEEE publication title, and month/year of publication]
- 2) Only the accepted version of an IEEE copyrighted paper can be used when posting the paper or your thesis on-line.
- 3) In placing the thesis on the author's university website, please display the following message in a prominent place on the website: In reference to IEEE copyrighted material which is used with permission in this thesis, the IEEE does not endorse any of [university/educational entity's name goes here]'s products or services. Internal or personal use of this material is permitted. If interested in reprinting/republishing IEEE copyrighted material for advertising or promotional purposes or for creating new collective works for resale or redistribution, please go to http://www.ieee.org/publications_standards/publications/rights/rights_link.html to learn how to obtain a License from RightsLink.

If applicable, University Microfilms and/or ProQuest Library, or the Archives of Canada may supply single copies of the dissertation.

Fig. 4.1



RightsLink[®]

[My Orders](#)[My Library](#)[My Profile](#)

Welcome kumarv@mtu.edu [Log out](#) | [Help](#)

Home > [My Orders](#) > View Your RightsLink Orders

License Details

This is a License Agreement between Kumar Vanga ("You") and Elsevier ("Elsevier"). The license consists of your order details, the terms and conditions provided by Elsevier, and the [payment terms and conditions](#).

[Get the printable license.](#)

License Number	2895200002829
License date	Apr 24, 2012
Licensed content publisher	Elsevier
Licensed content publication	Analytica Chimica Acta
Licensed content title	Spectrophotometric pH measurements of freshwater
Licensed content author	Craig R French,Jeffrey J Carr,Eleanor M Dougherty,Lisa AK Eidson,Jason C Reynolds,Michael D DeGrandpre
Licensed content date	18 February 2002
Licensed content volume number	453
Licensed content issue number	1
Number of pages	8
Type of Use	reuse in a thesis/dissertation
Portion	figures/tables/illustrations
Number of figures/tables/illustrations	1
Format	both print and electronic
Are you the author of this Elsevier article?	No
Will you be translating?	No
Order reference number	None
Title of your thesis/dissertation	Implementation of Porous Silicon Technology for a Fluidic Flow-Through Optical Sensor for pH Measurements
Expected completion date	Apr 2012
Estimated size (number of pages)	180
Elsevier VAT number	GB 494 6272 12
Permissions price	0.00 USD
VAT/Local Sales Tax	0.0 USD / 0.0 GBP
Total	0.00 USD

[← Back](#)

Copyright © 2012 Copyright Clearance Center, Inc. All Rights Reserved. [Privacy statement](#) . Comments? We would like to hear from you. E-mail us at customercare@copyright.com

Permission for the figures in Chapter 5

Figure 5.1

Kumar, Sure you can use the image. Prof. Conley, Professor, Electrical Engineering and Computer Science & Materials Science Oregon State University 3089 Kelley Engineering Center Corvallis, OR 97331-5501 (541)737-9874

Permission for figures in Appendix A

Fig. A.1 (a), Fig. A.1 (b), and Fig. A.2

4/26/2012

Dr. Jin Wallner

33 Timothy Heights, Pleasant Valley NY, 12569

Dear Dr. Jin Wallner,

I am completing a doctoral dissertation at Michigan Technological University entitled "IMPLEMENTATION OF POROUS SILICON TECHNOLOGY FOR A FLUIDIC FLOW-THROUGH OPTICAL SENSOR FOR pH MEASUREMENTS." I would like your permission to reprint in my dissertation excerpts from the following:

[J. Zheng, "Porous silicon technology for integrated microsystems", PhD dissertation, Electrical & Computer Engineering Department, MTU, Houghton, MI, 2006.]

The excerpts to be reproduced are: [Figure 3.5, Figure 3.6, Figure 3.29, and Figure 5.11].

The requested permission extends to any future revisions and editions of my dissertation, including non-exclusive world rights in all languages, and to the prospective publication of my dissertation by UMI. These rights will in no way restrict republication of the material in any other form by you or by others authorized by you. Your signing of this letter will also confirm that you own [or your company owns] the copyright to the above-described material.

If these arrangements meet with your approval, please sign this letter where indicated below and return it to me through email. Thank you very much.

Sincerely,

[Kumar Vanga]

PERMISSION GRANTED FOR THE
USE REQUESTED ABOVE:

Sign Here:

[Dr. Jin Wallner]

Date: 4/26/2012